p- and e- type Semiconductor layers optimization for efficient perovskite photovoltaics

By

Kevin Tambwe

(BSc. Chemical Science (UWC), BSc. Honours Chemical Science (UWC))

In fulfillment of the requirement for the degree of

Magister Scientiae in Chemical science

Faculty of Sciences, University of the Western Cape

Bellville, Cape Town, South Africa

Supervisors: Dr Natasha Ross and Prof. Priscilla Baker

November, 2019

Declaration

I, hereby declare that "*p- and e- type semiconductor layers optimization for efficient perovskite photovoltaics*" is the result of my own work that was done by me under the supervision of Dr. Natasha Ross and co-supervision of Prof. Priscilla Baker, and that it has not been previously submitted for any degree or examination in any other university or higher education; and that all the sources and quotations have been indicated and acknowledged by complete references.

Kevin Tambwe November 2019

Signed …… Date ……

Abstract

Perovskite solar cells have attracted a tremendous amount of research interest in the scientific community recently, owing to their remarkable performance reaching up to 22% power conversion efficiency (PCE) in merely 6 to 7 years of development. Numerous advantages such as reduced price of raw materials, ease of fabrication and so on, have contributed to their increased popularity. However, there are several factors that limits their performance, among which is recombination process of charge carriers occurring at the TiO_2/Perovskite interface. Therefore, it is crucial to prevent charge carriers recombination at the photo anode/electrode interface, in order to improve the overall efficiency of the Perovskite solar cell (PSC) devices.

In the initial part of this work an attempt to reduce the recombination process occurring at the electron transport layer (ETL) which in this work is compact-TiO_2 and the Perovskite interface was initiated, through the elimination of defects such as pinholes which are for the most part responsible for charge recombination at that interface. This was achieved by the optimization of the spin-coating conditions and parameters of the ETL. Secondly, an investigation into the photo-absorptivity of Silver-modified anode (Ag-TiO_2 compact composite films) was carried out. Finally a detailed manuscript describing how to fabricate high performance PSC layer by layer and how to measure the performance of the cells by I-V measurements was put together.

The first part of the fabrication process involved the preparation of the interface materials which in this case consisted of Ag–TiO_2 and TiO_2 films , then the characterization via High-Resolution Transmission Electron Microscopy (HR-TEM), via High-Resolution Scanning Electron Microscopy (HR-SEM), X-ray Diffraction (XRD), Fourier Transform Infra-Red Spectroscopy (FTIR), UV-visible spectroscopy, Cyclic Voltammetry (CV), to determine the

internal structure, morphology, microstructures, chemical compositions, optical properties and conductivity, of the samples respectively.

From HR-SEM, it was found that the silver nanoparticles were uniformly spread and strongly attached to the mesoporous TiO_2 matrix. The morphology of the composite film could be controlled by simply adjusting the molar ratio of the silver nitrate aqueous solution.

Cyclic voltammetry (CV) was used to test for pinhole defects in the ETL/blocking layer; it revealed that the TiO_2 compact layer had a good blocking capability which was observed by a substantial decrease in the anodic and cathodic peak currents with respect to the bare ITO electrode. This decrease also indicated that there was good surface coverage and the presence of no pinholes which was also confirmed by the HR-SEM images. Furthermore, the addition of the silver nanoparticles to the TiO_2 compact layer improved the electron mobility which was observed by higher current collection suggested by the increase in peak currents with respect to the non-modified TiO_2 compact layer. From these results, we were able to assume that the electron transport layer could effectively not only reduce the recombination process occurring at the interface in the middle of the electron transport layer and the absorbing material, but also allow for an easy transport of charges to and from the ETL.

UV-Vis results revealed an improvement in terms of the luminescent properties of TiO_2 compact layer with the addition of the Ag NPs. The functionalization with Ag NPs induced a red shift in absorption caused by a reduction in the band gap of the TiO_2. This reduction in band gap allowed for the absorption of more light, therefore also causing the perovskite layer to absorb more light and therefore generate more charge carriers which can in turn allow for more current to be generated.

Finally, from IV-measurements, the best PSC developed which had 1.5 % $AgTiO_2$ composite compact film had the best PCE with a value of 0.14%. This low PCE was attributed to the

very low current generation of the cells as a result of the high thickness of the absorbing layer.

Acknowledgment

I would like to acknowledge my indebtedness and render my warmest thanks to my supervisor, Dr. Natasha Ross, who made this work possible through her tremendous support. Her friendly guidance and expert advice have been invaluable throughout all stages of the work. I would also wish to express my gratitude to Professor Priscilla Baker for the financial support and extended discussions with valuable suggestions which have contributed greatly to the improvement of the thesis. The thesis has also benefited from comments and suggestions made by Olivier Tambwe and Kelechi Nwambaekwe who have read through the manuscript. I take this opportunity to thank them. Special thanks are due to my friends from the chemistry department, Sazi Thwala, Nelia Sanga and Zayaan Sampson for their continuous support and understanding, but also for more concrete things like commenting on earlier versions of the thesis, helping with the figures and the final preparation of the manuscript. My thanks are extended to my father and mother, Roger Tambwe, for supporting me both financially and emotionally during these two years . The person with the greatest indirect contribution to this work is my mother, Marie Tambwe, who has taught me love of mathematics and science ingerneral. I want to thank her, my siblings, as well as my brother Olivier Tambwe, my sister Peggy Tambwe for their constant encouragement. I finally would like to thank everyone with whom I have worked in the Sensor Lab research group for their kindness and support during the completion of my degree.

Cape Town, November 30th, 2019

Kevin Tambwe

Table of contents

Contents

List of figures

Abbreviations

Ag NPs	Ag nanoparticles
Al_2O_3	Aluminum(III) oxide
AM1.5G	Air-mass 1.5 global analysis
CB	Conduction band
CH_4	Methane gas
CO_2	Carbon dioxide
COP	Conference of parties
c-TiO_2	Compact TiO_2
CV	Cyclic voltammetry
DMF	N,N-dimethylformamide
DMSO	dimethylsulfoxide
EDS	Energy dispersive spectroscopy
EQE	External quantum efficiency
ETM	Electron transporting material
FF	Fill-Factor
H_2O	Water
HCl	Hydrochloric acid

HR-SEM	High resolution scanning electron microscopy
HR-TEM	High Resolution Transmission Electron Microscopy
HTM	Hole transporting material
ITO	Indium tin oxide
J_{max}	Maximum current density
J_{sc}	Short-circuit current density
I-V	Current density-voltage curves
Li-TFSI	lithium-bis(trifluoromethanesulfonyl)imide
m-TiO_2	Mesoporous TiO_2
N_2O	Nitrous oxide
NP	Nanoparticle
NREL	National renewable energy laboratory
PbI_2	Lead (II) iodide
PCE	Power Conversion Efficiency
P_{in}	Incident power
P_{max}	Maximum power output
PSCs	Perovskite solar cells
PWh	Peta Watt-hour

SAXS	Small-Angle X-ray Scattering
Spiro-OMeTAD	2,2′,7,7′-tetrakis-(N,N-di-p-methoxyphenylamine)-9,9′-bifluorene
TCO	Transparent conductive oxide
TiO_2	Titanium dioxide
UV-vis	Ultraviolet-visible Spectroscopy
VB	Valence band
V_{max}	Maximum voltage
V_{mp}	Maximum-power voltage
V_{oc}	Open-circuit voltage
V_{oc}	Open-circuit voltage
XRD	X-ray Diffraction
η	Power conversion efficiency.

Chapter 1 Introduction

This chapter explains the reasons surrounding the research and investment into renewable energy and photovoltaic technologies. Particularly, contextual information about perovskite solar cells is given; the device structural design and operating principle of the cells are also discussed. Finally, the aim which was to improve the power conversion efficiency (PCE) of the devices through the addition of metallic nanoparticles, as well as the research framework of this project is laid out.

1.1 Introduction

1.1.1 Global energy crisis

With the constant growth in the worldwide population and economy, there has been a significant increase in the demand for energy. The increase in energy demand has been accompanied by a projected increase in energy consumption of ~28% going from 169 PWh in 2015 to 216 PWh in 2040 [1]. Countries with strong developing economies like China and India are the biggest contributors to this increase [1]. Although renewable energy is currently fastest-growing energy source in the world, most of the energy is still expected to be produced by the burning of fossil fuels.

One of the most significant challenges humanity is currently confronted with is global warming, which is happening as a result of the burning of fossil fuels. The immediate consequences that emanate from the burning of fossil fuels could potentially be disastrous for the earth. As exhibited by the historic success of the COP21 summit in Paris in 2015, there is a worldwide motivation to tackle the issue and the international community is promising to join in efforts against climate change.

The phenomenon called global warming was brought about by the accumulation of ozone-depleting substances otherwise known as greenhouse gases (mainly CO_2, CH_4, and N_2O) in the atmosphere, which traps the sun's heat reflected by the earth's surface [2,3]. Although these gases occur naturally in the atmosphere, human activities have contributed huge quantities, since the industrial revolution, therefore disturbing the natural equilibrium. CO_2 is the greenhouse gas, which is responsible for a large portion of the global warming issues we are currently confronted with [4]. It is for the most part emitted as a waste product of burning fossil fuels. In developing countries such as South Africa, for instance, most of the energy consumed today still comes from

fossil fuels. Fossil fuels energy consumption in South Africa was estimated to be 86.79 % as of 2014, and its highest value throughout the past 43 years was 90.51 % in 1982, whereas its lowest value was 84.24% in 2000 [5]. This very high reliance on fossil fuels and non-renewable energy sources, in general, is on its own a problem that will have to be tended to.

Humans as well are to blame for this situation, typically because of deforestation and the consumption of fossil fuels. By doing so, they are disrupting the natural process of CO_2 capture. Strong correlation exists between global temperatures and atmospheric CO_2 levels as shown in **Figure 1.1**.

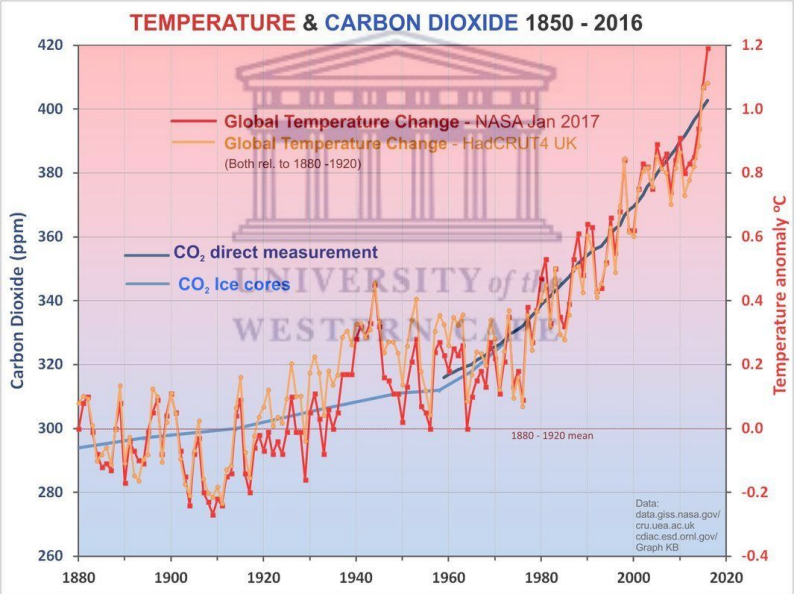

Figure 1.1: Historic correlations between global temperatures and atmospheric CO_2 levels [6].

As the earth's temperature rises, feedback loops accelerate the process (e.g. as polar ice melts the earth's surface becomes on average less reflective of the sun's light thus absorbing more heat). The two other major greenhouse gases, (CH_4 and N_2O), while produced by humans in a lot lower quantities, are unquestionably far more effective in trapping heat than CO_2. The former is a by-

product of livestock farming, while the latter is emitted by various agricultural and industrial activities including the proliferation of nitrogen-based fertilizers and the burning of fossil fuels.

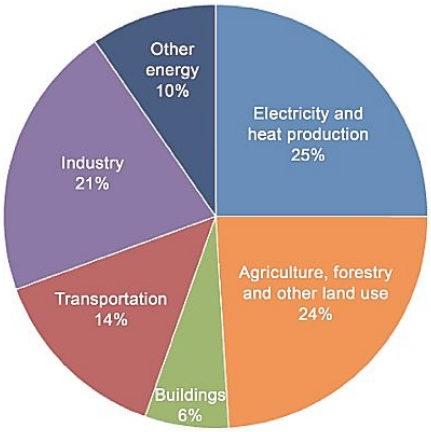

Figure 1.2: Global greenhouse gas emission by economic sectors [7].

The strategies to fight global warming are generally based on eliminating its root cause – greenhouse gases. Three fundamental spheres of human activities are responsible for the vast majority of the emissions or discharge of harmful gases in the atmosphere as shown in **Figure 1.2.** These are electricity and heat production, industrial production and agriculture. Of these three, electricity and heat generation is marginally responsible for the biggest part of the emissions. Despite the continuous effort to make these processes more environmentally friendly, more than 80 % of the energy globally is still supplied by the burning of fossil fuels like coal, oil and natural gases for instance [6]. Hence, the strategies to deal with global warming, very often are centered on substituting fossil fuel-generated energy with one derived from carbon-free sources such as nuclear, hydro, wind, geothermal, biomass and solar.

1.1.2 Renewable energy potential

While the world, in general, is severely being affected by the growing issues of global warming and environmental pollution, developing clean and renewable energies able to supplant

conventional fossil fuels has become an indispensable choice, making renewable energy sources such as water, wind and solar power the best substitute to resolve the ever-increasing demand for energy [7,8]. Setting environmental issues aside, it is imperative to understand that fossil fuels are limited commodities and they will not be able to power the growing energy appetite of the world economy for much longer. The world reserves of oil and gas are expected to be depleted within several decades, while those of coal will most likely not last beyond the turn of the century if the growing energy demand is not met with alternative energy sources. Pollution-free renewable resources are gaining importance at an accelerated pace [9]. They will not necessarily help reduce the devastating impacts that fossil fuels have had on the environment thus far, but they will help diversify the means of energy generation.

In principle, the amount of renewable energy available for harvesting is in many orders of magnitude larger than the energy currently consumed by humanity. An old cliché is that the amount of sunlight reaching the earth in just one hour is enough to power the world economy for a full year. However, the technical potential is only a fraction of that. Practically speaking, for renewable energy to be fully embraced, it has to be cost-competitive against the energy derived from conventional sources.

One big issue that emerges from the utilization of renewable energy is the fact that they require very specific locations for the production of the required energy, which is not the case with non-renewable energy sources such as gas, coal, and oil. Each of the renewable energy sources has its limitations; for instance, the availability of hydroelectricity is limited geographically and it is often concentrated in remote areas, from where it is costly to transport it to consumers. Additionally, it has a major environmental footprint as large areas of land have to be flooded, and it is highly dependent on precipitations. Then again, the amount of geothermal, wave and

biomass energy theoretically available for harvesting is too little to realistically contribute a significant share into a global energy mix [10,11]. This leaves wind and solar energy as the main contenders to substitute the fossil-fuel energy production and to satisfy the rising energy demand. They have their disadvantages though; the relatively high price aside, they are sporadic by nature as wind and sunlight are not available on demand. Hence, a power grid, which integrates a substantial amount of wind and solar power, will inevitably have to contain storage capacity, large overcapacity backed up with conventional power plants or a very efficient way of energy redistribution between remote areas. Regardless of this, wind and solar power will very likely be able to supply the vast majority of the energy in the future if they are used jointly.

In this thesis, the emphasis will be on one particular type of energy conversion system: Solar Photovoltaics (PVs) that convert sunlight directly into electricity.

1.1.3 The case for solar power

The solar power industry is gaining worldwide interest [7]. Being one of the renewable sources of energy, solar energy is becoming a primary source of energy considering that fossil fuel resources are limited and harmful to the environment [12]. The sun is the fundamental driving force behind most natural processes on earth. It is, therefore, an obvious source from which to try to artificially extract heat or light energy and convert it to a useable form.

There are various ways in which solar energy can be harvested that have proven to be extremely efficient. A more direct approach is to convert the light energy incident on materials to electricity using photovoltaics. In principle, this requires lower arable land usage, less infrastructure and a reduced visual impact than many of the other renewable technologies. It is also suited to developing regions of the world, such as Africa, where the growing of energy crops or the utilization of hydroelectricity or wind power is not as feasible. In theory, it is possible to produce

electricity at the point of use, with solar panels mounted on buildings, thus minimizing losses associated with the long dsitance distribution of power.

There are still several issues that must be addressed when it comes to solar and other renewable energy technologies. These include the incorporation of several technologies to eliminate potential shortfalls such as in higher latitudes where solar insolation is lower. Energy storage is also another challenge that must be overcome to help deal with the inherent intermittency of solar power; i.e. generation only during the daytime, but power needed at night.

What is clear is that solar power has the potential to provide much of the world's energy demand [13,14], as shown in **Figure 1.3**. Relatively small areas of land would have to be covered in solar panels to generate sufficient electricity to meet the global demand, particularly if this was done in deserted regions. In practice, it would be more sensible to produce this power nearer to where it is utilized, but it nonetheless emphasizes the potential of solar power.

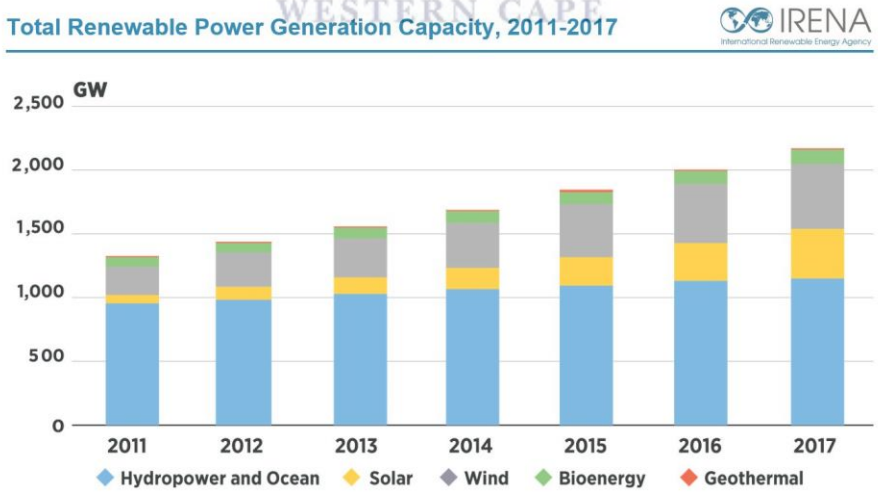

Figure 1.3: Total renewable power generation capacity, 2011-1017 [16]

1.1.4 Solar cells

The sun is one of the most prominent resources on the earth, as it provides the necessary energy for life to subsist and grow. Solar cells or photovoltaic cells (PV cells), were developed to capture the energy radiated by the sun and convert it into usable energy. Photovoltaic cells (PV) are one of the key solar energy technologies, where photoelectric devices of which electrical properties like current, voltage or resistance, are changed once exposed to the radiation of the sun, to directly convert the harvested solar light into electricity [9]. These devices need to accomplish mainly two tasks: photo-generation of charge carriers (electrons and holes) in a light-absorbing material, and separation of the charge carriers to a conductive contact that will transmit the electricity. This conversion is called the photovoltaic effect, these solar devices are regarded as one of the main technologies towards a sustainable energy generation [7].

While solar collectors can have multiple applications, the most common use is for electricity generation as previously mentioned. By absorbing the sun's radiation, a solar cell can generate a current, which is typically sent into the electricity grid. The primary function of a solar cell is to absorb energy through sunlight. A semiconductor is used as the absorber layer. The nature of the material allows the free flow of electrons as energy is introduced. There are specific materials that are selected for these layers based on their band gaps, the energy difference between an excited electron and an electron at its low energy state. The band gaps need to be selected properly to ensure an electron will reach a specific energy level when exposed to the sunlight. Once electrons are excited and reach a higher energy state, additional conductor layers are needed to carry the electrons out of the cell. One layer allows the electrons to move away from the original layer, while the other allows the leftover positive charge, or a 'hole' for better visualization, to also move away. The combination of moving electrons and the holes generates

the output current that allows for usable electrical power. Since these layers are conductors, the electrical conductivity is crucial to provide sufficient current. One must be careful to factor the change in conductivity as both temperature and shape (and thus cross-sectional area) change, which both vary with different applications of a solar cell.

1.1.5 Types of solar cells

The prototype solar cells were first developed in the 1950s. Since then, three distinct generations of solar cells have emerged, each with a different type of architecture and purpose. The future of solar energy technologies needs to develop systems with the highest efficiencies while minimizing their cost of production and installation. Each generation fulfills a specific need for commercial use and production. Through research and application, there is an opportunity to maximize the efficiency of each generation or combine their benefits.

The first-generation of solar cells includes cells made of silicon wafers. These cells require a substantial amount of material to manufacture and significant effort to transport and install. The manufacturing process involves creating molten silicon at temperatures above 1400°C to form the necessary crystal structure. Although they are costly to manufacture and install, and despite being the first to be developed, these cells are still the most common type of solar cell used today. A single-junction solar cell with an indirect bandgap has a theoretical maximum efficiency of approximately 35 % [14]. However, typical efficiencies of first-generation cells fall within the range of 15-25% [15].

Second-generation solar cells are categorized as thin-film cells. To achieve thin films, more amorphous and organic materials are utilized. Though not as efficient as the original crystalline silicon, the organic material layers still allow for reasonable efficiencies ranging from 15-20 % [16]. With a thin-film cell, far less material is required to fabricate the layers and the cell can be

annealed at room temperature. With shorter processing time and lower material costs, these second-generation cells have the potential to drastically reduce the total cost of solar cell production while only being slightly less efficient than the top of the line first-generation cells.

The most recent generation of cells is called heterojunction cells. This third-generation, although it is the youngest class of solar cells, has already had example prototypes that have achieved efficiencies higher than the theoretical maximum of the previous single-junction cells. As more layers (and junctions) are added with different bandgaps, it is possible to capture more of the excited electrons. The maximum theoretical efficiency of a cell with an infinite number of junctions can reach values over 45 % [17].

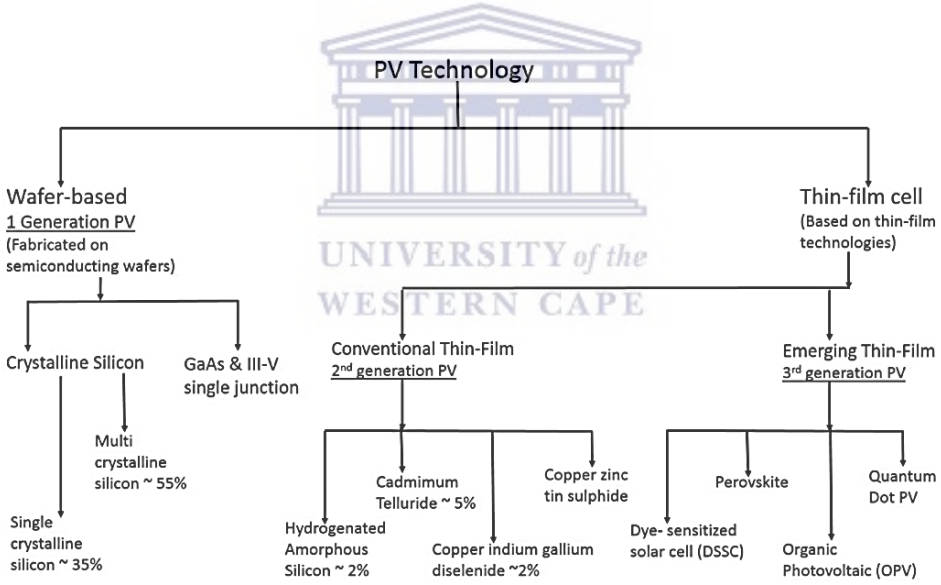

Figure 1.4: Classification of photovoltaic technologies with their current market share in percentage [10].

Figure 1.4 shows the various types of photovoltaic technologies developed to date, with crystalline silicon solar cells being at the very top in terms of market shares estimated at around 90 %. Very few of these PV technologies are commercialized and most linger at the research level. The solar PV market as previously mentioned is presently dominated by crystalline silicon

(c-Si) technology due to its increased power conversion efficiency (PCE) that went from about 15 % to 25 % over the last 40 years [18]. Silicon solar cells' popularity on the market is also due to their extended lifespan of nearly 20 years and the low manufacturing price of cells caused by mass production by large business corporations. However, the technical hitches with silicon solar cells come during the manufacturing process which necessitates a lot of heat energy in manufacturing the crystalline silicon structures, the manufacturing process in turn also generates large amounts of Co and CO_2 [19]. Besides, Silicon solar cells generally make use of rare and poisonous constituents like cadmium telluride, copper indium selenide, cadmium indium gallium di-selenide and silicon tetrachloride [20,21]. As a result, studies are currently being done to find other structured solar cells that typically derived from organic and abundant materials such as dye-sensitized-, organic-, and perovskite solar cells (PSCs).

Amongst the most promising alternatives to silicon solar cells, PSCs have shown the highest power conversion efficiency (PCE) growth going from 9.7 % [22] to 22 % [23] over 5 to 7 years. The rise of perovskite solar cells (PSCs) is evidences of a transformation in the field of photovoltaics, assuring the combination of low cost and high efficiency. At the same time, as an emerging photovoltaic technology with fast-developing speed, perovskite solar cells (PSCs) have drawn broad attention [24]. But then again these cell loose efficiency during operation [20] due to the unstable nature of its material constituents, so until that issue is dealt with it will not be able to measure up with the conventional silicon solar cells. Nevertheless, it is still an attractive area of research due to numerous factors: it does not necessitate a lot of heat energy to manufacture, the ability to fabricate highly efficient devices via solution processing and it can be applied on flexible surfaces like plastic [25]. PSCs consist of abundant materials and it is a young area of research that presents unknowns to be discovered. Furthermore, the high power-

conversion efficiency (PCE) levels (22 to 23 %) are the effect of exceptional material properties, including strong and broad absorption, long carrier lifetimes and diffusion lengths, defect tolerance and photon recycling [26–29]. An additional benefit is the versatility of the optoelectronic properties, specifically, the bandgap, which can be reached by substitution and alloying. This unfolds a huge chemical space from which a large number of material combinations are conceivable. With attested PCE values of over 22%, this new type of solar cells is set to contend with leading photovoltaic technologies, either as an improving tandem layer or as a separate substitute [30–32].

The weak stability in air and moisture, particularly when compared with conventional solar materials, is a major problem that is slowing the commercialization of perovskite solar devices [33–36]. Therefore, much effort should continue to be invested in attaining higher PCE values; at the same time, there should be efforts to improve the stability of the perovskite layer as well.

1.1.6 Perovskite Solar Cells (PSCs)

The earliest article on perovskite solar cells came out in 2009. In that article, the power conversion efficiency reported was 3.8% with very negligible stability [37]. In 2012 Kim et al. [38] were able to fabricate a perovskite solar cell device with an efficiency of 9.7% and overall stability of 500 h.

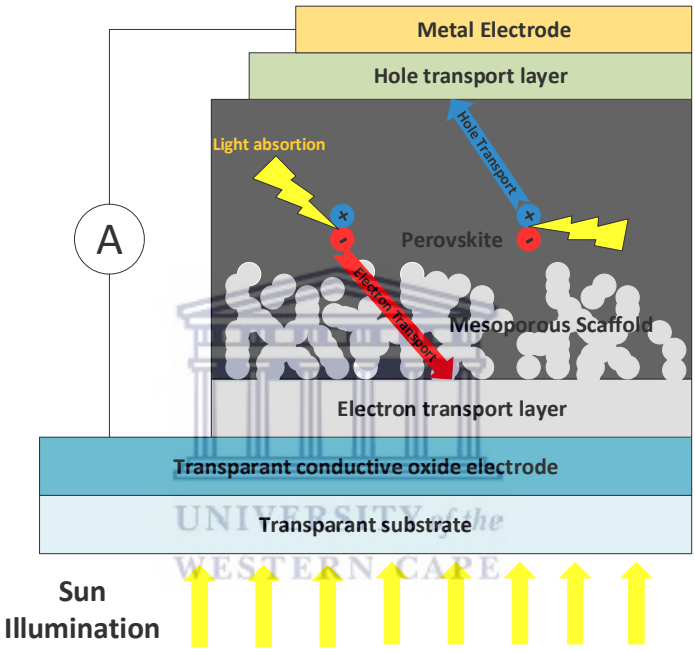

Figure 1.5: General schematic structures for a perovskite solar cell, with the sun as the illumination source.

Figure 1.5 gives a general structural design of PSCs. In its structure the PSC device consist of a transparent electrode, like indium tin oxide (ITO) or fluorine-doped tin oxide (FTO), coated on a glass surface and on top of the ITO/FTO there is an electron transporting layer (ETL) which in most cases may consist of a compact and a mesoporous layer (optional) of a metal oxide. Lying on top of the ETL is the perovskite layer that acts as the active layer (absorbing layer) where the light in the form of photons is absorbed and electron-hole pairs (exciton) are excited. Above the

perovskite layer is the hole transporting layer (HTL) and lastly on it is a metallic electrode. To make a closed-circuit system, the transparent electrode and the metallic electrode are connected as depicted in **Figure 1.5.**

A lot of research and development (R&D) has been done over the years, on the different layers in the perovskite device structure, as all these layers contribute to some extent to the overall PCE by a few percent. The electron transport layer which constitutes a very important part of the device has been given a lot of attention [37–39] for its capability to augment the cell performance considerably by gathering electrons more effectively which prevents electron-hole recombination. Experimentations have been made using a compact TiO_2 layer before adding the mesoporous TiO_2 layer to block the holes. The result indicated lower series resistance and higher shunt resistance than without the compact TiO_2 layer. That means it prevents the recombination of electrons-holes and it reduces resistance in the ETL which results in increased PCE because the electrons are gathered without much resistance. The ETL layer is either formed by spin-coating, spray pyrolysis or evaporation [38,40].

1.2 Thesis Synopsis

1.2.1 Aims and objectives

Thin-film solar cells based on hybrid organic-halide lead perovskites reached power conversion efficiency exceeding 22%. However, one key problem for development of this technology even further is to surmount the performance losses at both electron and hole transporting interface layers without compromising low costs and stability. The proper choice of the architecture and the interface materials, as well as their influence on the device performance and device reproducibility, becomes of utmost importance.

This project aimed to develop efficient and cost-effective solar cells through the process of synthesis, fabrication and optical and electrochemical characterization of Ag-TiO_2/Perovskite/ Spiro-OMeTAD-based PSCs which is depicted in **Figure 1.6**. The addition of Ag to the TiO_2 electron transport layer (ETL) is expected to strengthen the optical absorption of the perovskite solar cells in the visible light region. Additionally, the presence of Ag is expected to enhance the efficiency of electron injection and photo-stability in the perovskite solar cell which in turn will lead to the improvement of the overall performance of the device.

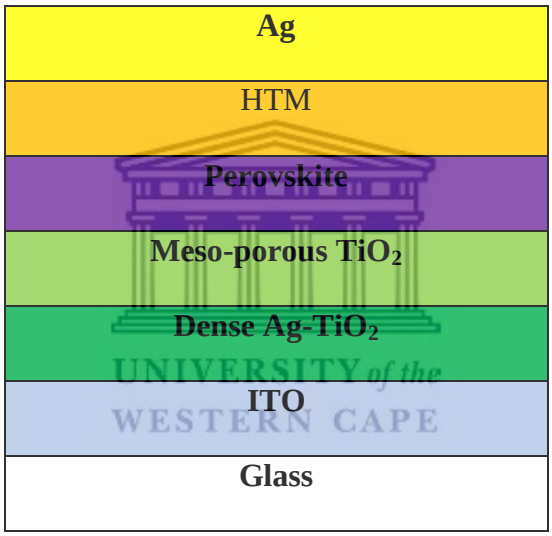

Figure 1.6: Layout of the solar cells structure.

1.2.2 Research framework

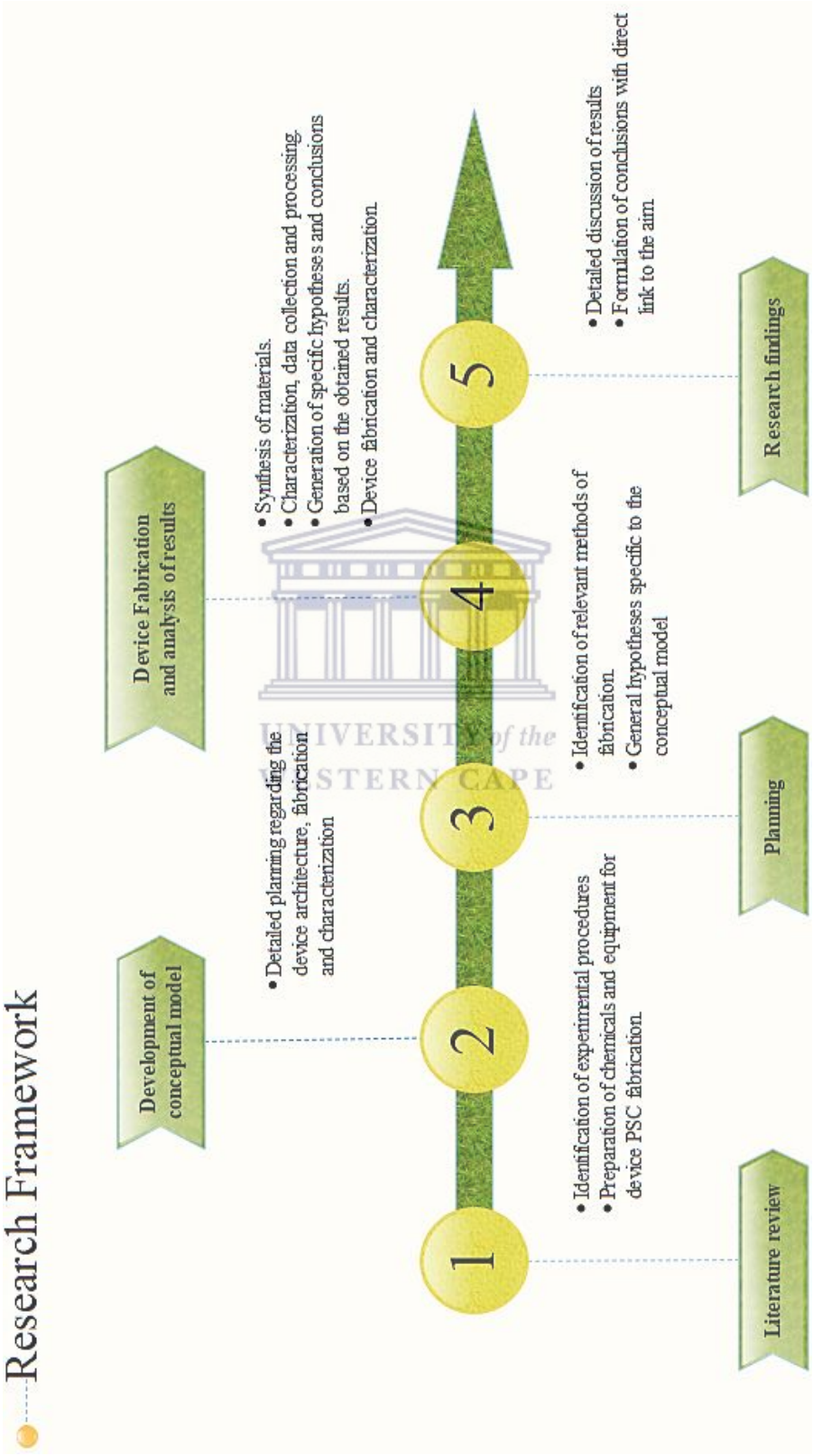

1.2.3 Thesis Outline

The research work is mainly focused on material synthesis, device fabrication and employing different materials and device characterization techniques to evaluate the photovoltaic performance of the perovskite solar cells.

In **Chapter 1**, a well-elaborated depiction of the reasons behind the research and investment into renewable energy and photovoltaic technologies is presented. Particularly, contextual information about perovskite solar cells is given; the device structural design and operating principle of the cells are also discussed. Finally, the aim, as well as the research framework of this project, is laid out.

In **Chapter 2**, an introduction of the theory behind perovskite solar cells and their operation is given. First, an overview of photovoltaics is discussed, followed by a description of perovskite, its properties, device architecture, working principle and then some challenges are also enumerated. The different fabrication processes of perovskite films are then described, together with the different deposition method used for optimal efficiencies. Finally, the main technique for the evaluation and the characterization of solar cells is described.

In **Chapter 3**, a summary of all the materials and characterization instruments used in this thesis is given. The detailed fabrication parameters for both perovskite and interface materials are summarized. Beside the comprehensive solar cell characterization techniques, detailed description of the interface as well as device characterization techniques are also presented.

In **Chapter 4**, an introduction of the results obtained from the different characterization techniques performed, their analysis and discussion is presented. Detailed explanation of the equipment and set up used for the characterization techniques included HR-SEM, HR-TEM,

XRD, EDS, FTIR, UV-Vis, CV and I-V curve measurements. The most important conclusions made were based on calculated photovoltaic parameters.

In **Chapter 5**, a summary of the outcomes of the research done in this thesis are presented. Recommendations with regards to some of the objectives that were not met and the way forward in order to improve the results obtained from the I-V measurements of the solar cells are given.

1.3 References

[1] U.S Energy Information Administration, Annual Energy Outlook 2017 with projections to 2050, 2017.

[2] S. Solomon, G.K. Plattner, R. Knutti, P. Friedlingstein, Irreversible climate change due to carbon dioxide emissions, Proc. Natl. Acad. Sci. U. S. A. 106 (2009) 1704–1709. doi:10.1073/pnas.0812721106.

[3] J. Hansen, M. Sato, P. Kharecha, D. Beerling, R. Berner, V. Masson-Delmotte, M. Pagani, M.L.R. Raymo, J.C. Zachos, Target Atmospheric CO_2: Where Should Humanity Aim? James, NASA. 48 (2011) 1–20.

[4] M. Allen, M. Babiker, Y. Chen, H. de Coninck, S. Connors, R. van Diemen, O.P. Dube, IPCC report Global Warming of 1.5 C: Summary for Policymakers, 2018.

[5] Data world bank, Fossil fuel energy consumption (% of total), World Bank. (2011) 90–91. doi:10.3109/14767058.2012.718390.

[6] Climate Science For Sceptics (CS4S), Historic correlations between global temperatures and atmospheric CO_2 Levels, Is Our Clim. Chang. Why? (2019). http://www.cs4s.net/climate-2.html. (accessed November 28, 2019).

[7] K. Holmberg, A. Erdemir, Influence of tribology on global energy consumption, costs and emissions, Friction. 5 (2017) 263–284. doi:10.1007/s40544-017-0183-5.

[8] World Energy Council [WEC], World Energy Resources: Solar 2016, in: World Energy Counc., 2016: pp. 1–80. doi:https://www.worldenergy.org/wp-content/uploads/2013/10/WER_2013_8_Solar_revised.pdf.

[9] M. Roser, E. Ortiz-Ospina, World Population Growth — Our World in Data, Ourworldindata.Org. (2018). http://ourworldindata.org/data/population-growth-vital-statistics/world-population-growth/.

[10] M.I.H. Ansari, A. Qurashi, M.K. Nazeeruddin, M. Istafaul, H. Ansari, A. Qurashi, M.K. Nazeeruddin, Frontiers, opportunities, and challenges in perovskite solar cells: A critical review, J. Photochem. Photobiol. C Photochem. Rev. 35 (2018) 1–24. doi:10.1016/j.jphotochemrev.2017.11.002.

[11] G. Mørk, S. Barstow, A. Kabuth, M.T. Pontes, ASSESSING THE GLOBAL WAVE ENERGY POTENTIAL ECMWF -European Centre for Medium-Range Weather Forecasts MEDS -Marine Environmental Data Services (Canada) NOAA -National Oceanic and Atmospheric Administration NDBC -National Data Buoy Centre WERATLAS -European, Offshore Mech. Arct. Eng. (2010) 1–8. https://pdfs.semanticscholar.org/d7fd/7fc8b4ec97db3cec84648b3303e9f267b581.pdf.

[12] I.B. Fridleifsson, R. Bertani, E. Huenges, The possible role and contribution of geothermal energy to the mitigation of climate change, IPCC Scoping Meet. Renew. Energy Sources. (2008) 59–80. http://scholar.google.com/scholar?hl=en&btnG=Search&q=intitle:The+possible+role+and+contribution+of+geothermal+energy+to+the+mitigation+of+climate+change#0.

[13] A. Chen, M. Yossef, C. Zhang, Strain effect on the performance of amorphous silicon and perovskite solar cells, Sol. Energy. 163 (2018) 243–250. doi:10.1016/j.solener.2018.01.057.

[14] Solar Generation 6, Solar photovoltaic electricity empowering the world, 2011.

[15] S. Rühle, Tabulated values of the Shockley-Queisser limit for single junction solar cells, Sol. Energy. 130 (2016) 139–147. doi:10.1016/j.solener.2016.02.015.

[16] W.A. Badawy, A review on solar cells from Si-single crystals to porous materials and Quantum dots, J. Adv. Res. 6 (2015) 123–132. doi:10.1016/j.jare.2013.10.001. [16] International Renewable Energy Agency (IRENA), Renewable Power Generation Costs in 2017, 2018. www.irena.org (accessed November 1, 2019).

[17] Multijunction III-V Photovoltaics Research | Department of Energy, (2013). https://www.energy.gov/eere/solar/multijunction-iii-v-photovoltaics-research (accessed February 24, 2020).

[18] efficiency-chart, (n.d.). https://www.nrel.gov/pv/assets/images/efficiency-chart.png.

[19] How products are made, How silicon is made - material, making, history, used, processing, components, composition, structure, product, (2017). http://www.madehow.com/Volume-6/Silicon.html (accessed October 2, 2018).

[20] H. Engül, T.L. Theis, An environmental impact assessment of quantum dot photovoltaics (QDPV) from raw material acquisition through use, J. Clean. Prod. 19 (2011) 21–31. doi:10.1016/j.jclepro.2010.08.010.

[21] M. Grätzel, Recent Advances ins sensitized Mesoscopic Solar Cells, Acc. Chem. Res. 42 (2009) 1788–1798. doi:10.1021/ar900141y.

[22] H.S. Kim, C.R. Lee, J.H. Im, K.B. Lee, T. Moehl, A. Marchioro, S.J. Moon, R. Humphry-Baker, J.H. Yum, J.E. Moser, M. Grätzel, N.G. Park, Lead iodide perovskite sensitized all-solid-state submicron thin film mesoscopic solar cell with efficiency exceeding 9%,

Sci. Rep. 2 (2012). doi:10.1038/srep00591.

[23] J. Tsao, N. Lewis, G. Crabtree, Solar FAQs, US Dep. Energy. (2006) 1–24. https://www.sandia.gov/~jytsao/Solar FAQs.pdf (accessed October 2, 2018).

[24] L. Li, S. Zhang, Z. Yang, E.E.S. Berthold, W. Chen, E. Esso, S. Berthold, W. Chen, Recent advances of flexible perovskite solar cells, J. Energy Chem. 27 (2018) 673–689. doi:10.1016/j.jechem.2018.01.003.

[25] L. Zhang, X. Liu, J. Li, S. Mckechnie, Interactions between molecules and perovskites in halide perovskite solar cells, Sol. Energy Mater. Sol. Cells. 175 (2018) 1–19. doi:10.1016/j.solmat.2017.09.038.

[26] J. Burschka, N. Pellet, S.J. Moon, R. Humphry-Baker, P. Gao, M.K. Nazeeruddin, M. Grätzel, Sequential deposition as a route to high-performance perovskite-sensitized solar cells, Nature. 499 (2013) 316–319. doi:10.1038/nature12340.

[27] L.M. Pazos-Outón, M. Szumilo, R. Lamboll, J.M. Richter, M. Crespo-Quesada, M. Abdi-Jalebi, H.J. Beeson, M. Vrućinić, M. Alsari, H.J. Snaith, B. Ehrler, R.H. Friend, F. Deschler, Photon recycling in lead iodide perovskite solar cells, Science (80-.). 351 (2016) 1430–1433. doi:10.1126/science.aaf1168.

[28] Y. Ogomi, A. Morita, S. Tsukamoto, T. Saitho, Q. Shen, T. Toyoda, K. Yoshino, S.S. Pandey, T. Ma, S. Hayase, All-solid perovskite solar cells with HOCO-R-NH_3+I-anchor-group inserted between porous titania and perovskite, J. Phys. Chem. C. 118 (2014) 16651–16659. doi:10.1021/jp412627n.

[29] G. Xing, N. Mathews, S. Sun, S.S. Lim, Y.M. Lam, M. Graẗzel, S. Mhaisalkar, T.C. Sum,

Long-range balanced electron-and hole-transport lengths in organic-inorganic $CH_3NH_3PbI_3$, Science (80). 342 (2013) 344–347. doi:10.1126/science.1243167.

[30] H.J. Snaith, Perovskites: The emergence of a new era for low-cost, high-efficiency solar cells, J. Phys. Chem. Lett. 4 (2013) 3623–3630. doi:10.1021/jz4020162.

[31] C. Battaglia, A. Cuevas, S. De Wolf, High-efficiency crystalline silicon solar cells: Status and perspectives, Energy Environ. Sci. 9 (2016) 1552–1576. doi:10.1039/c5ee03380b.

[32] A. Polman, M. Knight, E.C. Garnett, B. Ehrler, W.C. Sinke, Photovoltaic materials: Present efficiencies and future challenges, Science (80). 352 (2016). doi:10.1126/science.aad4424.

[33] J. You, L. Meng, T. Bin Song, T.F. Guo, W.H. Chang, Z. Hong, H. Chen, H. Zhou, Q. Chen, Y. Liu, N. De Marco, Y. Yang, Improved air stability of perovskite solar cells via solution-processed metal oxide transport layers, Nat. Nanotechnol. 11 (2016) 75–81. doi:10.1038/nnano.2015.230.

[34] S.D. Stranks, P.K. Nayak, W. Zhang, T. Stergiopoulos, H.J. Snaith, Formation of thin films of organic-inorganic perovskites for high-efficiency solar cells, Angew. Chemie - Int. Ed. 54 (2015) 3240–3248. doi:10.1002/anie.201410214.

[35] I.C. Smith, E.T. Hoke, D. Solis-Ibarra, M.D. McGehee, H.I. Karunadasa, A Layered Hybrid Perovskite Solar-Cell Absorber with Enhanced Moisture Stability, Angew. Chemie - Int. Ed. 53 (2014) 11232–11235. doi:10.1002/anie.201406466.

[36] Y. Rong, L. Liu, A. Mei, X. Li, H. Han, Beyond Efficiency : the Challenge of Stability in Mesoscopic Perovskite Beyond Effi ciency : the Challenge of Stability in Mesoscopic

Perovskite Solar Cells, Adv. Energy Mater. 5 (2015) 1–16. doi:10.1002/aenm.201501066.

[37] A. Kojima, K. Teshima, Y. Shirai, T. Miyasaka, Organometal halide perovskites as visible-light sensitizers for photovoltaic cells, J. Am. Chem. Soc. 131 (2009) 6050–6051. doi:10.1021/ja809598r.

[38] Y. Wu, X. Yang, H. Chen, K. Zhang, C. Qin, J. Liu, W. Peng, A. Islam, E. Bi, F. Ye, M. Yin, P. Zhang, L. Han, Highly compact TiO_2 layer for efficient hole-blocking in perovskite solar cells, Appl. Phys. Express. 7 (2014) 52301. doi:10.7567/APEX.7.052301.

[39] P. Vivo, A. Ojanperä, J.-H. Smått, S. Sandén, S.G. Hashmi, K. Kaunisto, P. Ihalainen, M.T. Masood, R. Österbacka, P.D. Lund, H. Lemmetyinen, Influence of TiO_2 compact layer precursor on the performance of perovskite solar cells, Org. Electron. 41 (2017) 287–293. doi:10.1016/j.orgel.2016.11.017.

[40] B. Peng, G. Jungmann, C. Jäger, D. Haarer, H.-W. Schmidt, M. Thelakkat, Systematic investigation of the role of compact TiO_2 layer in solid state dye-sensitized TiO_2 solar cells, Coord. Chem. Rev. 248 (2004) 1479–1489. doi:10.1016/j.ccr.2004.02.008.

Chapter 2 Literature review

This chapter introduces the theory behind perovskite solar cells and their operation. First, an overview of photovoltaics is discussed, followed by a description of perovskite, its properties, device architecture, working principle and then some challenges are also enumerated. The different fabrication processes of perovskite films are then described, together with the different deposition method used for optimal efficiencies. Finally, the main techniques for the evaluation and the characterization of solar cells are described.

2.1 Overview of photovoltaics

Currently, the world is facing global warming mainly caused by the emission of greenhouse gases resulting from burning coal and oil [1,2]. An important challenge for mankind is to find affordable, clean and sustainable energy sources at large scale to meet today's energy requirements. The energy supplied on the earth by the solar radiation is an efficient and feasible source to harvest and convert into electricity. Photovoltaic (PV) solar cells, capable of converting solar energy directly into electrical energy, are an alternative that have potential to meet the entire world's energy demand [3]. The PV devices can be divided into three categories. (1) First generation solar cell, (2) second generation solar cell and (3) third generation solar cell frequently also termed as future generation solar cells [4]. First generation solar cell mainly consists of silicon (Si) wafers (monocrystalline and polycrystalline). The monocrystalline Si homo-junction and heterojunction cells have 25.1% and 25.6% efficiencies in that order, whereas the polycrystalline Si cells have 20.8% efficiency [5]. Under thermodynamic consideration of detailed balance, the maximum efficiency of Si based single junction solar cells (absence of non-radiative recombination) is restricted to 33.5% for AM1.5G spectrum at 25 °C and referred to as Shockley Queisser (SQ) limit [6]. The AM 1.5 Standard Spectrum describes to two standard terrestrial solar spectral irradiance spectra. The two spectra define a standard direct normal spectral irradiance and a standard total (global, hemispherical, within 2π steradian field of view of the tilted plane at 38^{o} from horizontal) spectral irradiance [7]. At present, silicon solar cells (wafer technology) dominate and take up to 93% [8] of the global PV installation market with PCE of commercial modules of around 20% and lifetime of around 20 years. The cost of silicon modules was redeuced significantly from around 70$/WP in 1970s [9] to ~0.36 $/WP in 2017 [10]. **Figure 2.1** shows the global cumulative photovoltaic installations from 2010 to 2019 [11].

However, the major difficulty is that Si technology requires expensive materials with higher manufacturing temperature, which means that the fabrication is still costly [5,12]. Second generation solar cells are built based on 'thin film' technology that consists of semiconductor materials such as copper indium gallium diselenide (CIGS-21.7%), single crystalline gallium arsenide (GaAs-28.8%) and poly-crystalline cadmium telluride (CdTe-21.5%) showing promising efficiencies [5]. Multi-junction solar cells exceed SQ limit due to several absorber layers for harvesting light in different regions of the solar spectrum and have reached highest power conversion efficiency (PCE) of 38.8% under one sun condition with a five junction (GaInAs/GaInP/GaAs/AlGaInAs/AlGaInP) tandem geometry.

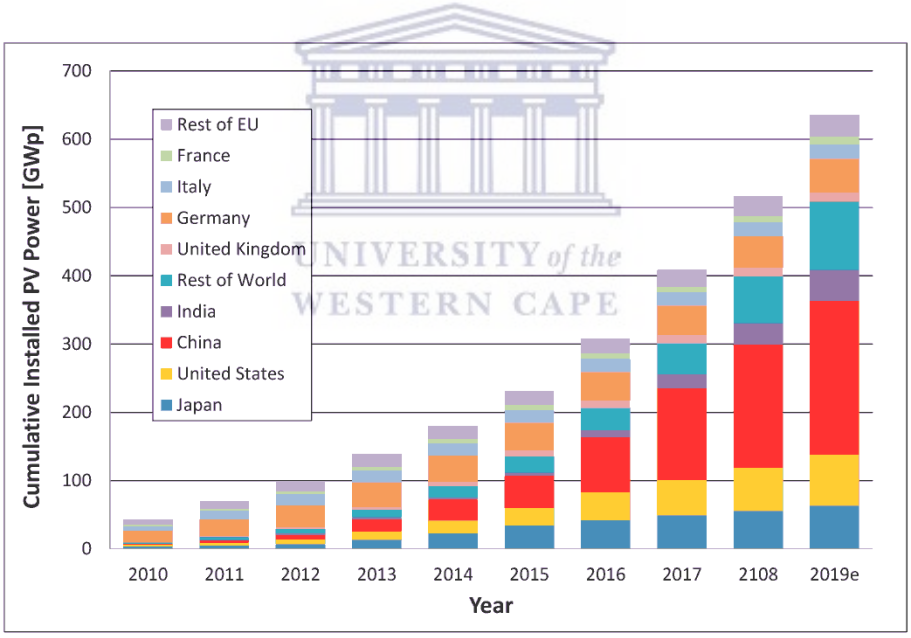

Figure 2.1: Cumulative photovoltaic installations from 2010 to 2019 [11].

Nevertheless, a big challenge for the PV community with these solar cells is the elevated manufacturing cost [5]. **Figure 2.2** shows the best solar cell efficiencies reported so far [13]. Researchers have pushed towards new types of solar cells and developed 'third generation' solar cells to overcome the limitations of the preceding solar cells and tried to decrease high

production cost [4]. Even though, the efficiencies of third generation solar cells are relatively low as compared to Si/multi-junction solar cells, they have low production cost due to cheap fabrication processing techniques. This makes third generation solar cells interesting to the PV community.

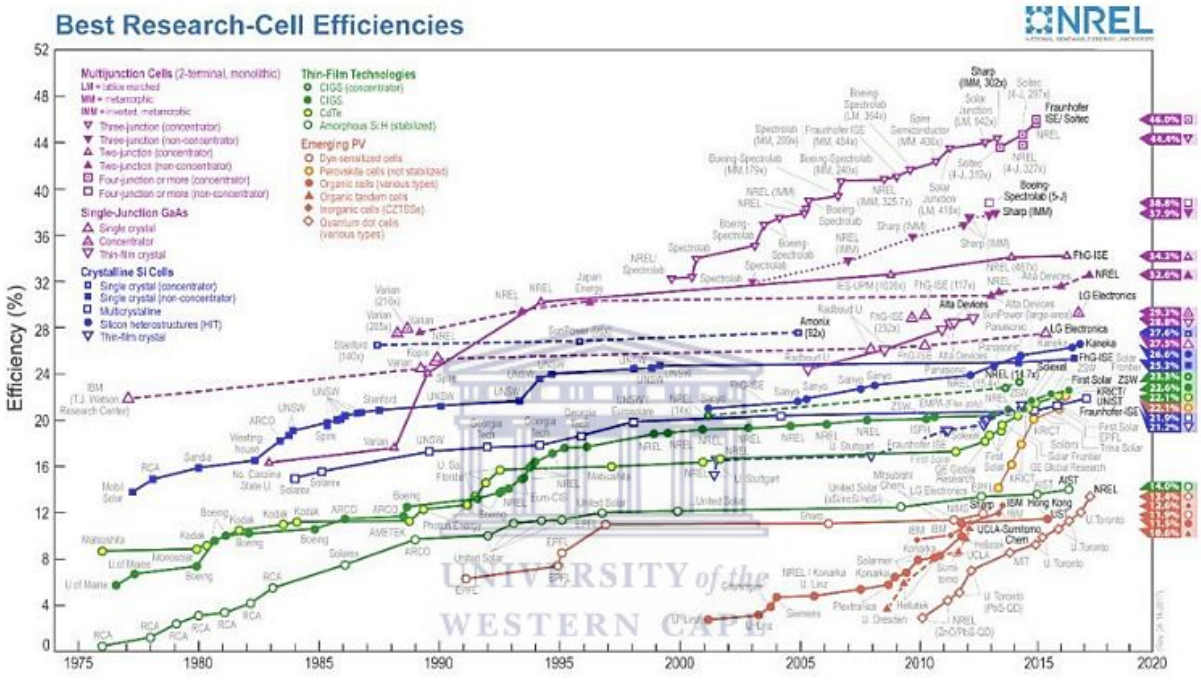

Figure 2.2: Best solar efficiencies, taken from National Renewable Energy Laboratory (NREL) website [14].

Fairly recently, solution processed photovoltaics have started to attract major interest owing to their high power conversion efficiency (PCE), cost effective fabrication, and added functionality such as flexibility, being aesthetic and light weight. In 1991, the first development was based on dye-sensitize solar cells (DSSCs) [15], which now demonstrate 14.3% efficiency [16]. The most recent advance in the field of third generation solar cells is the development of organic-inorganic halide perovskite solar cells that now demonstrate efficiencies of about 22% [17]. Advancement

of perovskite solar cells has been remarkable as these can be fabricated by solution processing at low temperatures and the production requires less energy than Si solar cell. Coupling of PSCs with c-Si and/or CIGS solar cells in tandem geometry is considered a novel approach in order to reduce the overall cost of energy generation (cost-efficiency balance) and also to enhance the PCE of single junction solar cells beyond the SQ limit. Tandem solar cells is possible to be fabricated in three different ways: (1) Mechanically stacked solar cells, termed as 4-terminal (4T), (2) Monolithic solar cells, termed as 2-terminal (2T) and (3) optical splitting tandem solar cell [18]. Recently, 26.4% PCE has been reported with mechanically stacked configuration [19]. A focus on tandem devices is due to their easy integration and printability on existing PV technology, as PSCs can easily be printed via solution processing techniques. A possible additional market advantage of the PSCs is the use of flexible PV technology. It is not only attracting a lot of attention due to the search for low cost manufacturing and high-throughput but also by taking into account its properties of being lightweight, flexible and thin, that would make it easy to integrate on any surface (e.g. building integrated photovoltaics (BIPV), automotive integrated photovoltaics (AIPV)) or structure (either curved, rigid, or flexible) and even in portable and indoor electronics [9]. Notwithstanding the high efficiency accounts, the PSCs still face issues such as: long-term operational stability, toxicity (the most efficient devices employ lead, Pb), and reproducibility. The reproducibility of the performance arises from their rapid crystallization, which largely depends on the fabrication conditions and also the substrate or the selective contacts below them [20]. For a highly efficient device, the choice of selective contacts is important for effective charge extractions as well as its stability as perovskite deposition on metal oxides such as ZnO and TiO_2 has displayed degradation problems due to a possible interfacial reaction [21,22].

2.2 Perovskite solar cells (PSCs)

Perovskite solar cells are a kind of solar cell devices that use perovskite-based material as the light absorbing layer [23].

2.2.1 Properties of perovskites

The original perovskite structure comes from calcium titanium oxide ($CaTiO_3$) with the general structure ABX_3, which is shown in **Figure 2. 3** below.

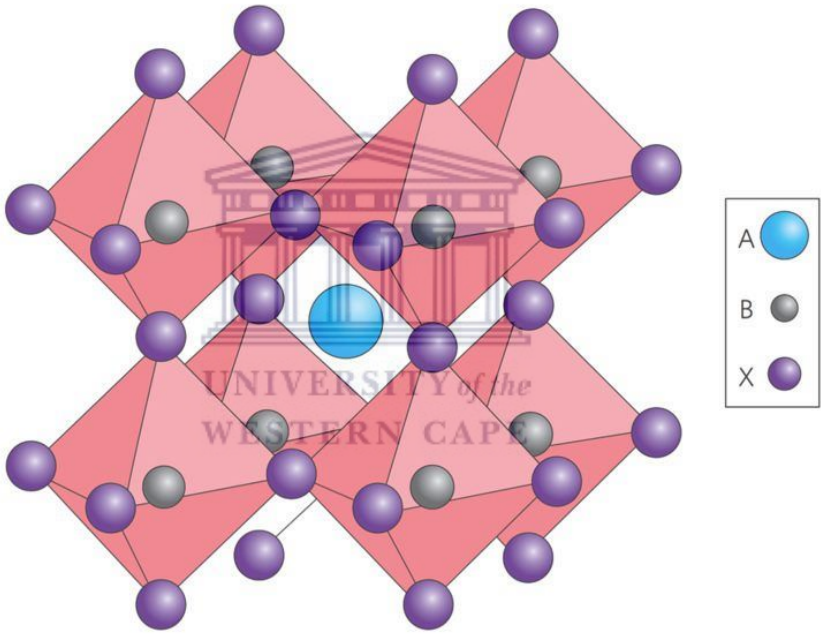

Figure 2. 3: The general perovskite cubical structure ABX_3, where A and B are cations and X is an anion. The anions are bonded to both of the cations [24].

As seen in **Figure 2. 3** A and B are cations with distinct electronegativity and size whereas X is an anion that is bonded to both A and B. It is vital that A atom has lower electronegativity and bigger atomic radius than atom B, due to symmetrical purposes of the crystal cubic structure. Any material with the same crystal structure is called perovskite material. Depending on cations

and anions they show different properties like super conductivity, ionic conductivity, high thermal power etc. The specific combination of materials in perovskite used for photovoltaic cells is called organometallic halides and was first discovered in 1978 by Weber [25]. It consists of organic material like methyl ammonium (MA) or formamidinium (FA) as (A), metal like lead (Pb^{2+}) or tin (Sn^{2+}) as (B) and halide like bromide (Br^-), iodide (I^-) or chloride (Cl^-) as (X_3). The beneficial properties for this perovskite are: low band gap which lets more light be absorbed because a broader spectrum of light has photons with enough energy to excite excitons. It has high charge carrier mobility which lets the created electrons and holes move through the material without much resistance, and a high diffusion length which keeps electron-hole pairs from recombination.

2.2.2 Device Architecture

The first embodiments of perovskite solar cells were based on dye-sensitized solar cell (DSCC) architecture and $CH_3NH_3PbI_3$ (Perovskite) was used as a sensitizer on thick mesoporous scaffolds [26]. It was coupled with liquid electrolyte, which resulted in very limited stability of such devices. This architecture yielded power conversion efficiency (PCE) of 3.8 %. The breakthrough came when an all solid-state architecture was realized with 9% PCE [27]. From then on, PSCs experienced rapid development. The thickness of the mesoporous scaffold decreased by an order of magnitude and it was realized that perovskite can efficiently conduct holes and electrons alike making it a much more conventional semiconductor material than thought initially [28–30]. Since then, the PCEs experienced rapid improvement and within several years of development the values improved beyond 22 %, rivalling more established PV technologies [14].

Today, state-of-the-art perovskite solar cells are typically less than 1 µm thick and contain perovskite sandwiched between hole and electron charge transport layers (HTL and ETL respectively). These are typically placed between a metal electrode (Au, Ag and Al are used most often) and another transparent one such as FTO or ITO (fluorine or indium-doped tin oxide). Often, a mesoporous scaffold is employed on top of the ETL in order to improve the perovskite film quality and charge transport. However, this is optional and "planar" devices have demonstrated similar performances to their scaffold-based counter parts [31,32]. When electrons are collected at the transparent electrode, and holes at the metal one, the device is said to have a "normal" architecture. If the opposite is true, the architecture is called "inverted". So far, the best performing devices employ a "normal" architecture. However, the different choice of charge transporting materials available with "inverted" architectures (notably inorganic ones) means that both architectures enjoy sustained interest of the researchers [33,34].

Figure 1.5 in Chapter showed the architecture of the device fabricate in this work with a mesoporous scaffold-based device with "normal" architecture. The ETL is made of a continuous, thin layer of TiO_2, which is most often deposited on ITO via Spray pyrolysis or spin-coating of the TiO_2 precursor solution. The scaffold is fabricated by spin coating and sintering TiO_2 nanoparticles to form an interconnected mesoporous network. The HTL is Spiro-OMeTAD in this case, which is deposited via spin-coating. The electrode is thermally evaporated and is made of Au. The perovskite is in this case composed of a mixture of different anions and cations. The monovalent cation site is occupied by methyl ammonium ($CH_3NH_3^+$). The metal site is occupied by Pb^{2+} cations. The halogen anion site is occupied by I^-. PSCs based on this composition and architecture are currently amongst the best performing ones. The early successful methods for depositing perovskite involved a two-step formation process in which PbI_2 was first deposited by

spin coating and then converted to $CH_3NH_3PbI_3$ by dipping in CH_3BH_3I solution [35]. However, this deposition method did not allow for precise composition control and soon a single-step method was devised [36]. That method involves spin-coating perovskite solution in one-step. Before the drying of the film is complete, it was washed with an anti-solvent to induce fast and homogenous crystallization. Alternatively, quick drying under vacuum can be employed [37]. To this date, most PSCs are fabricated via one-step, anti-solvent method. However, perovskite can also be thermally evaporated [38,39], which can be useful for certain experiments where solvents could dissolve the underlying layers.

2.2.2.1 Compact layer

One of the key components of the mesoscopic perovskite solar cells is the compact layer. Its role is to stop direct contact between the HTM and the FTO layers, which could potentially result in a short circuit inside the cell. In addition, it blocks the holes generated within the perovskite layer or HTM layers from reaching the FTO anode, which could have a negative on the net current that can be obtained from the cell because the holes are gathered at the cathode. Essentially the compact layer acts as a guide for the electrons and holes towards their respective electrodes, it reduces the chances of charge carrier recombination from occurring. As the connecting area between the FTO layer and the perovskite or HTM layers is reduced, so is the recombination process. The presence of pinholes in the compact layer decreases the solar cell efficiency by allowing a contact between the materials. The most used compact layer material is titania [40,41].

There are several ways in which the titania compact layer can be deposited. These methods include techniques such as spin-coating from a precursor solution, spray-pyrolysis, and atomic

layer deposition [42]. The compact layer deposition is done on a transparent conducting oxide (TCO) substrate. TCO is usually FTO, since it adheres well to titania. The compact layer should be as thin as possible, because a larger layer implies higher resistance, and thus lower fill factor and charge collection [43].

2.2.2.2 Mesoporous metal oxide

Inorganic semiconductor materials are used to produce different and complex nanostructures. Titania is widely used in photovoltaic devices because of its desired properties such as non-toxicity, its high chemical stability, low cost, intense photocatalytic activity, and high photoelectric conversion efficiency [44].

Mesoscopic perovskite solar cells use an n-type mesoporous semiconducting layer. To introduce excited electrons from perovskite to the mesoporous layer, the oxide layer should have lower conduction band than the excited state of perovskite. The n-type mesoporous material is typically made up of titania nanoparticles. Titania extracts electrons that have been generated in perovskite layer. It also increases the perovskite crystal transformation when sequential deposition method is employed. Mesoporous titania layers can be fabricated by spin-coating, screen-printing, and doctor-blading [42].

Titania has three accepted crystal structures: rutile, anatase and brookite. The structures are shown in **Figure 2.** 4. Rutile which is the most common and most stable of these three structures. It is also chemically inert and it can be excited by visible and ultraviolet light. Brookite and anatase are metastable forms. Anatase transform into rutile at high temperatures and it can be excited only by ultraviolet light. Brookite is not excited by light. Brookite can only turn into rutile by heating. Anatase turns into rutile in air around 500 °C. Pure anatase is considered to

widely begin transforming irreversibly to rutile in air at around 600 ^{o}C; however, the reported transition temperatures vary in the range 400–1200 ^{o}C depending on the methods used, the raw materials, and processing conditions [45].

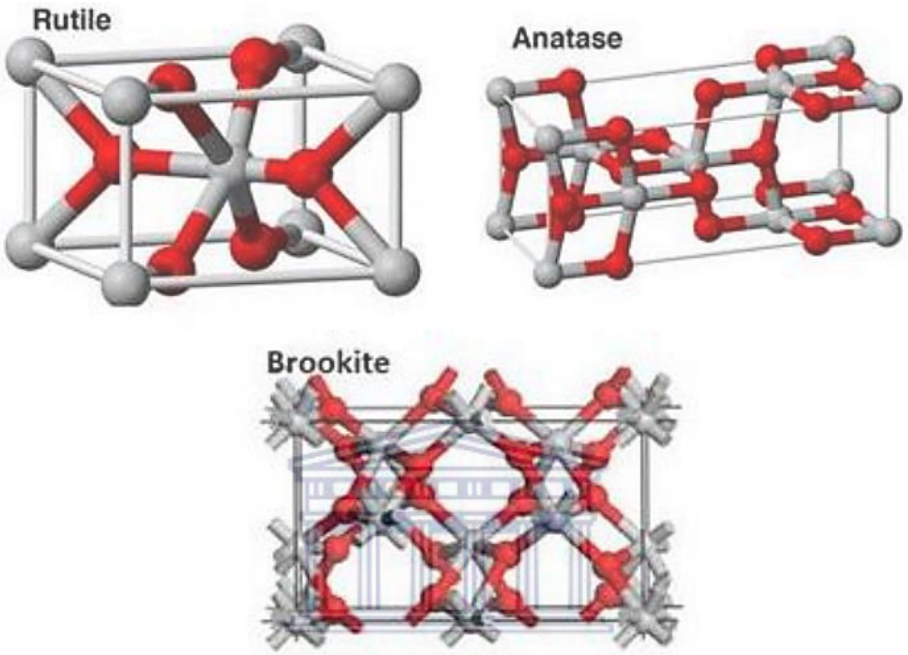

Figure 2. 4: Crystal Structures of rutile, anatase and brookite. Titanium atoms are depicted as gray spheres, while oxygen atoms are depicted as red spheres [46].

Titania is often used in anatase- or rutile form in mesoscopic solar cells [42]. Anatase titania particles are known to be the most successfully used nanostructure in the mesoscopic perovskite solar cells. TiO_2 in the anatase phase has wider bandgap of approximately 3.2 eV as opposed to the rutile phase which has a band gap of approximately 3 eV. TiO_2 in the anatase phase also shows superior photo-catalytic performance than rutile (more stable). Charge carrier recombination in anatase happens at a much slower rate than rutile by approximately a factor of 10 which is due to smaller grain-sizes in anatase phase [45]. Nonetheless, the devices with rutile particles have higher electron diffusion coefficients and faster charge carrier recombination. In

addition to nanoparticles also other structures, such as Nano rods and Nano sheets, has been studied.

Many other metal oxides, like zinc oxide (ZnO) and alumina (Al_2O_3), can also used in mesoporous perovskite solar cells [42]. In this research work only, n-type anatase titania is employed as the metal oxide mesoporous layer material.

2.2.2.3 Hole transport layer

The holes pass through the hole transport materials to the metal cathode. HTMs are theoretically not mandatory in perovskite solar cells. However, their use results in much higher efficiencies in perovskite solar cells, which makes them even more essential in a good cell. HTMs block the back-electron transfer and lead to higher fill factors and open circuit voltages. Both organic and inorganic hole conductors can be used as HTMs [47].

A capping layer of HTM could be useful for high-performance perovskite solar cells in order to disrupt the contact between the perovskite and cathode. Preferably, HTM should have a high hole- mobility, and good thermal- and UV- stabilities. It should also match with the HOMO level of the perovskite [48].

At present, 2,2',7,7'-tetrakis(N,N-di-p-methoxyphenylamine)-9,9'-spirobifluorene (spiro-OMeTAD) remains the best and most widely used HTM candidate for perovskite solar cells [42]. Its molecular structure is shown in **Figure 2.5**. However, spiro-OMeTAD is prohibitively expensive because of its onerous multistep synthesis that requires very low temperature (-78 °C), and because of the sensitive (n-butyl lithium or Grignard reagents) and aggressive (Br_2) reagents involved in the synthetic scheme. This restrains its up-scale application in the photovoltaic

industry. From the commercialization point of view, the development of efficient yet cost-effective HTMs is the major challenge for the advancement of hybrid perovskite solar cells technology [49].

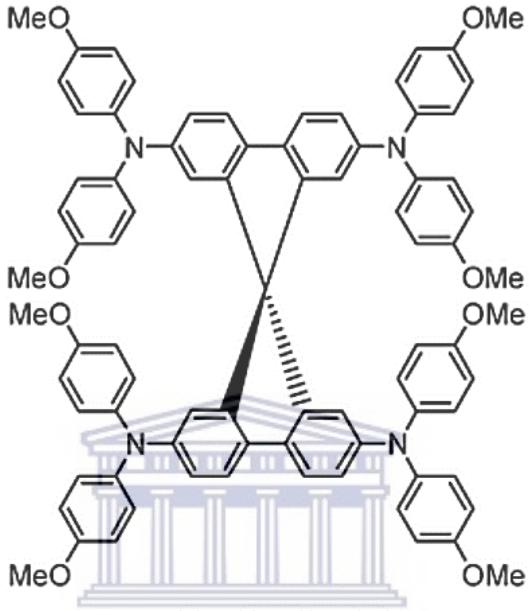

Figure 2.5: The structural formula of spiro-OMeTAD.

If spiro-OMeTAD is used as HTM in its pristine form, the resulting solar cells would have a high series resistance, using spiro-OMeTAD alone without dopants results poor charge transport properties. In fact, spiro-OMeTAD is normally combined with p-dopants, to enhance the charge transport properties [50]. p-doping is a method to enhance the conductivity of organic semiconductors by creating additional charge-carriers, which results in higher charge-carrier density [51].

HTM conductivity can be enhanced drastically by chemical oxidants, such as tris(2-(1H-pyrazol-1- yl)pyridine)cobalt(III) which is also known FK 102 Co(III) (PF_6) salt. Co(III) complexes are

efficient p- dopants of spiro-OMeTAD, and their addition leads to lower series-resistance in the solar cell [35,51,52].

Bis(trifluoro-methane)sulfonimide lithium salt (LiTFSI) and tert-butyl pyridine (tBP) are widely used additives. Li cations increase the electronic conductivity of spiro-OMeTAD via a catalyzed oxidative process. LiTFSI improves considerably the conductivity and the hole mobility of spiro-OMeTAD. The open circuit voltage of solar cells is enhanced by addition of tBP. Li cations and tBP influence several processes in the solar cells such as the electron transport and the recombination rates. Their general effect on HTM is complex and its thorough description goes beyond the scope of this work [52,53]. However, a key aspect to remember is that tBP and Li cations promote an energy level shift in the spiro-OMeTAD layer. Also, Li cation has been reported to catalyze the complex doping mechanism in which spiro-MeOTAD oxidizes, resulting in an HTL with high conductivity while L cation is consumed [54].

The molecular structures of the commonly used dopants, LiTFSI, tBP and PF_6 salt, are presented in **Figure 2.6**. These 3 dopants are employed in the solar cells fabricated in this work.

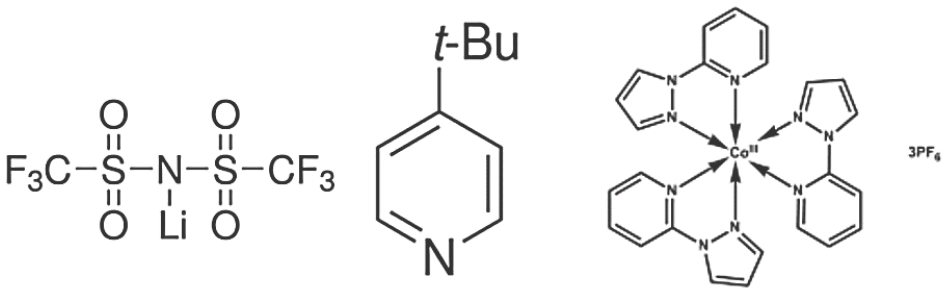

Figure 2.6: Structural formulas and molecular structure of LiTFSI, tBP, and FK 102.

As previously mentioned, it is not compulsory to use HTMs in perovskite solar cells. Since perovskite acts both as a light harvester and hole conductor, a p-n junction can be formed

between n-type metal oxides and perovskite in mesoscopic perovskite solar cells. The nonexistence of a HTM could potentially enhance the stability, lower the production costs and enable the fabrication [42]. If the HTM is left out, the perovskite layer should be thick and have a smoother surface to avoid shunt contacts and ensure good light absorption [55].

2.2.2.4 Cathode

The counter electrode gathers the electrons from the external circuit and the holes transported by the HTM. It should have high conductivity for charge transport, good electro-catalytic activity, and high stability. The most used counter electrode materials are noble metals, such as platinum, silver and gold. Predominantly, gold and silver are effective hole collectors to be used with the commonly adopted HTM materials. The most important drawback for the use of noble metals is their high cost [56].

2.2.3 Working principle

The PSC operation is described in the schematic shown in **Figure 2.7**.

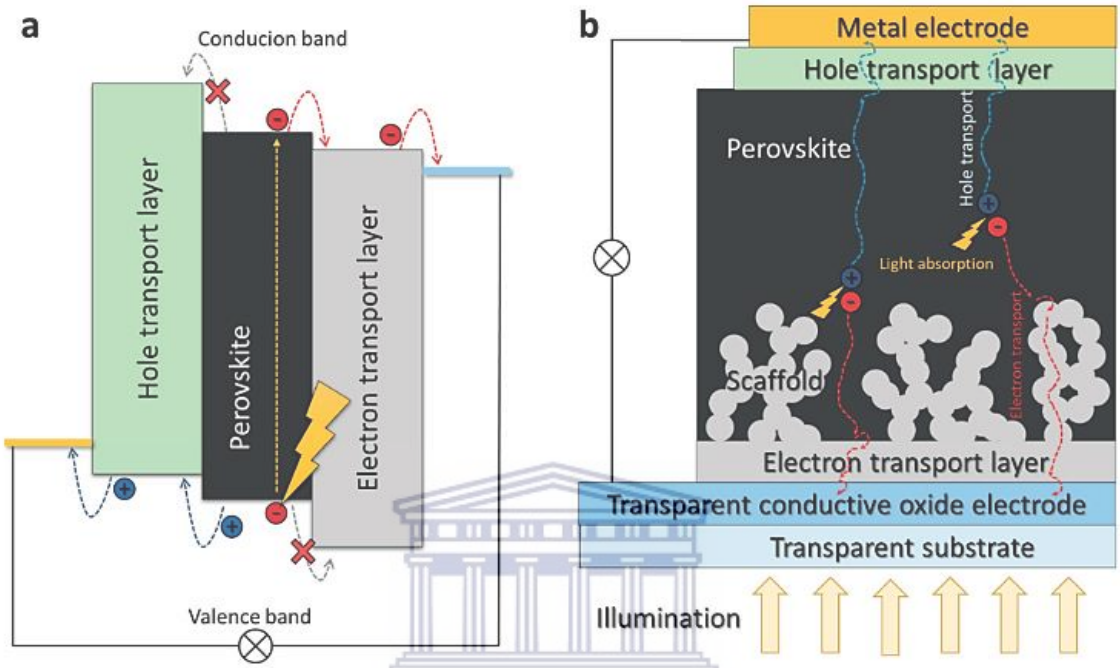

Figure 2.7: Working principles of PSCs with: a) Schematic energy diagram of a PSC. b) Schematics of the 'normal' architecture PSC with mesoporous scaffold. [57].

Photons from a light source, shown as yellow arrows, reach the perovskite layer through the glass and the transparent electrode as well as the electron transport layer. In the active perovskite layer, the photon is absorbed and excites an exciton if the photon's energy is above the energy gap of the perovskite material. The exciton is separated to free charge carriers by the internal potential created from the work function difference between the transparent electrode and the metallic electrode. The electrons are transported to the ETL while the holes are transported to the HTL. From there the electrons are transported to the transparent electrode and the hole to the metallic electrode. Then the electron moves through the wire connecting the two electrodes and a

current is produced by the moving electrons. In the metallic electrode the electron and hole recombine.

For the PSC to function properly the energy levels for each layer need to be carefully planned. Because the excited electrons and holes want to recombine in order to minimize the total energy, but the charge carriers are also energy conservers, which mean they will always take the path of minimum resistance. With the right layer structure some of the recombination in the cell will be blocked by letting the charge carriers take a different route. This is done by having the ETL's LUMO a bit lower than the active layer's LUMO which creates a more attractive way for the electron to go. The same is true for the HTL's HOMO that needs to be a bit higher than the active layer's HOMO which creates a more attractive way for holes to go. This is same for every layer in the cell, each layer has either higher HOMO or lower LUMO for the charge carrier's transportation chain to work as seen in **Figure 2.7** above.

2.2.4 Challenges with perovskite solar cells

In spite of significant achievements in the PCE of PSCs, stability is one of the critical issue that needs to be addressed prior to its commercial deployment. Stability depends on numerous factors, both intrinsic, such as perovskite structural and chemical stability and extrinsic, such as moisture, oxygen, light and heat that limit their life-time to few hundred hours only [58,59].

For any solar cell technology to be commercialized, operational stability and inexpensive manufacturing methods have to be demonstrated alongside high PCE as shown schematically in **Figure 2.8**. The use of abundant starting materials and inexpensive manufacturing techniques makes perovskite solar cells potentially very price competitive [60–63].

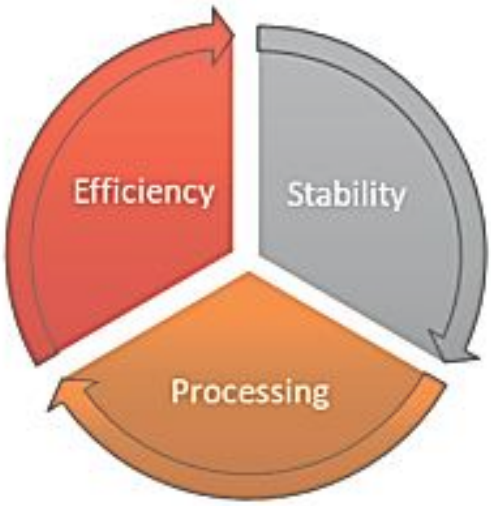

Figure 2.8: The "Holy Grail" of photovoltaic technologies that is efficient, stable and inexpensive to manufacture.

Perovskite ($CH_3NH_3PbX_3$) materials are stable, both chemically and structurally, but due to the hygroscopic nature of the organic cation, moisture induced degradation happens. Substituting or mixing of MA cation with cesium and/or formamidinium can improve the stability of perovskite towards moisture and heat [64,65]. A recent study using FTIR spectroscopy shows that evaporation of MAI during film fabrication itself initiates the instability, suggesting that the active layer film fabrication methodology is an essential step for the stability of PSCs [66].

Additionally, the question of how to measure the stability of PSCs has to be tackled. Here the ionic motion and J-V hysteresis create an additional obstacle. Hysteresis is directly related to ionic motion in the perovskite and the nature of contacts that can affect the PV characteristics (i.e., variation in the J-V curves for different scan rates), and it is detrimental to the device stability [59]. Oxidation and photo-oxidation have been seen for perovskite films but are less severe in full devices, depending on the hydrophobic nature of the top layer [67], and can be

avoided by appropriate encapsulation under inert conditions that enables solar cells to be stable for up to 1000 h [68].

2.3 Fabrication Methods

A large factor contributing to the costs of solar cell production lies directly within the production techniques themselves. Silicon solar cells require extensive amounts of processing and extremely high temperatures. Silicon solar cells have increased in magnitude and become streamlined; however, they are still limited by those production costs. Organic solar cells as well have promising efficiency potentials, have corresponding cheap production options and processing techniques encompassed by roll to roll processing.

2.3.1 Roll to Roll Processing

Roll to Roll (R2R) processing is an over encompassing title for several more specific processes, and is the ability to manufacture product using flexible substrates and create continuous product production. The immediate benefits of this process are the streamlined methods that do not require excessive labor or even necessarily the transfer of material from one process to another. There are several specific methods that can be placed one after another in R2R manufacturing line to complete a final product [69].

2.3.1.1 Chemical Vapor Deposition

Chemical vapor deposition, or CVD, is a chemical process that causes volatile precursors in the gas phase to form a solid layer on the target surface. Generally, CVD takes place at low pressures because the particles being deposited tend to exists as liquids in normal conditions. The conventional method of CVD is thermally activated CVD, which causes the chemical reaction to

happen by a change in temperature. Another common method is photo-initiated CVD, which triggers the deposition by the addition of light, usually UV causing the monomers to layer on the substrate [70].

2.3.1.2 Physical Vapor Deposition

Very similar in principle to CVD, physical vapor deposition (PVD) relies more on physical interactions than chemical ones. Like CVD there are subsets of PVD, sputter deposition specifically is the ejection of particles into a vacuum chamber. Particles are usually ejected by a continuous flow of argon gas which is usually converted to plasma, i.e. Ar^+ ions. The particles being sent into the vacuum are subject to a negative potential while the target substrate is grounded; this leads the ejected particles to evenly coat the substrate in a very thin layer of a conductive material. PVD coatings offer the benefits of improved hardness and oxidation resistance as well as a smooth layer, which is most beneficial for the solar cell process [71].

2.3.1.3 Solution Based Processing

As suggested by the name this process involves creating a solution with the desired material dissolved into a soluble substance. That solution is then spread onto the surface where the layer is to be coated to a desired thickness; the solution is then either treated or heated to evaporate the processing solvent. This method can be paired with spin coating to achieve a desired thickness of a material; however, spin coating is not conducive to R2R processing [72].

2.3.1.4 Doctor Blading

Doctor Blading is a process common in R2R processing where the substrate and a deposited solvent are either dragged under, or held while a blade drags over. The blade is at a fixed

distance from the material the solvent is added to, this distance determines the thickness of the doctor bladed layer. In R2R setups on a larger scale the doctor blade is at a set distance from a large cylinder where the flexible substrate and solvent are passed, the blade removes excess solvent leaving a thin film. Common for lab practices is a second technique where the substrate has two very thin buffers attached with a gap in between. The solvent is placed in the gap and the doctor blade is pulled along the buffers, leaving a film the thickness of whatever was used as a buffer [73,74].

2.3.1.5 Sol Gel process

Sol gel processing is a common method for synthesizing nanoparticles because it can be done at low temperatures compared to other methods. At a chemical level, the process involves reacting a base material with another solution over a specific amount of time to produce a sol, a solution with suspended nanoparticles. The addition of the secondary solution relies on the use of a titrator to accurately "drip" the solution into the other over a calculated time. The sol gel process relies on specific stoichiometric principles to produce these nanoparticles. ZnO particles are a common example of a sol that is produced via sol gel processing [75].

2.3.2 Spin-Coating

When depositing a thin film onto a substrate especially in a laboratory setting spin coating is often used because of its benefits in uniformity. This application method uses centrifugal forces on a disk spinning at high speeds to create an even coating on a substrate. The layer thickness is heavily dependent on viscosity, speed of the spinner, and the time the material is allowed to spin for [76]. There have also been applications of spin coating that use gas assisted methods which have been shown to produce smoother crystallization and reduce drying time of a substance onto

the substrate [74]. A downside of using spin coating is that much of the material is wasted, leaving only about 10% of the solution utilized [77]. It is also very impractical for large scale manufacturing.

2.4 Device Characterization

It is important to evaluate the solar cell performance with reliable measurements, in order to compare different materials and technologies. There are several parameters, which characterize the performance of solar cells, such as the short circuit current density, the open circuit voltage, the fill factor, and the energy conversion efficiency [78].

The wavelength range emitted by the sun goes from the ultraviolet and visible to the infrared. Ozone of the atmosphere filters out part of the ultraviolet light. Water and carbon dioxide filter out mainly the infrared light and cause some dropped irradiance peaks to the solar spectrum. The sun has the shortest path length through the atmosphere when it is directly overhead. In that case, the maximum radiation can strike the Earth if the sky is clear. The path length is called the air mass (AM). Its approximated value is

$$\mathrm{AM} = \frac{1}{\cos\varphi} \qquad \text{Equation (1)}$$

where φ is the angle of elevation of the Sun. The standard solar spectrum is AM1.5G (global) for the solar cell efficiency measurements. The spectrum is normalized in a way that the integrated irradiance, i.e. the radiant energy flux per unit area, is 1000 W m^{-2}. Sunlight scatters in the atmosphere, thus causing light diffusion. The fraction of the diffuse light is on average 15 %. Rough surfaces can collect the diffuse light better than the flat ones [79]. The AM1.5G solar irradiation spectrum is presented in **Figure 2.9**.

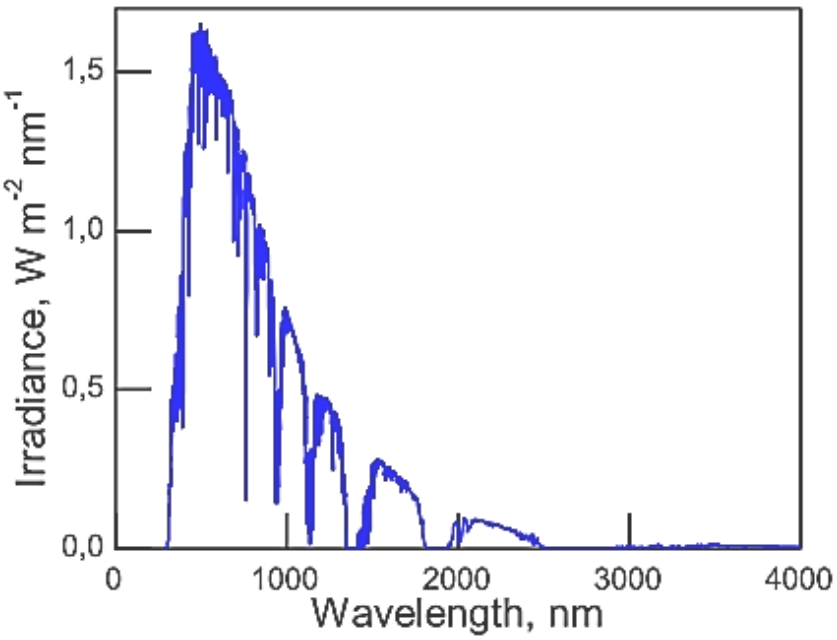

Figure 2.9: AM1.5G solar irradiation spectrum [80].

Traditionally, the performance of solar cells is evaluated by measuring their current density-voltage (I-V) characteristics. In the measurement photocurrent values are recorded as the bias voltage is changed stepwise. The short circuit current, I_{sc}, and the open circuit voltage, V_{oc}, can be directly determined from the recorded I-V curve. The short circuit current density, J_{sc} is obtained by dividing the short circuit current by the irradiated area [78]. The short circuit current density gives the maximum current density, which can be obtained from the solar cell at short circuit conditions, i.e. a condition in which the electrical power to a circuit is supplied at a low resistance between two conductors [81]. Other important parameters, such as the fill factor, FF, and the energy conversion efficiency, η, can be determined using the I-V measurement data [78]. A I-V curve is depicted in **Figure 2. 10**, where the open-circuit voltage, short-circuit current-density and the maximum power point are also indicated.

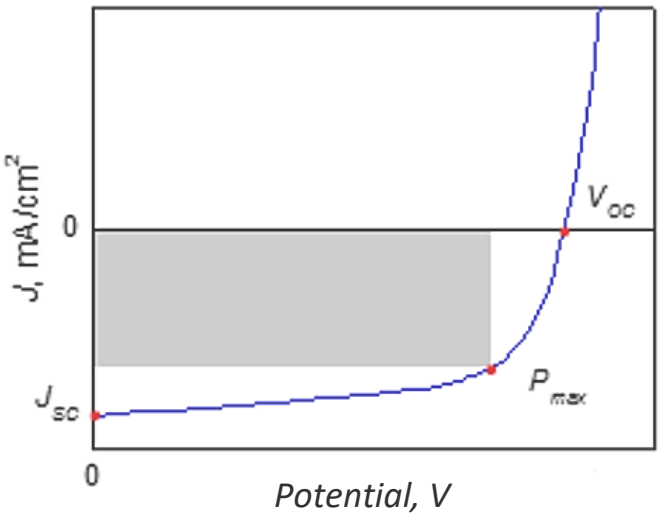

Figure 2. 10: I-V curve.

In **Figure 2.** 10 above, P_{max} is maximum power, i.e. the product of photocurrent and photo-voltage at that voltage where the power output is at its maximum. The fill factor indicates the 'squareness' of the I-V curve [81]. Its value can be determined from the equation

$$FF = \frac{P_{max}}{I_{SC}V_{OC}} \qquad \text{Equation (2)}$$

The value of the fill factor lies between 0 and 1 [79]. The ideal value is 1, but in practice this cannot be achieved due to physical constraints on the diode quality in the solar cell. The main reason for the deviation from the ideal behavior is the recombination occurring at the junction, which can be described in terms of series and shunt resistances. The increase in the series resistance indicates poor conductivity through the active layers and reduced charge carrier injection to the electrodes. The reduced shunt resistance is due to either imperfections within the photoactive layers or current leaks at the interface between layers in the solar cell [81].

The energy conversion efficiency is

$$\eta = \frac{I_{SC}V_{OC}FF}{P_{in}A_{cell}} = \frac{J_{SC}V_{OC}FF}{P_{in}} \quad \text{Equation (3)}$$

Where P_{in} is the irradiance of the incident light on the surface of a cell, A_{cell} is the area, which is irradiated by incident light [78]. The record efficiency for perovskite solar cells is 20.1 ± 0.4 %. The champion cell has open circuit voltage of 1.059 V, the short circuit current density of 24.65 mA/cm^2, and the fill factor of 77 % [82].

Solar cells can be also characterized with incident photon-to-current conversion efficiency, IPCE, i.e. external quantum efficiency. IPCE describes the photocurrent density produced in the external circuit under monochromatic illumination divided by the photon flux, eΦ, which encounters the cell. IPCE is determined as

$$\text{IPCE} = \frac{J_{SC}(\lambda)}{e\phi(\lambda)} = 1240\frac{J_{SC}[A\ cm^{-2}]}{\lambda[nm]P_{in}(\lambda)[W cm^{-2}]} \quad \text{Equation (4)}$$

Where, λ is the wavelength.

2.4.1 Measuring perovskite solar cell performance

There are various factors to be taken into consideration in order to measure the performance of perovskite solar cells accurately. The main issue is the hysteresis in I-V curves, which is affected by the measurement setup and by the solar cell construction. The hysteresis is different for every cell. The origin of the hysteresis is not yet understood. Erroneous interpretation and representation of the performances can be avoided by following certain guidelines [83,84].

In general, the I-V curves are obtained by sweeping the potential difference between the working and counter electrode and monitoring the current response simultaneously. The sweep rate should be carefully selected for each device, preferably about 140 sweep points for a time between sweeps of 10 ms. If the sweep rate is faster than the response time of the device, the

recorded curve does not show steady-state performance. The direction of the sweep causes hysteresis in the I-V curves. **Figure 2.12** shows the effect of the sweep rate. The steady-state output gives the actual values that are used to obtain the different parameters used in the calculation of the PCE. **Figure 2.11** presents also the effect of scan direction. The real output of the device lies between the forward and reverse scan curves [84].

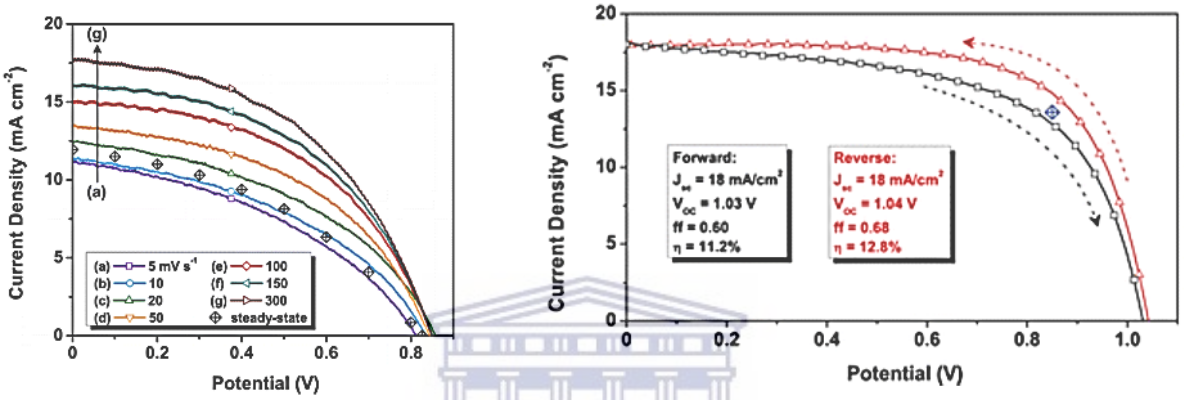

Figure 2.11: An example of the effect of the sweep rate (left) and the scan direction (right) to the I-V curve [84].

The measured current density values can be verified by measuring and integrating the IPCE spectra over the AM1.5G solar spectrum. The integrated current density is

$$J_{SC,INT} = \frac{F \times \int (E_{e\lambda} \times IPCE) d\lambda}{N_A} \quad \text{Equation (5)}$$

where N_A is the Avogadro constant, F the Faraday constant, and $E_{e\lambda}$ the solar spectral irradiance. The integrated and measured current density values should be approximately equivalent if the measurements have been executed carefully [84].

The solar cells should be masked right before the measurements. This avoids the under- and overestimations of the cell performance [84]. Masking also allows for reproducibility of the

measurements. A mask should have a single aperture through which the light enters the cell. This prevents the light entering the cell from elsewhere [85].

To conclude, the following recently published guidelines should be followed when an accurate evaluation of the device's performance is desired. The measured cell needs to be masked, the measurement position, i.e. the distance between the source and the cell should be always exactly same, and the illumination source must be calibrated. The steady-state values for J_{sc} and V_{oc} have to be determined, and the stability monitored. J-V should be measured at various scan rates in both forward and reverse directions. The determined current density is finally checked by calculating the corresponding value from the IPCE data [84,85].

2.5 References and Bibliography

[1] R.S. Lindzen, Taking GreenHouse Warming Seriously, Energy Environ. 18 (2007) 937–950. doi:10.1260/095830507782616823.

[2] M. Lallanilla, Greenhouse Gas Emissions: Causes & Sources, Livescience. (2015). https://www.livescience.com/37821-greenhouse-gases.html.

[3] N.S. Lewis, D.G. Nocera, Powering the planet: Chemical challenges in solar energy utilization, Proc. Natl. Acad. Sci. 103 (2006) 15729–15735. doi:10.1073/pnas.0603395103.

[4] G. Conibeer, Third-generation photovoltaics, Mater. Today. 10 (2007) 42–50. doi:10.1016/S1369-7021(07)70278-X.

[5] A. Polman, M. Knight, E.C. Garnett, B. Ehrler, W.C. Sinke, Photovoltaic materials: Present efficiencies and future challenges, Science (80). 352 (2016). doi:10.1126/science.aad4424.

[6] M.H. Futscher, B. Ehrler, Efficiency Limit of Perovskite/Si Tandem Solar Cells, ACS Energy Lett. 1 (2016) 863–868. doi:10.1021/acsenergylett.6b00405.

[7] PV Performance Modeling Collaborative | AM 1.5 Standard Spectrum, (n.d.). https://pvpmc.sandia.gov/modeling-steps/1-weather-design-inputs/irradiance-and-insolation-2/spectral-content/am-1-5-standard-spectrum/ (accessed February 24, 2020).

[8] F. ISE, Photovoltaics Report, 2018. doi:20.10.2016.

[9] F. Di Giacomo, A. Fakharuddin, R. Jose, T.M. Brown, Progress, challenges and perspectives in flexible perovskite solar cells, Energy Environ. Sci. 9 (2016) 3007–3035.

doi:10.1039/c6ee01137c.

[10] N. Rinaldi, Solar PV Module Costs to Fall to 36 Cents per Watt by 2017, Greentech Media. (2013). www.greentechmedia.com/research/report/pv-technology-and-cost-outlook-2013-2017.

[11] A. Jäger-Waldau, Snapshot of Photovoltaics—February 2019 †, Energies Commun. 12 (2019) 769. doi:10.3390/en12050769.

[12] M.A. Green, Advanced Solar Energy Conversion, in: Third Gener. Photovoltaics, Springer Berlin Heidelberg, 2003: pp. 1–6. doi:10.1007/3-540-26563-5_1.

[13] NREL, Best Research-Cell Efficiency Chart | Photovoltaic Research | NREL, Best Res. Effic. Chart | Photovolt. Res. | NREL. (2019) https://www.nrel.gov/pv/cell-efficiency.html. https://www.nrel.gov/pv/cell-efficiency.html (accessed February 25, 2020).

[14] National Renewable Energy Laboratory, Best research-cell efficiencies, “The Natl. Cent. Photovoltaics Natl. Renew. Energy Lab. (NREL).” (2017). doi:10.1016/j.jet.2007.03.008.

[15] B. O’Regan, M. Grätzel, A low-cost, high-efficiency solar cell based on dye-sensitized colloidal TiO_2 films, Nature. 353 (1991) 737–740. doi:10.1038/353737a0.

[16] K. Kakiage, Y. Aoyama, T. Yano, K. Oya, J.I. Fujisawa, M. Hanaya, Highly-efficient dye-sensitized solar cells with collaborative sensitization by silyl-anchor and carboxy-anchor dyes, Chem. Commun. 51 (2015) 15894–15897. doi:10.1039/c5cc06759f.

[17] W.S. Yang, B.W. Park, E.H. Jung, N.J. Jeon, Y.C. Kim, D.U. Lee, S.S. Shin, J. Seo, E.K. Kim, J.H. Noh, S. Il Seok, Iodide management in formamidinium-lead-halide-based

perovskite layers for efficient solar cells, Science (80). 356 (2017) 1376–1379. doi:10.1126/science.aan2301.

[18] Q. Wali, N.K. Elumalai, Y. Iqbal, A. Uddin, R. Jose, Tandem perovskite solar cells, Renew. Sustain. Energy Rev. 84 (2018) 89–110. doi:10.1016/j.rser.2018.01.005.

[19] T. Duong, Y.L. Wu, H. Shen, J. Peng, X. Fu, D. Jacobs, E.C. Wang, T.C. Kho, K.C. Fong, M. Stocks, E. Franklin, A. Blakers, N. Zin, K. McIntosh, W. Li, Y.B. Cheng, T.P. White, K. Weber, K. Catchpole, Rubidium Multication Perovskite with Optimized Bandgap for Perovskite-Silicon Tandem with over 26% Efficiency, Adv. Energy Mater. 7 (2017). doi:10.1002/aenm.201700228.

[20] A. Fakharuddin, F. De Rossi, T.M. Watson, L. Schmidt-Mende, R. Jose, Research Update: Behind the high efficiency of hybrid perovskite solar cells, APL Mater. 4 (2016) 91505. doi:10.1063/1.4962143.

[21] A. Djuriˇ, Improving the performance of ZnO-based perovskite solar cells, SPIE. (2012) 7–9.

[22] T. Leijtens, G.E. Eperon, S. Pathak, A. Abate, M.M. Lee, H.J. Snaith, Overcoming ultraviolet light instability of sensitized TiO_2 with meso-superstructured organometal tri-halide perovskite solar cells, Nat. Commun. 4 (2013). doi:10.1038/ncomms3885.

[23] Y. Li, High Performance Perovskite Hybrid Solar Cell Via Interfacial Engineering, 2016. doi:10.1017/CBO9781107415324.004.

[24] J.L. Miller, Defect physics in perovskite solar cells, Phys. Today. (2014). doi:10.1063/PT.5.7058.

[25] D. Weber, $CH_3NH_3PbX_3$, ein Pb(II)-System mit kubischer Perowskitstruktur $CH_3NH_3PbX_3$, a Pb(II)-System with Cubic Perovskite Structure, Z. Naturforsch. 33 (1978) 1443–1445. http://zfn.mpdl.mpg.de/data/Reihe_B/33/ZNB-1978-33b-1443.pdf (accessed November 26, 2018).

[26] A. Kojima, K. Teshima, Y. Shirai, T. Miyasaka, Organometal halide perovskites as visible-light sensitizers for photovoltaic cells, J. Am. Chem. Soc. 131 (2009) 6050–6051. doi:10.1021/ja809598r.

[27] H.S. Kim, C.R. Lee, J.H. Im, K.B. Lee, T. Moehl, A. Marchioro, S.J. Moon, R. Humphry-Baker, J.H. Yum, J.E. Moser, M. Grätzel, N.G. Park, Lead iodide perovskite sensitized all-solid-state submicron thin film mesoscopic solar cell with efficiency exceeding 9%, Sci. Rep. 2 (2012). doi:10.1038/srep00591.

[28] G. Xing, N. Mathews, S. Sun, S.S. Lim, Y.M. Lam, M. Graẗzel, S. Mhaisalkar, T.C. Sum, Long-range balanced electron-and hole-transport lengths in organic-inorganic $CH_3NH_3PbI_3$, Science (80). 342 (2013) 344–347. doi:10.1126/science.1243167.

[29] S.D. Stranks, G.E. Eperon, G. Grancini, C. Menelaou, M.J.P. Alcocer, T. Leijtens, L.M. Herz, A. Petrozza, H.J. Snaith, Electron-hole diffusion lengths exceeding 1 micrometer in an organometal trihalide perovskite absorber, Science (80-.). 342 (2013) 341–344. doi:10.1126/science.1243982.

[30] M.M. Lee, J. Teuscher, T. Miyasaka, T.N. Murakami, H.J. Snaith, Efficient hybrid solar cells based on meso-superstructured organometal halide perovskites, Science (80-.). 338 (2012) 643–647. doi:10.1126/science.1228604.

[31] E.H. Anaraki, A. Kermanpur, L. Steier, K. Domanski, T. Matsui, W. Tress, M. Saliba, A.

Abate, M. Grätzel, A. Hagfeldt, J.P. Correa-Baena, Highly efficient and stable planar perovskite solar cells by solution-processed tin oxide, Energy Environ. Sci. 9 (2016) 3128–3134. doi:10.1039/c6ee02390h.

[32] J.P. Correa Baena, L. Steier, W. Tress, M. Saliba, S. Neutzner, T. Matsui, F. Giordano, T.J. Jacobsson, A.R. Srimath Kandada, S.M. Zakeeruddin, A. Petrozza, A. Abate, M.K. Nazeeruddin, M. Grätzel, A. Hagfeldt, Highly efficient planar perovskite solar cells through band alignment engineering, Energy Environ. Sci. 8 (2015) 2928–2934. doi:10.1039/c5ee02608c.

[33] C.G. Wu, C.H. Chiang, Z.L. Tseng, M.K. Nazeeruddin, A. Hagfeldt, M. Grätzel, High efficiency stable inverted perovskite solar cells without current hysteresis, Energy Environ. Sci. 8 (2015) 2725–2733. doi:10.1039/c5ee00645g.

[34] C.-H. Chiang, Z.-L. Tseng, C.-G. Wu, Planar heterojunction perovskite/PC $_{71}$ BM solar cells with enhanced open-circuit voltage via a (2/1)-step spin-coating process, J. Mater. Chem. A. 2 (2014) 15897–15903. doi:10.1039/C4TA03674C.

[35] J. Burschka, N. Pellet, S.J. Moon, R. Humphry-Baker, P. Gao, M.K. Nazeeruddin, M. Grätzel, Sequential deposition as a route to high-performance perovskite-sensitized solar cells, Nature. 499 (2013) 316–319. doi:10.1038/nature12340.

[36] N.J. Jeon, H. Noh, W.S. Yang, Y.C. Kim, S. Ryu, J. Seo, S. Il Seok, Compositional engineering of perovskite materials for high-performance solar cells, Nature. 517 (2014). doi:10.1038/nature14133.

[37] X. Li, D. Bi, C. Yi, J.D. Décoppet, J. Luo, S.M. Zakeeruddin, A. Hagfeldt, M. Grätzel, A vacuum flash-assisted solution process for high-efficiency large-area perovskite solar

cells, Science (80). 353 (2016) 58–62. doi:10.1126/science.aaf8060.

[38] Y. Liu, Z. Hong, Q. Chen, H. Chen, W.H. Chang, Y.M. Yang, T.B. Song, Y. Yang, Perovskite Solar Cells Employing Dopant-Free Organic Hole Transport Materials with Tunable Energy Levels, Adv. Mater. 28 (2016) 440–446. doi:10.1002/adma.201504293.

[39] M. Liu, M.B. Johnston, H.J. Snaith, Efficient planar heterojunction perovskite solar cells by vapour deposition, Nature. 501 (2013) 395–398. doi:10.1038/nature12509.

[40] Y. Wu, X. Yang, H. Chen, K. Zhang, C. Qin, J. Liu, W. Peng, A. Islam, E. Bi, F. Ye, M. Yin, P. Zhang, L. Han, Highly compact TiO_2 layer for efficient hole-blocking in perovskite solar cells, Appl. Phys. Express. 7 (2014) 52301. doi:10.7567/APEX.7.052301.

[41] X. Wang, Y. Fang, L. He, Q. Wang, T. Wu, Influence of compact TiO_2 layer on the photovoltaic characteristics of the organometal halide perovskite-based solar cells, Mater. Sci. Semicond. Process. 27 (2014) 569–576. doi:10.1016/j.mssp.2014.07.039.

[42] S. Shi, Y. Li, X. Li, H. Wang, Advancements in all-solid-state hybrid solar cells based on organometal halide perovskites, Mater. Horizons. 2 (2015) 378–405. doi:10.1039/c4mh00236a.

[43] N. Park, Organometal Perovskite Light Absorbers Toward a 20 % E ffi ciency Low-Cost Solid-State Mesoscopic Solar Cell, J. Phys. Chem. Lett. 4 (2013) 2423–2429. doi:10.1021/jz400892a.

[44] X. Fan, M. Zhang, X. Wang, F. Yang, X. Meng, Recent progress in organic-inorganic hybrid solar cells, J. Mater. Chem. A. 1 (2013) 8694–8709. doi:10.1039/c3ta11200d.

[45] D.A.H. Hanaor, C.C. Sorrell, Review of the Anatase to Rutile Phase Transformation

Review of the anatase to rutile phase transformation, J. Mater. Sci. 46 (2011) 855–874. doi:10.1007/s10853-010-5113-0.

[46] D.A.H. Hanaor, C.C. Sorrell, Review of the anatase to rutile phase transformation, J. Mater. Sci. 46 (2011) 855–874. doi:10.1007/s10853-010-5113-0.

[47] Y. Zhang, W. Liu, F. Tan, Y. Gu, The essential role of the poly(3-hexylthiophene) hole transport layer in perovskite solar cells, J. Power Sources. 274 (2015) 1224–1230. doi:10.1016/j.jpowsour.2014.10.145.

[48] Z. Yang, W.-H. Zhang, Organolead halide perovskite: A rising player in high-efficiency solar cells, Chinese J. Catal. 35 (2014) 983–988. doi:10.1016/S1872-2067(14)60162-5.

[49] P. Gratia, A. Magomedov, T. Malinauskas, M. Daskeviciene, A. Abate, S. Ahmad, M. Grätzel, V. Getautis, M.K. Nazeeruddin, A Methoxydiphenylamine-Substituted Carbazole Twin Derivative: An Efficient Hole-Transporting Material for Perovskite Solar Cells, Angew. Chemie - Int. Ed. 54 (2015) 11409–11413. doi:10.1002/anie.201504666.

[50] S. Kazim, M.K. Nazeeruddin, M. Grätzel, S. Ahmad, Perovskite as light harvester: A game changer in photovoltaics, Angew. Chemie - Int. Ed. 53 (2014) 2812–2824. doi:10.1002/anie.201308719.

[51] J. Burschka, A. Dualeh, F. Kessler, E. Baranoff, N.L. Cevey-Ha, C. Yi, M.K. Nazeeruddin, M. Grätzel, Tris(2-(1 H -pyrazol-1-yl)pyridine)cobalt(III) as p-type dopant for organic semiconductors and its application in highly efficient solid-state dye-sensitized solar cells, J. Am. Chem. Soc. 133 (2011) 18042–18045. doi:10.1021/ja207367t.

[52] P. Docampo, S. Guldin, T. Leijtens, N.K. Noel, U. Steiner, H.J. Snaith, Lessons Learned:

From Dye-Sensitized Solar Cells to All-Solid-State Hybrid Devices, Adv. Mater. 26 (2014) 4013–4030. doi:10.1002/adma.201400486.

[53] A. Abate, T. Leijtens, S. Pathak, J. Teuscher, R. Avolio, M.E. Errico, J. Kirkpatrik, J.M. Ball, P. Docampo, I. McPherson, H.J. Snaith, Lithium salts as “redox active” p-type dopants for organic semiconductors and their impact in solid-state dye-sensitized solar cells, Phys. Chem. Chem. Phys. 15 (2013) 2572–2579. doi:10.1039/c2cp44397j.

[54] E.J. Juarez-perez, M.R. Leyden, S. Wang, L.K. Ono, Z. Hawash, Y. Qi, Role of the Dopants on the Morphological and Transport Properties of Spiro-MeOTAD Hole Transport Layer, Chem. Mater. 28 (2016) 5702–5709. doi:10.1021/acs.chemmater.6b01777.

[55] A. Ojanperä, Mesoscopic perovkite solar cells: efficiency enhancement via optimization of the titania anode, Tampere University of Technology, 2015.

[56] M. Ye, X. Wen, M. Wang, J. Iocozzia, N. Zhang, C. Lin, Z. Lin, Recent advances in dye-sensitized solar cells: From photoanodes, sensitizers and electrolytes to counter electrodes, Mater. Today. 18 (2015) 155–162. doi:10.1016/j.mattod.2014.09.001.

[57] K. Domanski, The Quest for Stability of Perovskite Solar Cells : Understanding Degradation , Improving Lifetimes and Towards Experimental Standards PAR, 2018.

[58] Y. Yuan, J. Chae, Y. Shao, Q. Wang, Z. Xiao, A. Centrone, J. Huang, Photovoltaic Switching Mechanism in Lateral Structure Hybrid Perovskite Solar Cells, Adv. Energy Mater. 5 (2015). doi:10.1002/aenm.201500615.

[59] E. Erdenebileg, L.E. Scholz, A. Hofacker, C. Koerner, K. Leo, Very Small Inverted

Hysteresis in Vacuum-Deposited Mixed Organic–Inorganic Hybrid Perovskite Solar Cells, Energy Technol. 5 (2017) 1606–1611. doi:10.1002/ente.201700002.

[60] J.H. Noh, S.H. Im, J.H. Heo, T.N. Mandal, S. Il Seok, Chemical management for colorful, efficient, and stable inorganic-organic hybrid nanostructured solar cells, Nano Lett. 13 (2013) 1764–1769. doi:10.1021/nl400349b.

[61] J. Xiong, B. Yang, R. Wu, C. Cao, Y. Huang, C. Liu, Z. Hu, H. Huang, Y. Gao, J. Yang, Efficient and non-hysteresis CH3NH3PbI3/PCBM planar heterojunction solar cells, Org. Electron. 24 (2015) 106–112. doi:10.1016/J.ORGEL.2015.05.028.

[62] K. Kara, D.A. Kara, C. Kirbiyik, M. Ersoz, O. Usluer, A.L. Briseno, M. Kus, Solvent washing with toluene enhances efficiency and increases reproducibility in perovskite solar cells, RSC Adv. 6 (2016) 26606–26611. doi:10.1039/c5ra27122c.

[63] D. Shen, X. Yu, X. Cai, M. Peng, Y. Ma, X. Su, L. Xiao, D. Zou, Understanding the solvent-assisted crystallization mechanism inherent in efficient organic-inorganic halide perovskite solar cells, J. Mater. Chem. A. 2 (2014) 20454–20461. doi:10.1039/c4ta05635c.

[64] Y. Shao, Z. Xiao, C. Bi, Y. Yuan, J. Huang, Origin and elimination of photocurrent hysteresis by fullerene passivation in $CH_3NH_3PbI_3$ planar heterojunction solar cells, Nat. Commun. 5 (2014). doi:10.1038/ncomms6784.

[65] J.M. Frost, K.T. Butler, A. Walsh, Molecular ferroelectric contributions to anomalous hysteresis in hybrid perovskite solar cells, APL Mater. 2 (2014). doi:10.1063/1.4890246.

[66] W. Tress, J.P. Correa Baena, M. Saliba, A. Abate, M. Graetzel, Inverted Current–Voltage

Hysteresis in Mixed Perovskite Solar Cells: Polarization, Energy Barriers, and Defect Recombination, Adv. Energy Mater. 6 (2016). doi:10.1002/aenm.201600396.

[67] A.K. Jena, H.W. Chen, A. Kogo, Y. Sanehira, M. Ikegami, T. Miyasaka, The interface between FTO and the TiO<inf>2</inf> compact layer can be one of the origins to hysteresis in planar heterojunction perovskite solar cells, ACS Appl. Mater. Interfaces. 7 (2015) 9817–9823. doi:10.1021/acsami.5b01789.

[68] A. Dualeh, T. Moehl, N. Tétreault, J. Teuscher, P. Gao, M.K. Nazeeruddin, M. Grätzel, Impedance spectroscopic analysis of lead iodide perovskite-sensitized solid-state solar cells, ACS Nano. 8 (2014) 362–373. doi:10.1021/nn404323g.

[69] Proceedings of the International Conference for High Performance Computing, Networking, Storage and Analysis, SC 2017, Proc. Int. Conf. High Perform. Comput. Networking, Storage Anal. SC 2017. (2017).

[70] C.A. Dorval Dion, J.R. Tavares, Photo-initiated chemical vapor deposition as a scalable particle functionalization technology (a practical review), Powder Technol. 239 (2013) 484–491. doi:10.1016/j.powtec.2013.02.024.

[71] N. Selvakumar, H.C. Barshilia, Review of physical vapor deposited (PVD) spectrally selective coatings for mid- and high-temperature solar thermal applications, Sol. Energy Mater. Sol. Cells. 98 (2012) 1–23. doi:10.1016/j.solmat.2011.10.028.

[72] W. Nie, H. Tsai, R. Asadpour, J.C. Blancon, A.J. Neukirch, G. Gupta, J.J. Crochet, M. Chhowalla, S. Tretiak, M.A. Alam, H.L. Wang, A.D. Mohite, High-efficiency solution-processed perovskite solar cells with millimeter-scale grains, Science (80-.). 347 (2015) 522–525. doi:10.1126/science.aaa0472.

[73] K. Xiong, L. Hou, M. Wu, Y. Huo, W. Mo, Y. Yuan, S. Sun, W. Xu, E. Wang, From spin coating to doctor blading: A systematic study on the photovoltaic performance of an isoindigo-based polymer, Sol. Energy Mater. Sol. Cells. 132 (2015) 252–259. doi:10.1016/j.solmat.2014.08.039.

[74] Y. Lin, C. Cai, Y. Zhang, W. Zheng, J. Yang, E. Wang, L. Hou, Study of ITO-free roll-to-roll compatible polymer solar cells using the one-step doctor blading technique, J. Mater. Chem. A. 5 (2017) 4093–4102. doi:10.1039/c6ta10018j.

[75] Siswanto, N.T. Rochman, P.R. Akwalia, Fabrication and characterization of Zinc Oxide (ZnO) nanoparticle by sol-gel method, in: J. Phys. Conf. Ser., 2017. doi:10.1088/1742-6596/853/1/012041.

[76] L.E. Scriven, Physics and Applications of DIP Coating and Spin Coating, MRS Proc. 121 (1988). doi:10.1557/proc-121-717.

[77] F. Huang, Y. Dkhissi, W. Huang, M. Xiao, I. Benesperi, S. Rubanov, Y. Zhu, X. Lin, L. Jiang, Y. Zhou, A. Gray-Weale, J. Etheridge, C.R. McNeill, R.A. Caruso, U. Bach, L. Spiccia, Y.B. Cheng, Gas-assisted preparation of lead iodide perovskite films consisting of a monolayer of single crystalline grains for high efficiency planar solar cells, Nano Energy. 10 (2014) 10–18. doi:10.1016/j.nanoen.2014.08.015.

[78] X. Yang, M. Yanagida, L. Han, Reliable evaluation of dye-sensitized solar cells, Energy Environ. Sci. 6 (2013) 54–66. doi:10.1039/c2ee22998f.

[79] R. Ameta, S. Benjamin, S. Sharma, M. Trivedi, Dye-sensitized solar cells, in: Sol. Energy Convers. Storage Photochem. Modes, 2015. doi:10.1201/b19148.

[80] The National Renewable Energy Laboratory (NREL), Reference Solar Spectral Irradiance: Air Mass 1.5, Am. Soc. Test. Mater. - Terr. Ref. Spectra Photovolt. Perform. Eval. (2012). doi:10.1016/j.appdev.2008.12.009.

[81] M. Wright, A. Uddin, Organic-inorganic hybrid solar cells: A comparative review, Sol. Energy Mater. Sol. Cells. 107 (2012) 87–111. doi:10.1016/j.solmat.2012.07.006.

[82] M.A. Green, Corrigendum to 'Solar cell efficiency tables (version 46)' [Prog. Photovolt: Res. Appl. 2015; 23: 805-812], Prog. Photovoltaics Res. Appl. 23 (2015) 1202–1202. doi:10.1002/pip.2667.

[83] S.D. Stranks, H.J. Snaith, Metal-halide perovskites for photovoltaic and light-emitting devices, Nat. Nanotechnol. 10 (2015) 391–402. doi:10.1038/nnano.2015.90.

[84] J.A. Christians, J.S. Manser, P. V. Kamat, Best practices in perovskite solar cell efficiency measurements. Avoiding the error of Making Bad Cells Look Good, J. Phys. Chem. Lett. 6 (2015) 852–857. doi:10.1021/acs.jpclett.5b00289.

[85] H.J. Snaith, How should you measure your excitonic solar cells?, Energy Environ. Sci. 5 (2012) 6513–6520. doi:10.1039/c2ee03429h.

Chapter 3 Experimental method

This chapter is mostly dedicated to the description of the methods and investigation techniques used in the development of the experiments done in this thesis. In particular, in the first part a full description of the materials and chemicals used in this research work is given. Meticulous fabrication parameters for both perovskite and the interface materials are summarized. Part of this chapter is also dedicated to the preparation of the samples and photovoltaic devices for the Perovskite-based solar cells. Beside the comprehensive solar cell characterization techniques explained, complete interface characterization techniques are also provided in the chapter.

3.1 Materials

3.1.1 Active layer

The reagents and solvents used to prepare the perovskite precursors comprising lead iodide (99.9%), methyl ammonium iodide (99.9%), terephtalic acid (99.9%), dimethylformamide and dimethyl sulfoxide both with purity of 99.99%, were purchased from Sigma Aldrich and used as received.

3.1.2 Interface layer

The reagents and solvents used to prepare the ETMs comprising titanium tetraisopropoxide (99.9%), titanium(IV) oxide nanoparticles (99.9%), ethanol (99.9%) and silver nitrate (99.9%), were purchased from Sigma Aldrich and used as received. Deionized water was prepared with Millipore filtration system (Millipore-Sigma)

The reagents and solvents used to prepare the HTMs comprising spiro-OMeTAD (≥99.0%), chlorobenzene (99.9%), acetonitrile (99.9%), lithium bis(trifluoromethanesufonyl)imide and 4-tert-butylpyridine (99.9%), were purchased from Sigma Aldrich and used as received.

3.1.3 Substrates

ITO substrates were used to fabricate the devices as shown in **Figure 3.1** and were purchased from Ossila with the specifications listed in the **Table. 3.1**. This particular type of patterned ITO substrates was used because it was better adapted to the type of metal deposition mask available in our labs (Multi-electrode mask from Ossila).

The solvents used to clean the substrates comprising a 2% solution of Hellmanex III, isopropanol (99%) and methanol (99%) were purchased from Sigma Aldrich and used as received. Deionized water was prepared with Millipore filtration system.

Table 3.1: ITO substrate specifications.

Substrate size	20 mm x 15 mm
Thickness	1.1 mm
Glass type	Polished soda lime, float glass
Substrate coating	Fully oxidized ITO
ITO thickness	100 nm
ITO resistance	14 Ω / square
Glass roughness	< 1nm RMS (By AFM)
ITO roughness	1.8 nm RMS (By AFM)

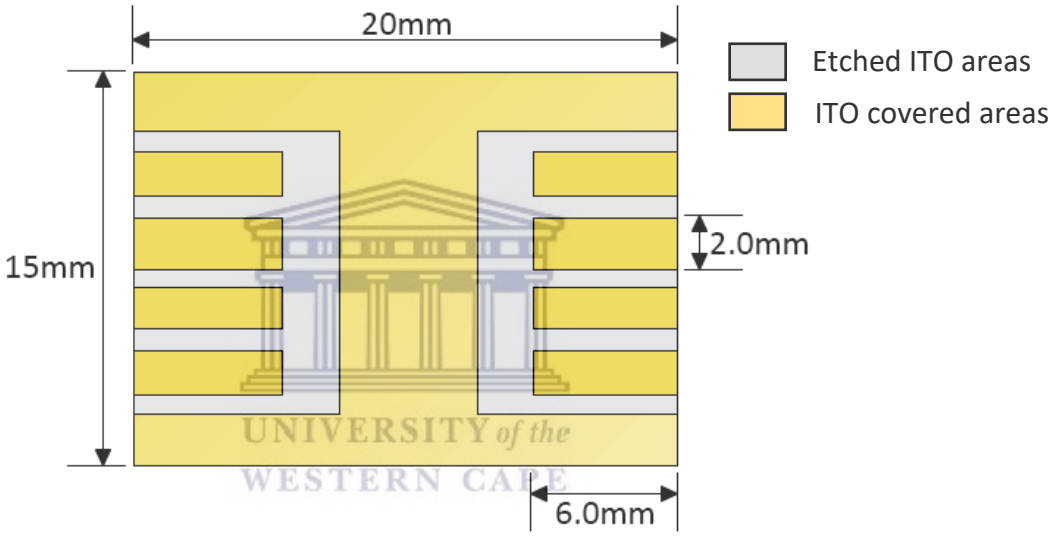

Figure 3.1: ITO pattern and substrates dimensions.

3.2 Device fabrication

The fabrication process of the devices required building upon and readjusting several methods found in research in terms the materials and laboratory tools available. The following section will look into the final processing that was used to formulate each solution and resulting solar cell layers.

In this work a non-vacuum deposition technique namely spin-coating was used. The deposition involved preparation the different precursor solutions for the individual layers forming part of

the device architecture in a suitable solvent and spin coating them onto ITO glass layer by layer, then subsequently anneal the ITO glass to evaporate the solvents. In order to carry out the fabrication of the perovskite solar cell devices, the architecture described in **Figure 3. 2** was used

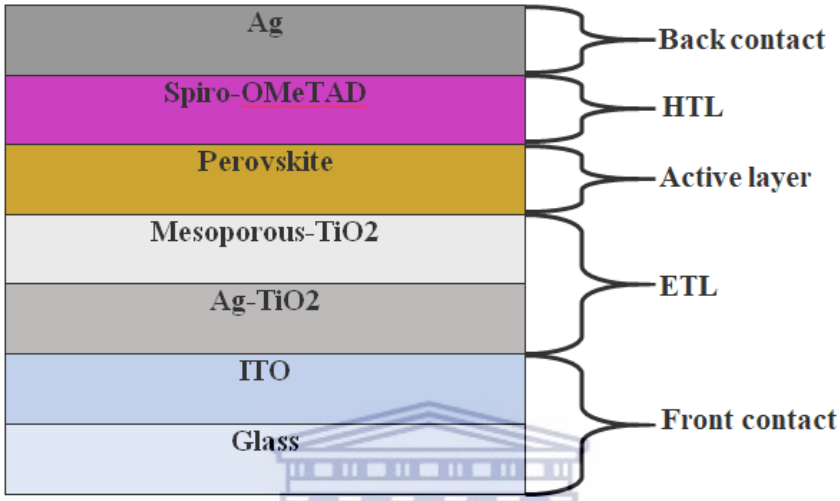

Figure 3. 2: Device architecture.

3.2.1 Substrate cleaning

The cleaning process was done as follows:

i. The ITO substrates were sonicated for 10 minutes in a hot mixture of the Hellmanex III solution and distilled water in 1:100 volume ratio.

ii. Next the substrates were washed with a sponge in petri dish containing a mixture of distilled water, acetone and isopropanol in volume ratio of 1:1:1.

iii. The substrates were then sonicated in a petri dish containing the previously mentioned solution mixture for 10 minutes.

iv. Step 3 was repeated three times without waiting periods in between.

v. The substrates were taken out of the petri dish individually with a pair of tweezers and dried using compressed air in a fume hood until visibly dry.

vi. Finally the substrates were placed in a closed glass vial and stored.

3.2.2 Solar cells layer processing and deposition parameters

Before deposition of the layers, the substrates were temporarily masked with kapton tape on both ends to allow for only the central part to be uncovered as depicted in **Figure 3.3** below:

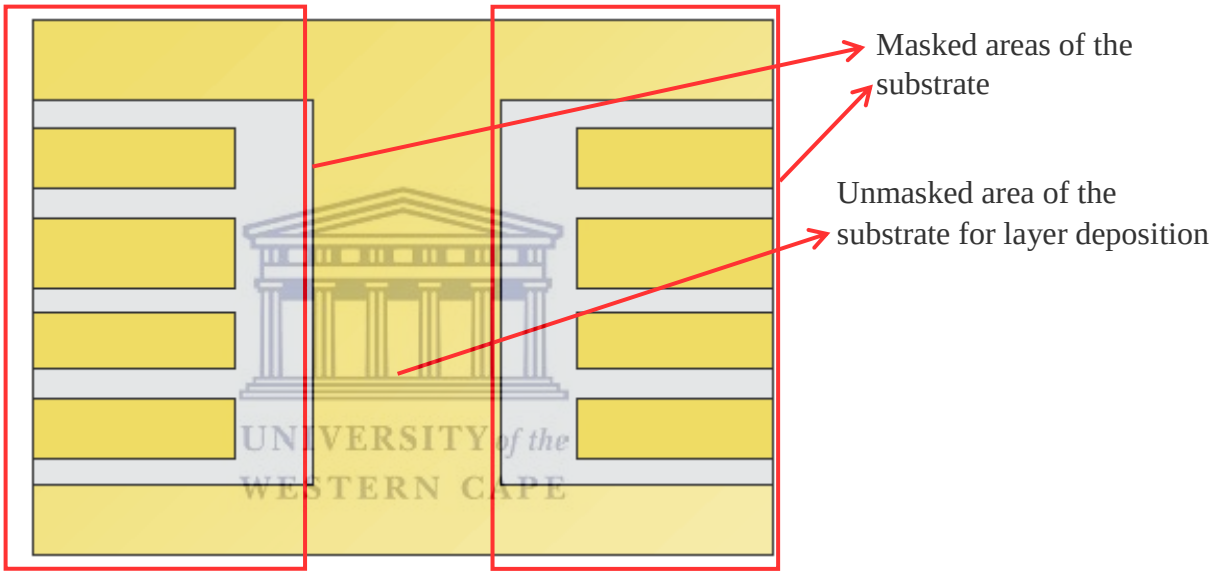

Figure 3.3: Schematic of the ITO substrates showing the areas that were masked before spin coating.

3.2.2.1 Compact pristine TiO_2 and Ag-TiO_2

3.2.2.1.1 Pristine TiO_2

3.2.2.1.1.1 Solution processing

The pristine compact-TiO_2 precursor solution was synthesized by dripping 1 mL titanium diisopropoxide into 19 mL ethanol, then the mixture was stirred for 1 hour at room temperature.

3.2.2.1.1.2 Spin coating procedure and parameters

The c-TiO_2 layer was prepared by spin-coating 60 µL of TiO_2 precursor solution at 4000 rpm for 20 s on the ITO substrate. The film was then annealed at 150 °C for 10 min on a hot plate, and finally underwent heat- treatment at 500 °C for 30 min in a furnace.

3.2.2.1.2 Ag doped-TiO_2

3.2.2.1.2.1 Solution processing

Three Ag-doped TiO_2 precursor solutions were prepared in order to evaluate the overall effect of the percentage doping of silver on the device efficiency. Firstly, chosen amounts of silver nitrate (0.0017, 0.005, and 0.008 g) were added to 1 mL titanium diisopropoxide in various molar ratios (Ag : Ti = 0.5, 1.5 and 2.5 %). Secondly, the acquired solutions were added to 19 mL of ethanol. The three mixtures were stirred for 1 hour at room temperature to form the uniform compact precursor solutions.

3.2.2.1.2.2 Spin coating procedure and parameters

The three different Ag-TiO_2 layers were each prepared on separate substrates by spin-coating 60 µL of Ag-TiO_2 precursor solution at 4000 rpm for 20 s on the ITO substrate. The film was then annealed at 150 °C for 10 min on a hot plate, and finally underwent heat- treatment at 500 °C for 30 min.

3.2.2.2 Mesoporous-TiO_2

3.2.2.2.1 Solution processing

TiO_2 nanoparticles were diluted in ethanol with 1:7 weight ratios.

3.2.2.2.2 Spin coating procedure and parameters

The mesoporous-TiO_2 layer was prepared by spin-coating 60 µL of TiO_2 precursor solution at 5000 rpm for 45 s on the ITO/c-TiO_2 or Ag-TiO_2 substrates. The film was then annealed at 150 °C for 10 min on a hot plate, and finally underwent heat- treatment at 500 °C for 30 min to obtain the anatase phase of TiO_2.

3.2.2.3 Perovskite ($CH_3NH_3PbI_3$)

3.2.2.3.1 Solution processing

To prepare the perovskite absorbing layer the two precursor solutions were each initially synthesized separately then combined during the deposition process. The first precursor solution synthesized was PbI_2. 461 mg of PbI_2 was dissolved in a 1 ml mixture of Terephtalic acid (TPA, 8mg/mL) and dimethylformamide (DMF). The mixture was then stirred overnight at 70^oC overnight. The second precursor solution was MAI/2-Propanol (0.42M) solution. This solution was used as purchased no modification were done to it.

3.2.2.3.2 Spin coating procedure and parameters

The active layer was deposited via two steps. The first step involved the preheating of both the PbI_2 precursor solution and the ITO/c-TiO_2 or Ag-TiO_2/p-TiO_2 substrates at 70 ^oC. Subsequently, 60 µl of PbI_2 solution was dropped onto the ITO/c-TiO_2 or Ag-TiO_2/p-TiO_2 substrates, then spinne6d at 3000 rpm for 30 s. The as-coated films were then annealed at 100 ^oC for 1 hour.

The second step involved dropping 60 µl of MAI/2-Propanol solution onto the ITO/c-TiO_2 or Ag-TiO_2/p-TiO_2/PbI_2 substrates. A pause of 40 s was observed before starting the spinning to allow for the MAI MAI/2-Propanol solution to properly penetrate the PbI_2 layer. Subsequently

the substrates were spin-coated at 2000 rpm for 30 s. The as-coated perovskite films were then annealed at 70 ^{o}C for 20 min.

3.2.2.4 Spiro-OMeTAD

3.2.2.4.1 Solution processing

The precursor solution was prepared by mixing 73 mg of spiro-OMeTAD into 1ml of chlorobenzene with additives consisting of 17.5 mL LiTFSI/acetonitrile (520 mg/mL) and 28.8 mL of 4-tert-butylpyridine.

3.2.2.4.2 Spin coating procedure and parameters

The HTM layer prepared spin-coating 60 μL of the spiro-OMeTAD solution onto the FTO/c-TiO_2/p-TiO_2/$MAPbI_3$ substrate at 2000 rpm for 45 s.

3.2.2.5 Evaporation of Silver electrode

The samples were allowed to dry in open air for a few minutes then put in a masked holder for the substrates to only get the evaporated metal on the wanted area that was at the center of the substrate as previously displayed in **Figure 3.3** and then placed in the evaporator (Leybold vacuum, Univex 350). The metal evaporated metal was Silver (Ag). The evaporation began by lowering the amount of pressure pressure inside the evaporator and when the pressure reached vacuum of < 3.5×10^{-6} mbar the current within the holder was manually increased. At ~165 A the evaporation of the silver started and the voltage was changed to get an evaporation speed of 0.02 nm. s^{-1} until a layer of thickness of 10 nm had been evaporated. The reason for the slow evaporation speed at the start was to avoid the Ag particles from penetrating the spiro-OMeTAD and be in direct contact with the perovskite layer. Then the evaporation speed was increased to 0.2 nm. s^{-1} by changing the current. One pellet of Ag resulted in a layer approximately 70 nm thick.

3.3 Characterization of interfaces and devices

3.3.1 Film characterization techniques

3.3.1.1 Surface profilorimery

Veeco Dektak profilometers was used for the measurement of layer thicknesses. Samples were scratched with a scalpel and then cleaned with compressed nitrogen in order to remove any remaining debris. The stylus of the Dektak was then passed above the sample, going across the scratch in the film, permitting a thickness measurement to be taken as shown in **Figure 3.** 4 **(a)**. At least 4 readings from different scratches were taken for each sample individually and the average of those thicknesses was used. In the case of uneven films the height was averaged over a range of positions in order to guarantee a more accurate reading (see **Figure 3.** 4 **(b)**).

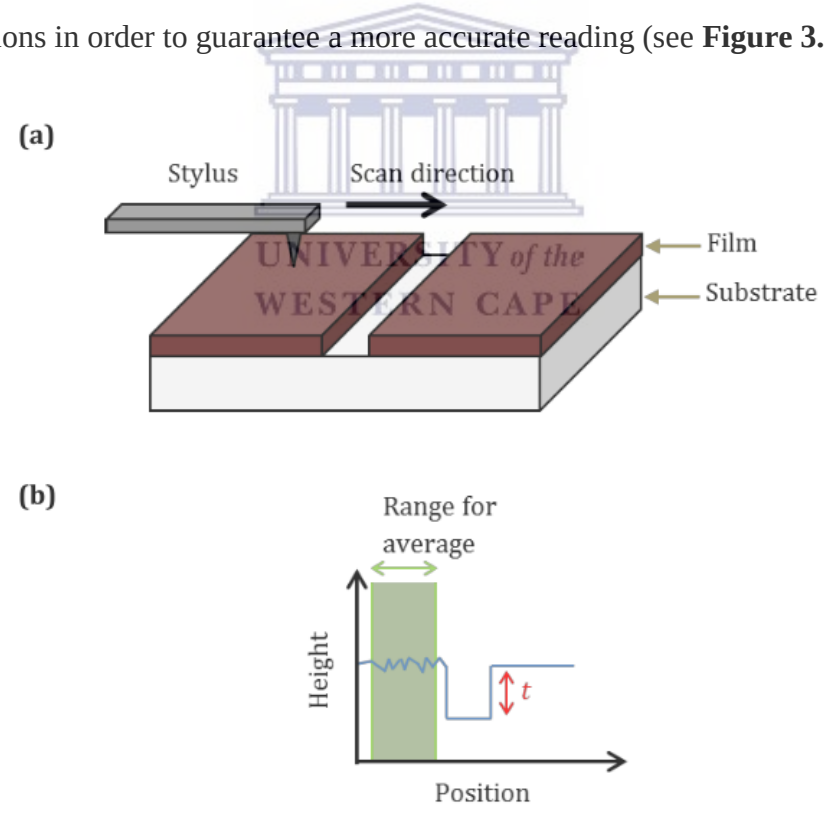

Figure 3. 4: A schematic of the profilometry equipment (a) and an example scan showing the use of a range in order to ensure a more accurate height reading when measuring rough films (b).

3.3.1.2 Microscopic characterization

Microscopy is a specialized field of characterization techniques that uses microscopes to inspect objects and the surface of objects that would normally be difficult to see with the naked eye (objects that are not within the resolution range of the normal eye) [1]. There are three types of microscopy: optical, electron, and scanning probe microscopy. **Figure 3.5** shows cross sectional diagram of imaging modes for the three types of microscopes regularly employed for materials characterization: the light microscope (left), the transmission electron microscope (TEM, center), and the scanning electron microscope (SEM, right).

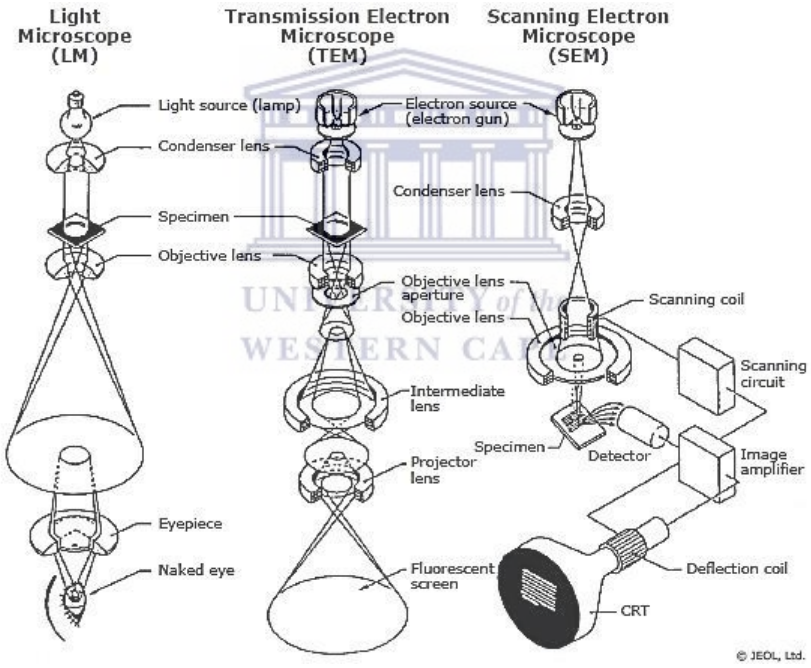

Figure 3.5: Schematic cross-sections of imaging modes in the light microscope, the TEM, and the SEM [2].

Frequent elements include a source of illumination (visible light source or an electron gun) and a condenser lens over the specimen to center the light or electron beam. After the condenser lens, the structure of the SEM diverges from that of the light microscope and the TEM. In the latter two, the objective lens that produce the image is positioned below the specimen, and a static,

near-parallel beam of illumination is projected onto a viewing point or onto a camera for recording. Though the TEM includes some additional lenses, the overall method by which the image is obtained and projected for viewing and recording is the same as that of the light microscope.

The SEM is significantly different in that the objective lens sits over the specimen or sample, and the beam is created into a fine, centered probe that is passed across the specimen using scanning coils, producing an image point by point. The image can be recorded on various detectors placed above the specimen.

These types of microscopes give complementary information over diverse size ranges. The unaided human eye resolution features down to about 100 μm in size, and the best performing light microscopes allow us to see features as small as 1 μm. Because SEMs and TEMs utilize electrons, which have higher energies and shorter wavelengths than visible light, much smaller objects can be seen as well from its use. The highest-resolution SEMs can allow users to see objects with only a few nanometers in size, while aberration-corrected TEMs allow for imaging and analysis of objects and substance at the atomic level. All three types of microscope can be used complementarily to provide fundamental information about size, morphology, and texture of materials or objects. Although the SEM and TEM are usually classified as electron optical instruments, the TEM and the light microscope share a similar mechanism for image formation.

3.3.1.2.1 Scanning Electron Microscopy (SEM)

Scanning electron microscopy (SEM) is a characterization technique that utilizes electrons to investigate a sample's surface in order to imaging easier at higher resolution than is possible with the normal optical microscope. Given that the resolution is only limited to around half the wavelength of the probe, it is possible to obtain much higher resolution with electron microscopy

than optical microscopy. Additionally, SEMs offer the ability to obtain better '3D' image than optical microscopes due to the larger depth of focus resulting from the lower aperture angle.

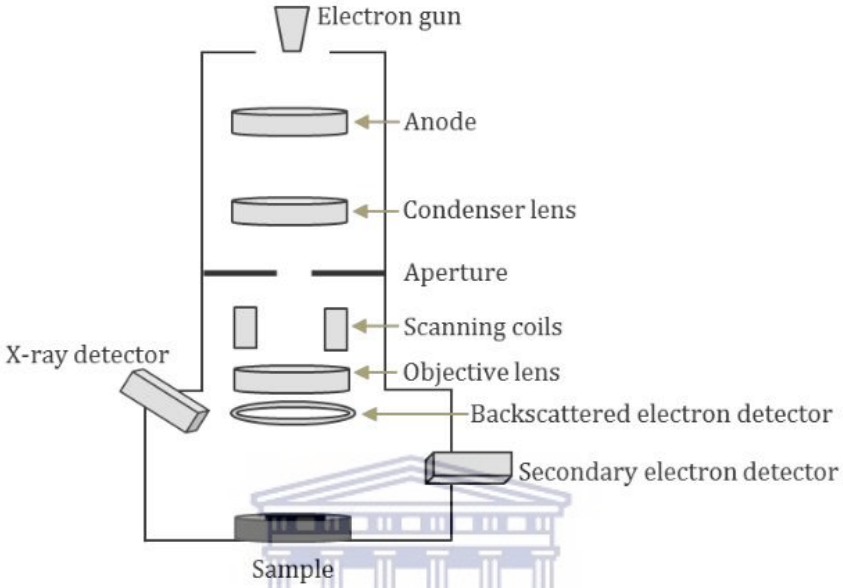

Figure 3.6: A basic schematic of a scanning electron microscope.

In **Figure 3.6** is shown a simplified image/schematic diagram of the SEM instrument. In order to avoid interactions between the electron beam and the air, the electron gun, optics and sample chamber are held under vacuum, which reduces the image quality and could cause the sample to be damaged. The electron beam in a SEM is generated by either a thermionic emission gun (heating a filament to release electrons) or field emission gun (using a strong electric field to extract electrons from a tungsten crystal). A field emission gun SEM (FEGSEM or FESEM) offers better resolution than its thermionic counterpart due to the production of narrower beams of electrons with smaller spread in energy. In this work the field emission gun SEMs has been used. Electrons are emmited and allowed to travel in a helical path down the microscope column under the influence of magnetic fields from the electromagnetic lenses. To control the spot size

of the beam on the sample, the condenser lens(es) and aperture(s) act in tandem. A decreased spot size increases the resolution but reduce the clarity of the image and results in ‘graininess’ as less electrons invade on the sample. Scanning coils are used to deploy the electron beam across the sample in order to produce an image, whilst electron beam is focused onto the sample by the objective lens. Increasing the accelerating voltage reduces the diameter of electron probe, therefore the improving resolution of the output images obtained from the sample analysis. This also, however, reduces the clarity of surface structures, because the penetration of the beam into the sample is augmented. In addition the charging is increased together with any sample damage which may occur. When the electron beam strikes the sample it causes both electrons and X-rays to be ejected from the material. The ejected electrons are usually distributed into two types – secondary and backscattered, with imaging most of the time achieved using the secondary electrons (SEs). These have a shallow generation region (~10 nm) since those generated deeper in the sample will be unable to escape due to their fairly low energy (~50 eV or less). Secondary electron detectors have a scintillator (fluorescent material) over which a voltage is applied. In front of the detector is also a collector, through which a high voltage is applied to attract the secondary electrons discharged from the sample. These impact on the scintillator and generate light which is allowed to pass through a photomultiplier before being transformed into an electrical signal. When the electron beam attains the sample at an angle, more secondary electrons are generated than when it is normal to the surface, implying that SE images appear particularly topographical. Backscattered electrons have a higher energy than secondary electrons, having a range of energies up to that of the incident beam. The increased energy of the backscattered electrons implies that they are less impacted by charging and specimen contamination than SEs, and that their generation region is considerably larger. While this

decreases resolution, it does allow for detection of electrons from deeper into the sample. Backscattered electron intensity is dependent on atomic number, and thus backscattered images can provide a composition contrast as well as a topographic one.

It is important to note that the sample under examination is conductive enough, or coated and stuck to the sample stub with a conductive material to avoid charging. This happens when electrons from the probe beam build up on the specimen, interfering with secondary electron emission and thus adversely affecting the image quality and resolution.

For the purpose of this research project the instrument used for this specific analysis was the ZEISS ULTRA scanning electron microscope with acceleration voltage of 5.0 kV.

3.3.1.2.2 Transmission electron microscope

Transmission electron microscopy (TEM) is a microscopy technique in which a beam of electrons is transmitted across an ultrathin sample or specimen, interacting with the sample as it passes through. An image is produced from the interaction of the electrons transmitted through the sample; the image is enlarged and focused onto an imaging device, such as a fluorescent screen, on a layer of photographic film, or to be detected by a sensor such as a CCD camera.

TEM in essence is used to reveal sub-micrometer, internal fine structure in solids. The amount of information which can be extracted by TEM depends critically on four very important parameters; the resolving power of the microscope (usually smaller than 0.3 nm); the energy spread of the electron beam (often several eV); the thickness of the specimen (almost always significantly less than 1μm), and; the composition and stability of the specimen [3].

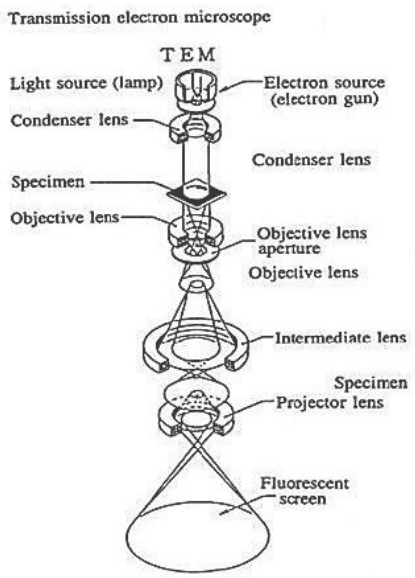

Figure 3.7: General layout of a TEM describing the path of electron beam in a TEM. (Image taken from JEOL 2000FX Handbook).

In order to obtain the TEM images needed for a sample, the beam of electrons from the electron gun is focused into a small, thin, clear beam by the use of the condenser lens as shown in **Figure 3.7**. The beam is limited by the condenser aperture, which eliminates high angle electrons. The beam then collides with the sample and parts of it are diffused depending upon the thickness and electron translucence of the specimen. This transmitted portion is focused by the objective lens into an image on phosphor screen or charge coupled device (CCD) camera. Optional objective apertures can be utilized to increase the contrast by blocking out high-angle diffracted electrons. The image is then passed down the column across the intermediate and projector lenses, is broadened all the way. The image strikes the phosphor screen and light is produced, allowing the user to see the image. The darker areas of the image characterize those areas of the sample that fewer electrons are transmitted across while the brighter areas of the image characterize those areas of the sample that more electrons were transmitted across.

For the purpose of this research project the TEM instrument used for this analysis is the TECNAI G2 F2O X-TWIN MAT 200 kV field emission, where nickel grid was used to coat the material for better conductivity.

3.3.1.3 Spectroscopic characterization

Spectroscopy is the study of the properties of matter and its interaction with different frequency components of the electromagnetic spectrum [4]. Spectroscopy is a common technique that can be used in many ways to obtain information needed about a substance such as electronic energies, vibrational energies, rotational states, structure and symmetry of molecules, and finally dynamic information.

3.3.1.3.1 Energy-Dispersive X-ray spectroscopy (EDS or EDX)

Energy dispersive X-ray spectroscopy (EDS) is a typical technique for element detection in material analysis. EDS systems are mounted on scanning electron microscopes (SEM) and use the primary beam of the microscope to produce characteristic X-rays. The composition of the sample is found by analyzing the energy of the characteristic X-rays that are emitted from the sample after the incoming radiation [5]. The spatial (lateral + vertical) resolution of EDS depends on the sample material and the energy of the primary beam of the SEM as shown in **Figure 3.8**.

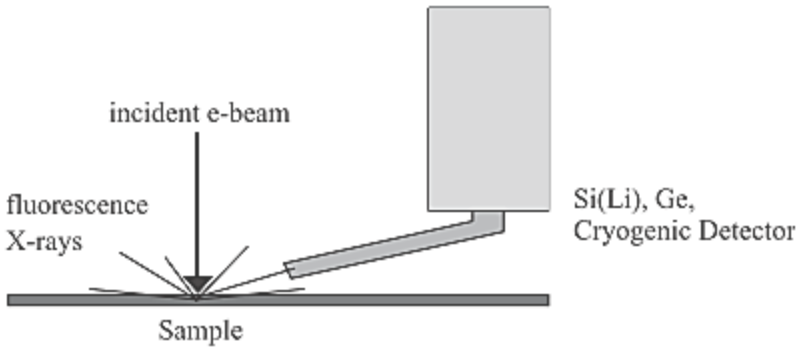

Figure 3.8: Working principle of EDS.

The instrument used is the EDS analyzer coupled into the High-Resolution Scanning Electron Microscope used for SEM analysis.

3.3.1.3.2 Ultraviolet-Visible spectroscopy (UV-Vis)

UV/Vis spectroscopy is a measurement technique in which the recording of the absorption spectra of different samples using ultraviolet (UV) and visible (Vis) light is achieved by a spectrophotometer, i.e. an instrument able to measure the spectrum of a sample in the UV/Vis range [6]. A UV/Vis spectrophotometer determines the intensity of light passing through a sample solution in a cuvette, and evaluates it against the intensity of the light before it passes through the sample. The light should also be passed though the cuvette or sample holder in order to account for any absorption by them. The major components of a UV/Vis spectrophotometer are a light source, a sample holder, a dispersive device to separate the different wavelengths of the light (e.g. a monochromator), and a suitable detector as shown in **Figure 3.9**.

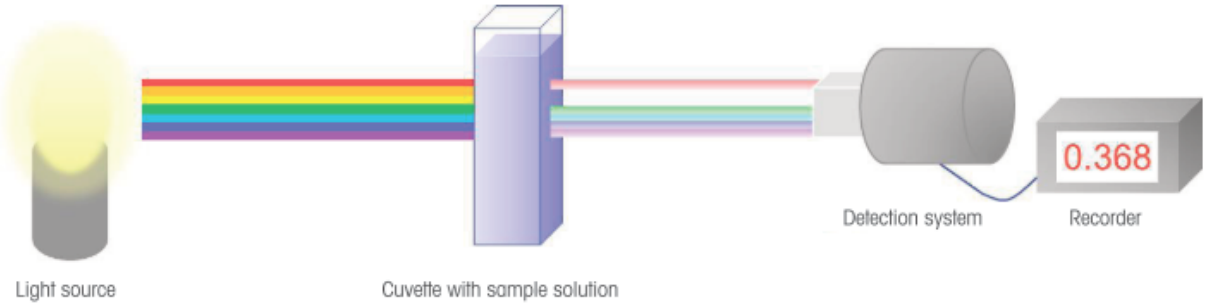

Figure 3.9: Measurement principle in UV/VIS spectroscopy [6].

The UV–Vis absorption spectra were obtained by using UV-Vis Double beam Spectrophotometer from ThermoFisher Scientific.

3.3.1.4 Electrochemical characterization

Electrochemistry is a vast and interdisciplinary field of research and development activity, that deals the interrelation of electrical and chemical effects [7]. A significant aspect of this field is the study of chemical changes caused by the movement of an electric current and the generation of electrical energy by chemical reactions, which include an array of diverse phenomena (e.g., electrophoresis and corrosion), devices (electrochromic displays, electroanalytical sensors, etc.), and technologies (the electroplating of metals and the large-scale production of aluminum and chlorine) [8].

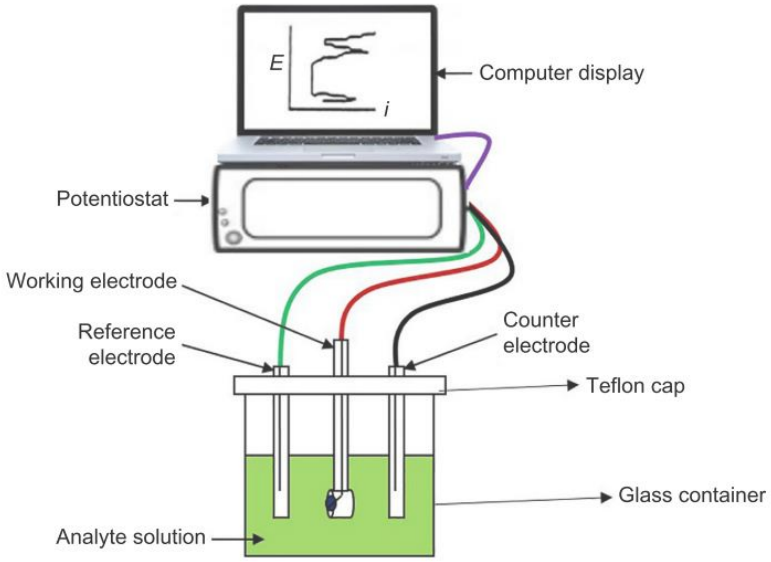

Figure 3.10:Illustration depicting the simplicity of a three-electrode electrochemical cell system that would form part of an electrochemical workstation.

Although largely based on conventional electrochemical characterization methods developed for bulk materials, including potentiometric, polarography, voltammetry, cyclic voltammetry (CV), chrono-potentiometry, chrono-amperometry, linear sweep, and pulsed methods, the "nanoscale" concept has initiated a new scenario in which physicochemical principles, laws, and properties which can be quite different from those of the macro and micro worlds. Electrochemical characterization of nanomaterials necessitates not only sensitivity and selectivity but also accuracy.

Deciding on the best technique for a particular situation needs knowledge of the analyzed particles or materials, the ultimate application of the particles, and the restrictions of the considered techniques. Therefore, a rational choice of technique(s) and methodology(ies) is essential.

The basis of electrochemical investigation is electrode surface reaction. Because the working electrode (WE) substrates can strongly influence the efficiency of the reactions, the properties of electrode substrates and ionic substance at the electrode surface are of great significance for successful electrochemical characterization. Different researchers, including David Harvey et al. in 2012, have shown that there are six basic and interrelated concepts of note in the study of electrochemistry: (1) the electrode's potential determines the analyte's form at the electrode's surface; (2) the electrochemical cell design; (3) the concentration of analyte at the electrode's surface may not be the same as its concentration in bulk solution; (4) the analyte may not be restricted from participating in other reactions; (5) the current as a measure of the rate of the analyte's oxidation or reduction; and (6) current and potential cannot be controlled simultaneously.

3.3.1.4 Electrochemical Characterization

3.3.1.4.1 Cyclic Voltammetry

CV is a technique used to study the electrochemical properties associated with surfaces that are electroactive. CV is a very multipurpose electrochemical method that enables understanding of the mechanisms of redox reactions, reversibility of a reaction, and electron transfer kinetics of an electroactive species in solution [9,10]. CV offers rapid information on thermodynamic redox processes, on the kinetics of heterogeneous electron-transfer reactions, and on coupled chemical reactions or adsorption processes [9]. It is the foremost electrochemical experiment performed to characterize electrode material for every type of application [9].

3.3.2 Device characterization

3.3.2.1 Solar Cells Current-Voltage measurements

The main characteristic of a solar cell is its aptitude to convert light into electricity. This is known as the power conversion efficiency (PCE) and is the ratio of incident light power to output electrical power. To determine the PCE, and other helpful metrics, current density-voltage (I-V) measurements are performed. A series of voltages are applied to the solar cell while it is under illumination. The output current is quantified at each voltage step, resulting in the characteristic 'I-V curve' seen in many research papers. An example of this can be seen below in **Figure 3.11**, along with some significant properties that can be determined from the I-V measurement. It should be noted that generally, current density (J) is used instead of current when characterizing solar cells, as the area of the cell will have an effect on the magnitude of the output current (the larger the cell, the more current).

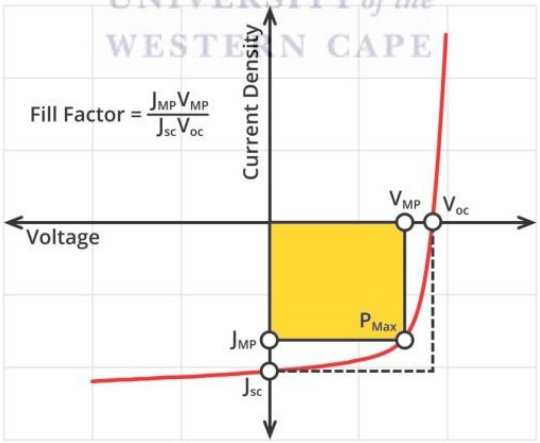

Figure 3.11: Typical I-V curve of a solar cell plotted using current density, highlighting the short-circuit current density (J_{sc}), open-circuit voltage (V_{oc}), current and voltage at maximum power (J_{MP} and V_{MP} respectively), maximum power point (P_{Max}), and fill factor.

3.3.3. Other characterization

3.3.3.1 X-ray diffractometry (XRD)

X-ray diffraction (XRD) is one of the most important non-destructive tools to analyze diverse classes of matter, ranging from fluids, to powders and crystals. From research to production and engineering, XRD is a crucial method for structural materials characterization and quality control which makes use of the Debye-Scherrer method. This technique uses X-ray (or neutron) diffraction on powder or microcrystalline samples, where preferably every possible crystalline orientation is characterized equally. In the so called diffractogram the diffracted intensity is shown as function either of the scattering angle 2θ or as a function of the scattering vector q which makes it autonomous from the used X-ray wavelength. The diffractogram is like a distinctive "fingerprint" of materials.

X-ray diffractometry is a characterization technique that bases its working principle solely onit ability to diffracts X-rays from crystals in a characteristic manner allowing a precise study of the structure of crystalline phases. The recorded diffraction patterns contain additive contributions of several micro- and macro-structural characteristics of a sample. With the peak position, lattice parameters, space group, chemical composition, macro-stresses, or qualitative phase analysis can be examined. Based on the peak intensity, knowledge about crystal structure (atomic positions, temperature factor, or occupancy) as well as texture and quantitative phase analyses can be obtained. Finally, the peak shape gives information about sample broadening contributions (micro-strains and crystallite size) [11].

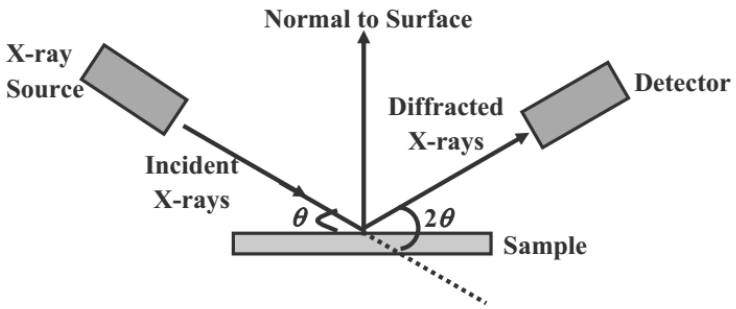

Figure 3.12: Schematic representation of the working principle of X-ray diffraction [11].

The SAED micrograph as seen from the example in **Figure 4.4** is the diffraction pattern obtained in the reverse space of the lattice planes. It is used in order to find the d-spacing of the crystal planes. The SAED pattern can be used to see if the sample is amorphous, i.e. diffuse rings, crystalline (bright spots), polycrystalline (small spots making up rings, each spot arising from Bragg reflection from an individual crystallite. The results obtained from XRD can be used in conjunction with the SAED micrograph to corroborate specific information obtained from the sample.

The XRD data were collected with the help of the BRUKER AXS DS Advance diffractometer with 2θ values ranging from 20-90 º, with a step size of 0.028 º operating at 45 kV and 40mA form the Ithemba Labs.

3.3.3.2 Fourier Transform Infrared Spectroscopy (FTIR)

FTIR analysis measures the intensity of absorption at a range of wavelengths in the infrared region that are captured by a material as seen. The application of infrared radiation (IR) to samples of a material allows for this to be accomplished. The sample's absorbance of the infrared light's energy at diverse wavelengths is measured to determine the material's molecular composition and structure [12].

This technique also allow for the identification of unknown materials by comparing the spectrum against a spectra in the reference database. Materials can be quantified using the FTIR materials characterization technique as long as a standard curve of known concentrations of the component of interest can be created.

FTIR analysis can be used to identify new materials, additives within polymers, surface contamination on a material, and more. The results of the tests can identify a sample's molecular composition and structure.

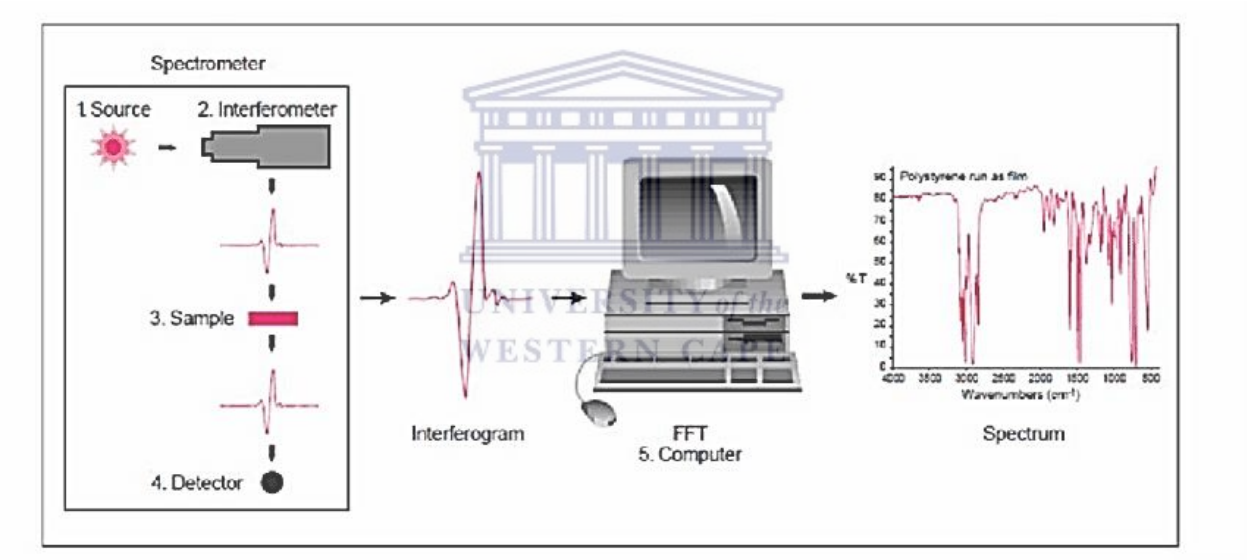

Figure 3.13: Working principle of the Fourier transform infra-red spectrometer Infra-red (IR) spectrometer [14].

The instrument used for the analysis was Perkin Elmer spectrum Two FTIR spectrometer. FTIR Spectra were recorded in the range of 4000-400 cm^{-1} using the substrates coated with the different layers of materials being studied.

3.4 References

[1] The University of Edinburgh, What is Microscopy? | The University of Edinburgh, Online. (n.d.). https://www.ed.ac.uk/clinical-sciences/edinburgh-imaging/for-patients-study-participants/tell-me-more-about-my-scan/what-is-microscopy (accessed November 28, 2019).

[2] E.F. Schumacher, Microscopy for materials characterization: Illuminating structures with light and electrons, Am. Lab. 46 (2014). https://www.americanlaboratory.com/914-Application-Notes/167499-Microscopy-for-Materials-Characterization-Illuminating-Structures-With-Light-and-Electrons/ (accessed November 28, 2019).

[3] P.J. Goodhew, General Introduction to Transmission Electron Microscopy (TEM), in: Aberration-Corrected Anal. Transm. Electron Microsc., 2018: pp. 1–18. doi:10.1002/9781119978848.ch1.

[4] J. Chen, B. Gu, E.J. Leboeuf, H. Pan, S. Dai, Spectroscopic characterization of the structural and functional properties of natural organic matter fractions, Chemosphere. 48 (2002) 59–68.

[5] C. Hollerith, D. Wernicke, M. Buhler, F. v. Feilitzsch, M. Huber, J. H.ohne, T. Hertrich, J. Jochum, K. Phelan, M. Stark, B. Simmnacher, W. Weiland, W. Westphal, Energy dispersive X-ray spectroscopy with microcalorimeters, Nucl. Instruments Methods Phys. Res. 520 (2004) 606–609. doi:10.1016/j.nima.2003.11.327.

[6] C.A. De Caro, UV / VIS Spectrophotometry Fundamentals and Aplications, 2015.

[7] P.S. Nnamchi, C.S. Obayi, Electrochemical Characterization of Nanomaterials, in: Charact. Nanomater., Elsevier Ltd., 2018: pp. 103–127. doi:10.1016/b978-0-08-101973-

3.00004-3.

[8] A. Larry, J. Bard, Faulkner, L. R., Electrochemical Methods: Fundamentals and Applications, second edi, JOHN WILEY & SONS, INC, 2001. doi:10.1108/acmm.2003.12850eae.001.

[9] F. Manea, Electrochemical Techniques for Characterization and Detection Application of Nanostructured Carbon Composite, in: Mod. Electrochem. Methods Nano, Surf. Corros. Sci., InTech, 2014. doi:10.5772/58633.

[10] D.K. Gosser, Cyclic Voltammetry; Simulation and Analysis of Reaction Mechanisms, Synth. React. Inorg. Met. Chem. 24 (1994) 1237–1238. doi:10.1080/00945719408001398.

[11] Y. Li, S.M. Chen, M.A. Ali, F.M.A. AlHemaid, Biosynthesis and electrochemical characterization of silver nanoparticles from leaf extract of adenium obesum and its application to antibacterial effect, Int. J. Electrochem. Sci. 8 (2013) 2691–2701.

[12] R.E. Dinnebier, S.J.L. Billinge, Powder Diffraction : Theory and Practice, Royal Society of Chemistry, 2008. doi:10.1039/9781847558237.

[13] J. Mathias, How Does FTIR Work? | Innovatech Labs, (2015). https://www.innovatechlabs.com/newsroom/672/stuff-works-ftir-analysis/ (accessed November 29, 2019).

[14] G. Ramaiah, D. Bhatia, Structural Analysis Of Merino Wool, Pashmina And Angora Fibers Using Analytical Instruments Like Scanning Electron Microscope And Infra-Red Spectroscopy, Int. J. Eng. Technol. Sci. Res. 2394-3386. 4 (2017) 112–125. https://www.researchgate.net/publication/319135784_Structural_Analysis_Of_Merino_W

ool_Pashmina_And_Angora_Fibers_Using_Analytical_Instruments_Like_Scanning_Electron_Microscope_And_Infra-Red_Spectroscopy (accessed March 1, 2020).

Chapter 4 Results and Discussions

This chapter introduces the results gotten from the different characterization techniques performed, their analysis and discussion. The techniques used comprised HR-SEM, HR-TEM, XRD, EDS, FTIR, UV-Vis, CV and I-V curve measurements. The most important deductions and conclusionsare based on calculated photovoltaic parameters. The majority of the samples were fabricated in air with relative humidity of about 60 %. Because of the moisture in air and other atmospheric effects, the perovskite fabrication is not totally reproducible and the degree of degradation varies. Thus, the photovoltaic parameters of the prepared solar cell series are not fully comparable to each other.

4.1 Interface characterization

4.1.1 Surface morphology

High Resolution Scanning Electron Microscope (HR-SEM)

The morphology of the surface of the prepared pristine TiO_2 and Ag-TiO_2 thin films were studied using a scanning electron microscope.

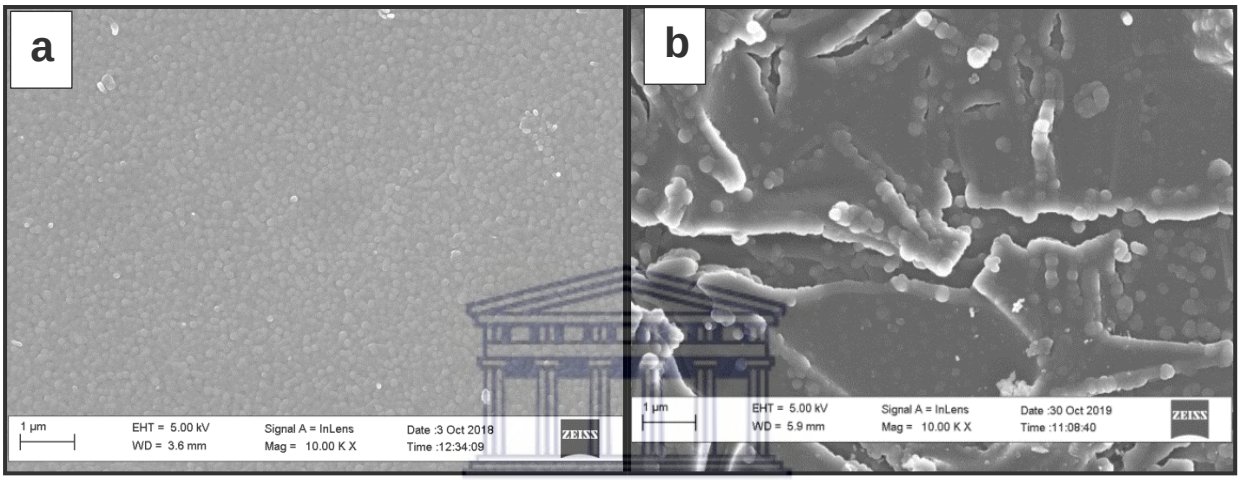

Figure 4.1: SEM images of a) Pristine compact-TiO_2 and b) 2.5 % Ag-TiO_2 composite films.

Figure 4.1 a) and b) shows the SEM images of the undoped (compact pristine TiO_2 layer) and Ag doped TiO_2 films formed on the ITO substrates via the spin-coating method. The images of the pure TiO_2 film in **Figure 4.1** shows the surface morphologies of compact TiO_2 layers which was fabricated on ITO substrates using spin-coating methods. As can be seen in **Figure 4.1 a)** the TiO_2 is extremely smooth and dense with very good surface coverage, showing no observable defects. The surface doesn't show any discontinuities, cracks, pinholes, and pores. As is well-known, ITO substrates are based on In-doped SnO_2 grains with sizes fluctuating between tens to hundreds of nanometers, and due to the grain boundaries, the substrate surface is uneven. The spin- coating-based compact TiO_2 layer did not alter the surface topography of the ITO grains as the layer was very thin (45-60 nm thick across the surface of the substrate). Relatively

large TiO_2 particles (>10 nm) fill up the gaps between the ITO grains and makes the surface much smoother on the micron scale. This means that, the TiO_2 layer's thickness the is not perfectly uniform across the surface of the substrate, and this theoretically should be problematic in when it comes to the charge collection through the blocking layer. These affirmations will further be confirmed by the cyclic voltammetry study which was done to both test for defects in the TiO_2 compact blocking layer and test for the ability of the material to reduce recombination.

The microstructure of the Ag-TiO_2 films was made up of several mud-crack shaped layers. These defects could be due to the heat treatment regime to which the Ag-TiO_2 films were exposed. Thermal shock may be the principal reason for the mud cracks on the surface of the films. These cracks on the layer surface are very noticeable when the Ag concentration was augmented as was the case in **Figure 4.1 b)** above; the larger Ag particles were observed on the mud-crack-shaped layers. Even with these apparent defects at the surface of the layer the Ag nanoparticles helped in increasing the conductivity of the TiO_2 layer as will once again be observed in the results of the cyclic voltammetry study explained later in this chapter.

4.1.2 Internal structure

1.1.1.1 High Resolution Transmission Electron Microscope (HR-TEM)

The internal structure of the synthesized nanoparticles was evaluated using transmission electron microscope (TEM).

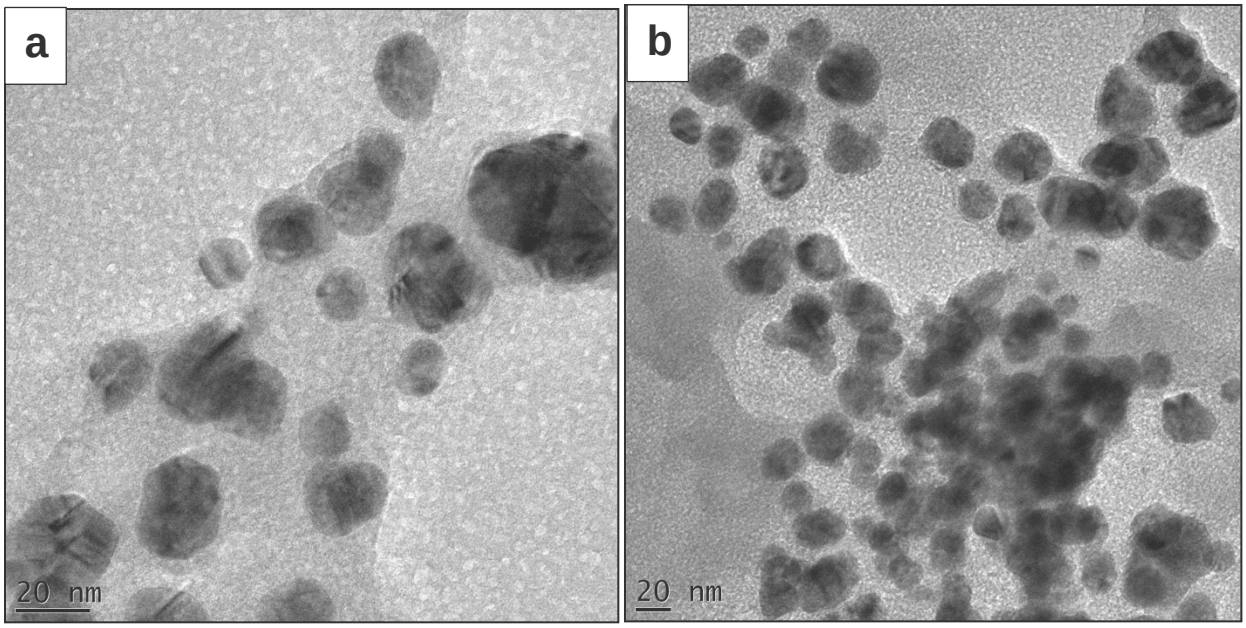

Figure 4.2:TEM micrograph of a) Pristine compact-TiO_2 and b) 2.5 % Ag-TiO_2 solutions.

The TEM images of the pristine compact-TiO_2 and 2.5 % Ag-doped TiO_2 particles are shown in **Figure 4.2 a)** and **b)** respectively. The micrograph obtained for the nanoparticles shows the poly-disperse nature of the nanoparticles in both cases. The micrograph shows some sphere-like structure for both the pristine TiO_2 and Ag-TiO_2 as can be seen in **Figure 4.2 a)** and **b)** above. The internal structure of the synthesized nanoparticles also revealed some agglomerations as well as the presence of nanoparticles of smaller sizes. Although the observed TiO_2 nanoparticles have a spherical shape with a diameter of about 25 nm, most of the TiO_2 nanoparticles appeared to be agglomerated and formed large particle with a diameter as large as 50 nm, which might be due to their large surface area and high interface energy. Compared with TiO_2 nanoparticles, Ag-TiO_2 nanoparticles showed much more agglomeration with a diameter around 30 nm for the smaller nanoparticles and up to about 90 nanometers for the larger nanoparticles as depicted in **Figure 4.2 b)**. Although, the micrograph obtained did show sporadic agglomeration of nanoparticles in some areas for both the pristine and Ag-doped nanoparticles, distinct information about the

internal structure could still be extracted to determine the particle size of the nanoparticles and lattice fringes spacing as will be seen later.

4.1.3 Phase composition

1.1.1.2 X-Ray Diffraction (XRD)

The phase composition and crystalline structure of the synthesized nanoparticles were investigated through powder X-ray diffraction (XRD). The XRD results obtained were refined with crystal-impact software called MATCH to remove the noise and obtain only the available peaks from the diffraction pattern of the sample analyzed.

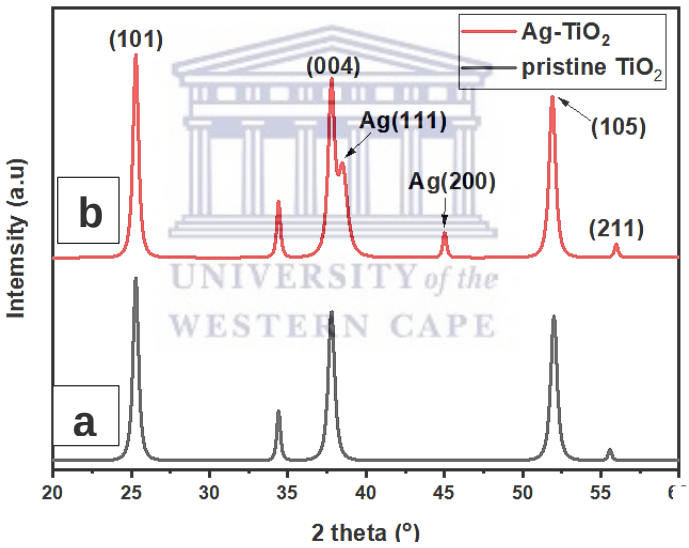

Figure 4.3: XRD patterns of the a) pristine TiO_2 and b) 2.5 % Ag-TiO_2 composites films with substracted ITO substrates peaks.

The XRD patterns of the pristine TiO_2 and the Ag/nano-TiO_2 composite compact film are presented in **Figure 4.3 a) and b)**. The spiky and intense peaks in spectra are an sign of the presence of crystalline films. Most of the main diffraction peaks at 25.29 ^{o} (101), 37.69 ^{o} (004), 51.97 ^{o} (105) and 54.91 ^{o} (211) agree with the JCPDS values (PDF Card No: 00-021-1272) which match to the crystal structure of anatase phase of TiO_2 [1]. As opposed to the diffraction

peaks of the pristine TiO_2, the peaks of the Ag-TiO_2 composite compact film in ($2\theta = 38^o$) and ($2\theta = 45^o$) are considerably larger, while the other peaks stay almost the same as in the pristine which was expected as seen in **Figure 4.3 b)**. One very important aspect to note is the fact that the peaks of the Ag-TiO_2 composite compact film in ($2\theta = 38^o$) and ($2\theta = 45^o$) are not observed at all in the pristine compact-TiO_2 films. The peaks at diffraction angles ($2\theta = 38^o$) and ($2\theta = 45^o$) are attributed to the specific diffraction peaks of the (111) and (200) crystal planes of Ag with the standard anatase PDF card, respectively. Additionally, there is no clear shift in any of the diffraction peaks, suggesting that no trace of the Ag oxide phase was found in the prepared samples. It is possible to observe that all the distinctive diffraction peaks of the anatase TiO_2 phase (101), (004), and (105) are seen in **Figure 4.3 a)** and **b).** The full-width at half-maximum is similar for the most intense peak of the anatase diffraction phase (101)of both the pristine TiO_2 compact film and the Ag-TiO_2 composite compact film. This is an indication that the crystal structure of TiO_2 barely changes with the development of the Ag-TiO_2 composites.

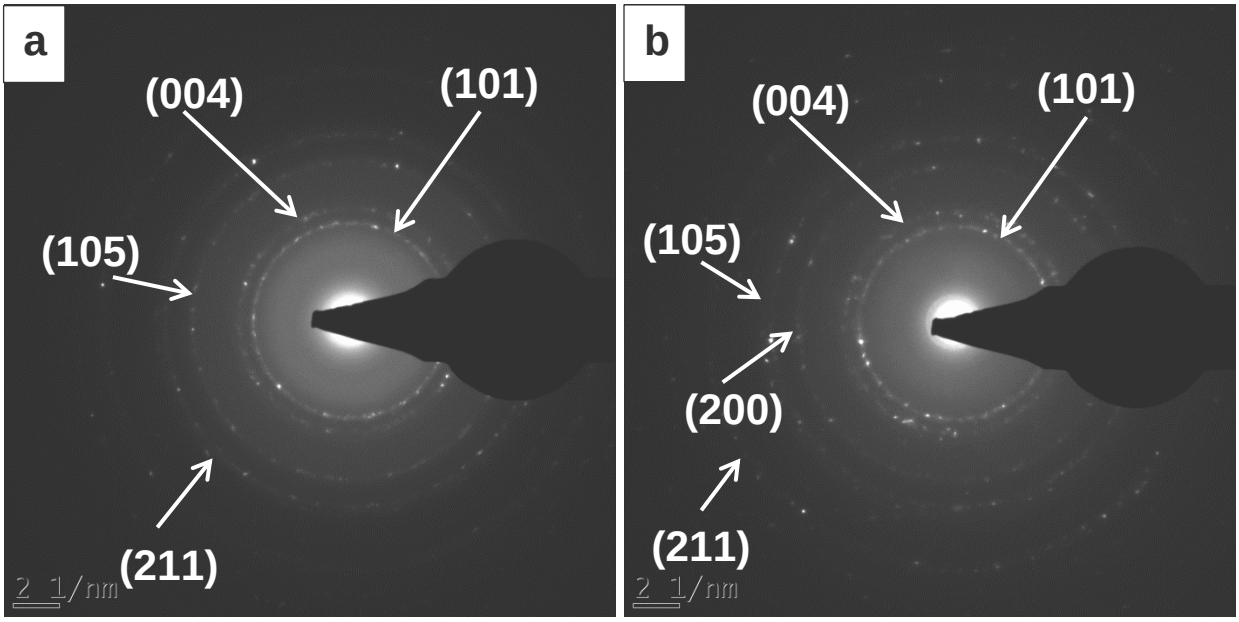

Figure 4.4: SAED micrograph of the a) pristine TiO_2, and b) Ag-TiO_2 nanoparticles confirming the hkl miller index (planes) found in the XRD spectra.

Selected Area Electron Diffraction (SAED) was obtained from HR-TEM which revealed and confirmed that the nanoparticles were crystalline as seen in **Figure 4.4 a)** and **b)**. The planes found in XRD plot in **Figure 4.3** above were also observed in the SAED image obtained, which confirms the anatase phase composition of the synthesized nanoparticles. The images obtained from SAED analysis, shows that both the pristine TiO_2 and Ag-TiO_2 were crystalline. The higher crystallinity displayed by Ag-TiO_2 translated into a high electro-activity which was the expected outcome with improved photocatalytic property as seen from the discussions of electrochemistry of the thin films and their optical properties which leads to a possible correlation between high crystallinity and electro-activity as the least crystalline of the nanoparticles TiO_2 displayed a lower electro-activity when compared to Ag-TiO_2 which was more crystalline.

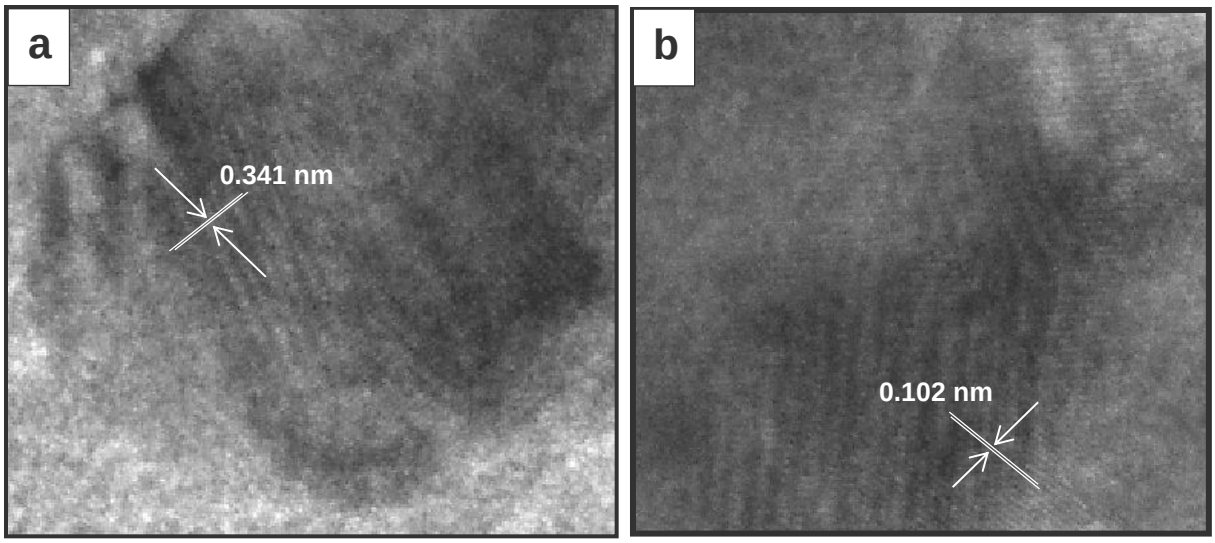

Figure 4.5: HR-TEM image of a) pristine compact-TiO_2, b) Ag-TiO_2 showing the lattice fringe and d-spacing values of the lattice.

The lattice fringe images obtained for the synthesized nanoparticles further confirms that the nanoparticles were crystalline and the d-spacing value of the lattice fringes were assigned as can be seen in **Figure 4.5 a)** and **b)** above.

4.1.4 Elemental composition

1.1.1.3 Energy Dispersive Spectroscopy (EDS)

The elemental composition of the prepared thin films was evaluated using Energy Dispersive X-ray spectroscopy (EDS) as shown in figure 4.11.

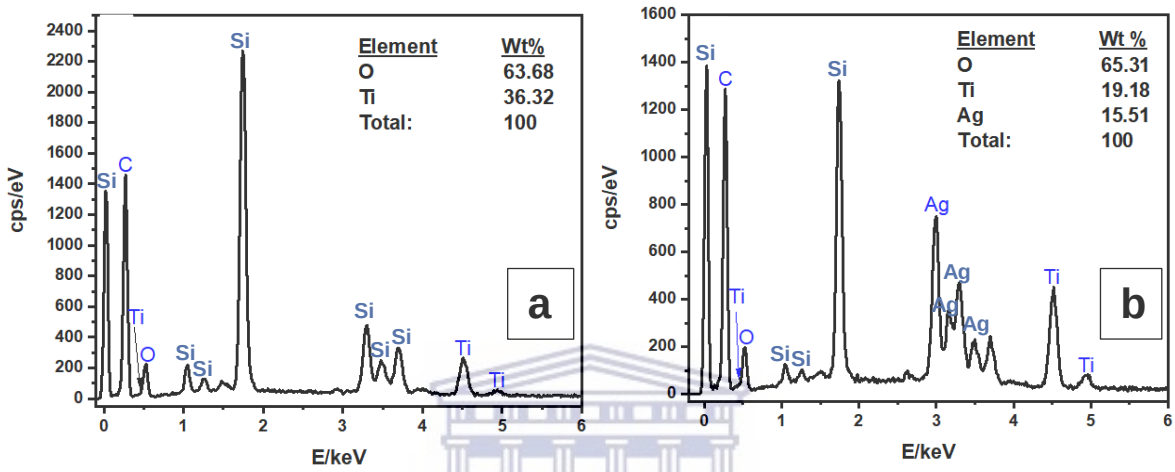

Figure 4.6: EDS images of a) Pristine TiO_2 and b) Ag-TiO_2 composite films with substracted ITO substrates peaks.

Figure 4.6 a) and b) displays the EDS results obtained for both the pristine TiO_2 and Ag-TiO_2 films surface with subtracted ITO substrate peaks. The EDS spectra of the prepared thin films showed all the elements expected for the samples analyzed. **Figure 4.5 a)** shows the pristine TiO_2 spectra, where the presence of titanium, oxygen and carbon can be observed. The same can be seen in **Figure 4.5 b)** which shows the Ag-doped TiO_2 spectra, where the presence of titanium, oxygen and carbon can be observed, however silver is present as well. Silver particles were spotted in different points. Carbon grids were used for SEM analysis, hence the presence of carbon in the spectra. Overall the EDS analysis provided a semi-quantitative elemental analysis of the surface showing that Ti and Ag appeared on the surface.

1.1.1.4 Fourier Transform Infra-red Spectroscopy (FTIR)

Fourier transform infra-red spectroscopy **(**FTIR**)** was used to identify the functional groups in the prepared pristine TiO_2 and Ag-TiO_2 thin films**.**

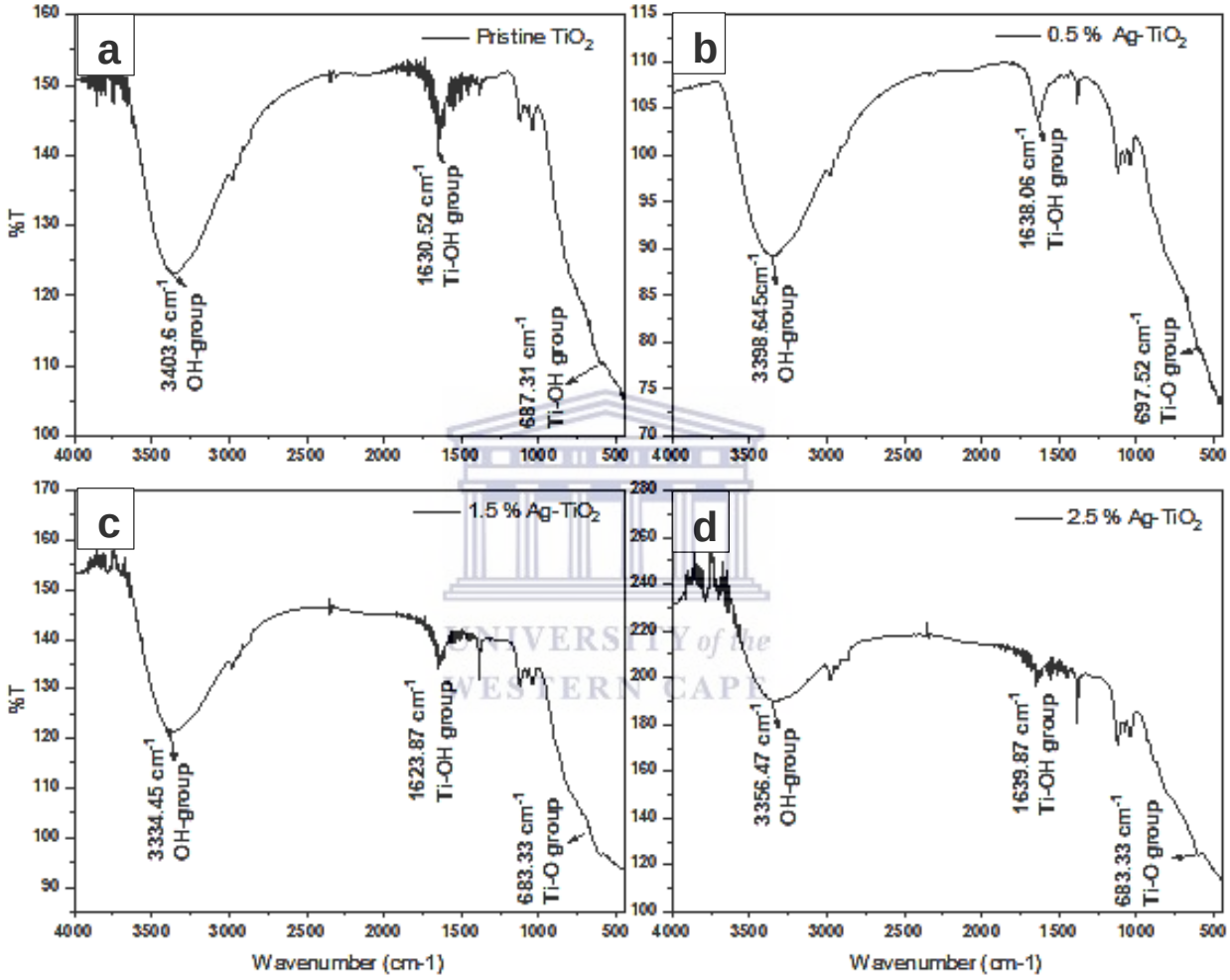

Figure 4.7: FTIR spectra of a) pristine TiO_2, b) 0.5% Ag-doped TiO_2, c) 1.5% Ag-doped TiO_2 and d) 2.5 % Ag-doped TiO_2 thin films on ITO substrates recorded at room temperature.

Figure 4.7 a), b), c) and d) shows the FTIR spectra of the pristine TiO_2 and Ag-TiO_2 thin films prepared at different percentage doping. From the vibration bands obtained from the spectra of each of the analyzed films, we can notice the presence of a broad band appearing in the range of

3330-3400 cm^{-1} which is attributed to the O-H stretching vibration and band in the range of 1630-1640 cm^{-1} attributed to Ti-O-H bending vibration which is present as a result of the chemically adsorbed water molecules. The broad band at 450-850 cm^{-1} represents the Ti-O bending mode of vibrations which corroborates the presence of metal oxygen bonding [2].

4.1.5 Optical Absorption

1.1.1.5 UV-Visible Spectroscopy (UV-Vis)

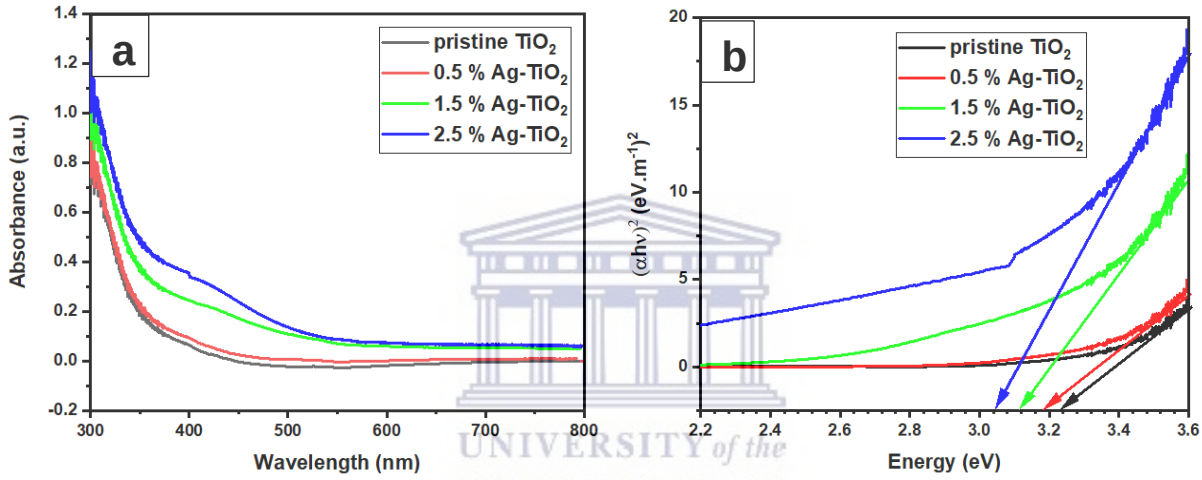

Figure 4.8: a) UV-Vis absorption spectra of pristine TiO_2 and Ag-TiO_2 composite compact films b) Tauc plot for bandgap calculation of the pristine TiO_2 and Ag-TiO_2 composite compact films.

The UV–Vis absorption spectra results are shown in **Figure 4.8 a)**. By doing a comparison of the optical absorption curves of the Ag-TiO_2 composite compact film, it is clear that, as the percentage of Ag augments, the absorption is progressively enhanced; the 2.5% Ag/nano-TiO_2 composite compact film shows the highest amount of absorption. The Ag-TiO_2 composite samples have higher absorption than the samples that do not contain Ag in the visible light region, which is mostly attributed to the surface plasmon resonance (SPR) of the metallic Ag nanoparticles in the Ag-TiO_2 composite compact film [3–6].

Figure 4.8 b) shows the Tauc plot obtained from the absorption of the undoped and Ag doped TiO_2 films. The graph was rescaled on the x-axis so it starts from 2.2 eV and ends at 3.6 to make

sure the area of interest was highlighted and clearly visible. As the ratio of Ag doping rises from 0% mol to 2.5 % mol, the band gap values are reduced. It can be observed that the band gap and absorbance spectra corroborate each other. These observed findings demonstrate that doping can potentially decrease the width of the forbidden band of TiO_2 thin films. The range of values found in the literature for the band gaps of anatase lie between 3.20 and about 3.56 eV [7]. In our specific study, though the band gap of undoped TiO_2 film is 3.23 eV, it obviously decreased to 3.04 for 2.5 % mol Ag doped TiO_2 film. A potential process behind the decreasing band gap of Ag-doped TiO_2 films could be that lattice distortion occurred with doping Ag ions in TiO_2 and produced the contamination level in the forbidden band of TiO_2. Adsitionaly, it can be speculated that fermi level of TiO_2 is higher than that of loaded silver. Silver deposits behave as buildup/accumulation sites for photo-generated electrons transferred from TiO_2 [8]. Effective separation of electrons and holes can therefore be reached by raising the silver content up to the optimum proportion.

The trend observed with the reduction in band gap as the Ag percentage doping is increased is indicative that the impact of silver within a perovskite solar cell device would be that of increasing the the light absorption of the electron transport layer (ETL) therefore allowing the absorbing layer to use the light received much more efficiently, which in turn could ultimately result in an improvement of the overall power conversion efficiency of the device.

Table 4.1: Band gap values of the undoped TiO_2 and Ag doped TiO_2.

Film	Eg (eV)
0 % Ag-TiO_2	3.23
0.5 % Ag-TiO_2	3.18
1.5 % Ag-TiO_2	3.11
2.5 % Ag-TiO_2	3.04

4.1.6 Electrochemistry

1.1.1.6 Cyclic Voltammetry (CV)

In order to evaluate the electronic behavior of the blocking layer, cyclic voltammetry study was done. The electro-activity of the prepared thin films was investigated using a 5 mM $K_3Fe(CN)_6$ in 0.1 M KNO_3 electrolyte. The potential window used for the investigation was -1.0 V to +1.0 V. The precursor materials that were investigated were bare ITO, pristine TiO_2 coated ITO, 0.5 % Ag-TiO_2 coated ITO, 1.5 % Ag-TiO_2 coated ITO and 2.5 % Ag-TiO_2 coated ITO. It is important to note that the bare ITO was also studied to clearly observe the trends in changes in conductivity of the coated layers by comparison. Scan rates of 10 mV/s, 50 mV/s and 100 mV/s were studied for each of the layers studied, but 50 mV/s was chosen as the optimal scan rate which was used ultimately used for the study.

A three-electrode system comprising of working electrode, counter electrode and reference electrode was used. The working electrode used was ITO coated glass substrate coated with the materials while the counter electrode was a platinum electrode and the reference electrode used was a Ag/AgCl reference electrode in 3 M KCl. As scan rate was initiated, potential was applied to the material within the potential window, at a characteristic potential value the materials responded with a current peak assuming they exhibit electrochemical behavior within that window. The voltammograms of the precursor materials that showed cathodic and anodic peaks are summarized in **Figure 4.8 a)** to **d)**.

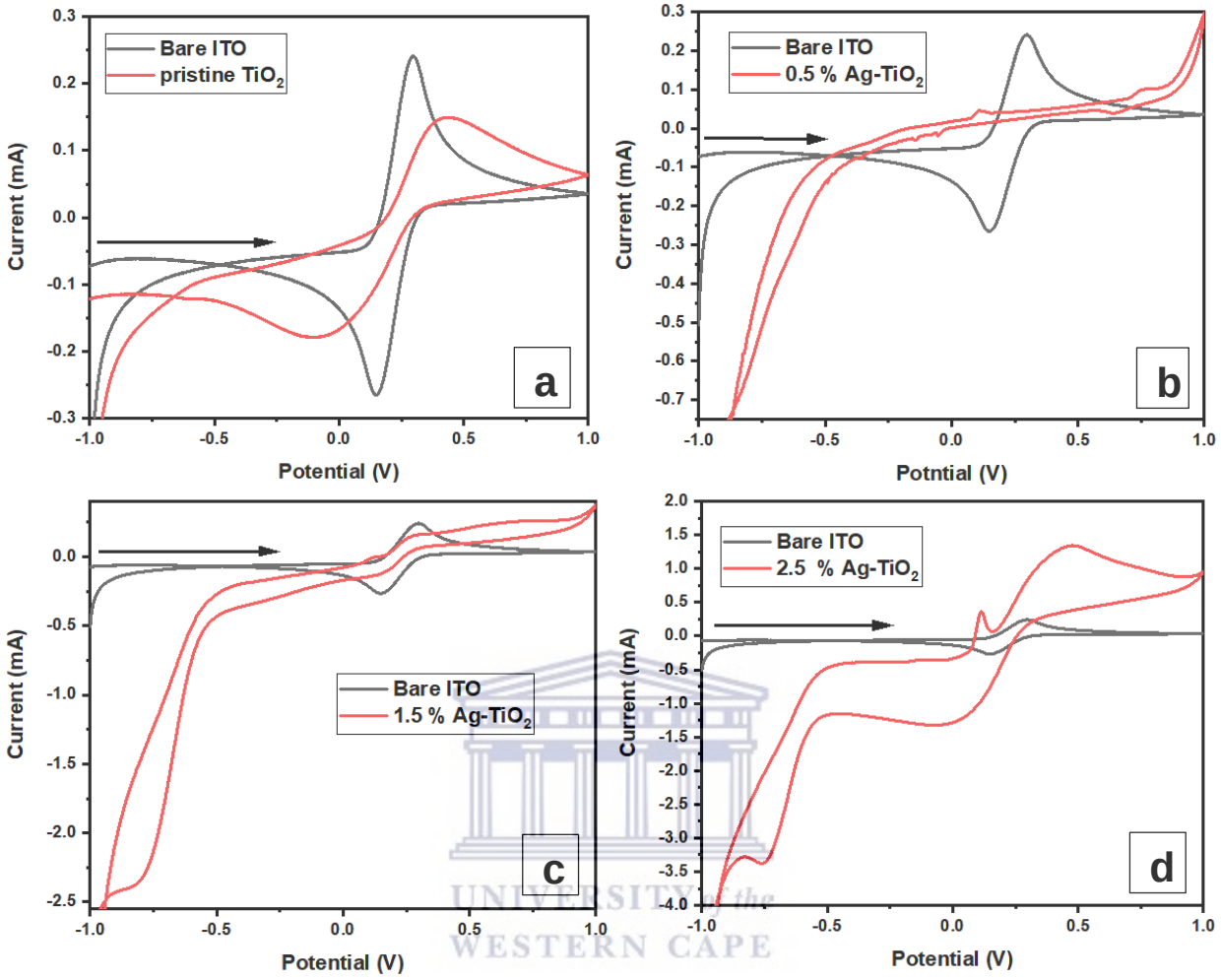

Figure 4. 9: Cyclic voltammograms of a) bare and TiO_2 coated ITO b) bare and 0.5 Ag-TiO_2 coated ITO c) bare and 1.5 % Ag-TiO_2 coated ITO and d) bare and 2.5 % Ag-TiO_2-coated ITO. The analyses are recorded at scan rate of 50 mV. s^{-1} in a 5 mM of $K_3Fe(CN)_6$ with 0.1 M KNO_3.

As seen in **Figure 4. 9 a),** the presence of the spin-coated pristine TiO_2 slightly decreases the anodic and cathodic currents with respect to a bare ITO electrode which is in this case very good as it confirms the assumption we made in the morphological analysis that there were no observable pinholes on the surface of the layer. However the shape of the curves, the peaks shift and the current variations, do suggest some substantial change of the electrode surface as already confirmed by the morphological analysis.

Compared to **Figure 4.** 9 **a)**, the behavior of the 0.5% Ag-TiO_2 is much different as seen in the cyclic voltammogram shown in **Figure 4.** 9 **b)**. Here, what is observed is that there is a much larger decrease the anodic and cathodic currents with respect to the bare ITO electrode not at very negative potentials. This decrease is accompanied by the appearance of much smaller cathodic and anodic peak which are quasi inexistent at -0.1 and 0.4 V, which in this case would be associated to the influence of the Ag nanoparticles. However the trend observed with the increase in Ag percentage observed in **Figure 4. 9 b)** through to **d)** is that there is once again an increase in anodic and cathodic peak currents. This is an indication that even though the TiO_2 is acting as a blocking layer limiting the interaction between the electrolyte and the ITO electrode, the presence of the Ag within the TiO_2 layer makes the substrate more conductive. This trend alone is indicative that the impact of silver within a perovskite solar cell device would be that of increasing the electron charge transfer to the electron transport layer (ETL) and which could ultimately result in an improvement of the overall power conversion efficiency of the device.

4.2 Device characterization

4.2.1 I-V measurements

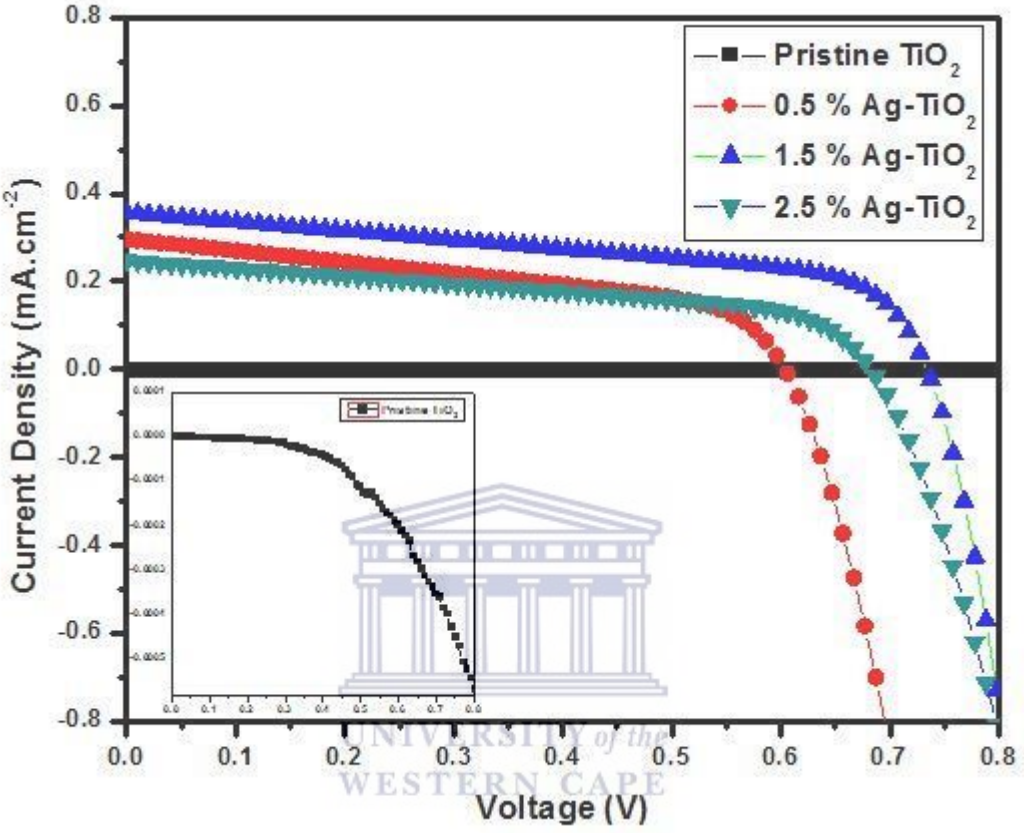

Figure 4.10: I-V characteristics of PSC devices based on different contents of Ag-TiO_2 composites compact films under AM 1.5G irradiation (100 $mW.cm^{-2}$).

The PSC devices' performance was evaluated under AM 1.5G irradiation (100 mW cm^{-2}). Each Each step involved in the fabrication the PSC device was done in ambient air and at a moisture level of about 60%. Humidity was one big issue that had to be addressed as the device degradation was accelerated by it. Then, the PSC devices were kept in a drying box. The I–V curves of the PSCs with the pristine compact film and the 0.5, 1.5, and 2.5 % Ag-TiO_2 composite compact films are shown in **Figure 4.10** and the corresponding photovoltaic parameters are listed in **Table 4.2**.

The data in **Table 4.2** demonstrate that J_{SC} improves progressively with the increase Ag amount except for the 2.5% Ag-TiO_2; the PSC device with the 1.5% Ag-TiO_2 composite compact film has the highest Jsc and achieves 0.36 mA.cm^{-2}. However, with the increase in the content of Ag, the PSC device with the 2.5% Ag/nano-TiO_2 composite compact film has the lowest J_{SC} and PCE, because a high content of Ag lowers the electron conducting role of the TiO_2 and the Ag impurities also act as a recombination center, resulting in lower J_{SC} and PCE values [9].

Table 4.2: Summarized parameters of PSC devices based on 0-2.5 % Ag-TiO2 composite compact film.

Samples	V_{oc} (V)	J_{sc} (mA.cm^{-2})	FF (%)	PCE (%)
0 % Ag-TiO_2	0.17	0.15	0.36	0.01
0.5 % Ag-TiO_2	0.60	0.30	0.50	0.09
1.5 % Ag-TiO_2	0.73	0.36	0.51	0.14
2.5 % Ag-TiO_2	0.70	0.25	0.48	0.08

It can also be observed from **Table 4.2** that the open-circuit voltage (V_{OC}) difference is quite important for the PSC devices with different contents of the Ag-TiO_2 composite compact film. It is known that V_{OC} is determined by the CB of TiO_2 and the perovskite in the PSC device, which means that the addition of Ag into the TiO_2 nanocrystal has had a significant impact on the CB of TiO_2. In general, the perovskite solar cell with the 1.5% Ag–TiO_2 composite compact film exhibits the highest PCE of 0.14 % and J_{SC} of 0.36 mA cm^{-2}, representing a 140 and 130 % increase compared to the PSC device without Ag. The percentage increase is extremely high, so one reason for this could be whether the layers were compact enough and well deposited on top of each other during the fabrication process as any irregularities during that process could potentially affect these parameters which may results in situation such as this.

4.3 References

[1] W. Li, R. Liang, A. Hu, Z. Huang, Y.N. Zhou, Generation of oxygen vacancies in visible light activated one-dimensional iodine TiO2 photocatalysts, RSC Adv. 4 (2014) 36959–36966. doi:10.1039/c4ra04768k.

[2] O.F. Tio, S. Composites, A.N. Murashkevich, A.S. Lavitskaya, T.I. Barannikova, I.M. Zharskii, Infrared Absorption Sectra and structure of TiO_2-SiO_2 composites, J. Appl. Spectrosc. 75 (2008) 724–728.

[3] J. He, I. Ichinose, S. Fujikawa, T. Kunitake, A. Nakao, Reversible conversion of nanoparticles of metallic silver and silver oxide in ultrathin TiO_2 films: A chemical transformation in nano-space, Chem. Commun. 8 (2002) 1910–1911. doi:10.1039/b204227b.

[4] D.W. Brandl, P. Nordlander, Plasmon modes of curvilinear metallic core/shell particles, J. Chem. Phys. 126 (2007). doi:10.1063/1.2717167.

[5] K. Kawahara, K. Suzuki, Y. Ohko, T. Tatsuma, Electron transport in silver-semiconductor nanocomposite films exhibiting multicolor photochromism, Phys. Chem. Chem. Phys. 7 (2005) 3851–3855. doi:10.1039/b511489f.

[6] K. Matsubara, T. Tatsuma, Morphological changes and multicolor photochromism of Ag nanoparticles deposited on single-crystalline TiO2 surfaces, Adv. Mater. 19 (2007) 2802–2806. doi:10.1002/adma.200602823.

[7] A. Nakaruk, D. Ragazzon, C.C. Sorrell, Anatase-rutile transformation through high-temperature annealing of titania films produced by ultrasonic spray pyrolysis, Thin Solid Films. 518 (2010) 3735–3742. doi:10.1016/j.tsf.2009.10.109.

[8] Y. Cao, H. Tan, T. Shi, T. Shi, T. Tang, J. Li, Preparation of Ag-doped TiO_2 nanoparticles for photocatalytic degradation of acetamiprid in water, J. Chem. Technol. Biotechnol. 83 (2008) 546–552. doi:10.1002/jctb.1831.

[9] B. Xin, L. Jing, Z. Ren, B. Wang, H. Fu, Effects of Simultaneously Doped and Deposited Ag on the Photocatalytic Activity and, J. Phys. Chem. B. 109 (2005) 2805–2809.

Chapter 5 Conclusions and Future work

This chapter gives a summary of the outcome of the research done in this thesis. It also gives recommendations with regards to some of the objectives that were not met and the way forward in order to improve and the results obtained from the J-V measurements of the solar cells.

5.1 Conclusions

Perovskite solar cells have had a substantial progression in terms of power conversion efficiency going from 3.8% to over 22% since 2012. Tandem perovskite-based solar cells have had an even better increase with PCEs reaching as high as 26.7%, setting a new record in the history of photovoltaic technology. A lot of research efforts have been put in place in order to both improve PSCs efficiency and attain a much deeper understanding of the perovskite materials' outstanding electrical and optical properties, such as largely-tunable band gaps for light absorption, high absorption coefficients, large carrier diffusion lengths, great carrier mobility, have been established during the past few years. The PSCs currently researched on already have combined structural advantages of both DSSCs and thin film PV ever since the discovery of perovskite and have become one of the main contenders to Si-based PV dominant market share, not only owing to its record 22.1% efficiency for small area but also for comparable larger-area device efficiency.

With the above mentioned facts in mind, the aim of this project was to develop efficient and cost-effective solar cells through the process of synthesis, fabrication, optical and electrochemical characterization of Ag-TiO_2/Perovskite/ Spiro-OMeTAD-based PSCs. The PSCs were fabricated with different doping percentages of Ag in the electron transport layer which in this case was TiO_2 to form Ag-TiO_2 composite films. The addition of the Ag to the TiO_2 drastically improved the light absorption of the TiO_2 in the visible light region as was confirmed by the UV-Vis results and band gap values obtained from it. This same trend was also seen in the built PSCs devices. This improvement was due to the resonance plasmon effect of the metallic Ag nanoparticles present in the Ag-TiO_2 composite compact films. Due to the addition of the Ag nanoparticles, an improvement in the conductivity was observed as seen with CV

results which in turn decreased the charge transfer resistance of the PSC device and the cells performances clearly improved. However compared to the TiO_2 without Ag, only one device containing 1.5 % Ag-TiO_2 achieved higher PCE of 0.14%.

5.2 Recommendations

The above research project indicated that there is truly a great potential for PSCs if the stability the cells as well as fabrication process and conditions is improved. In this work as was observed in the results obtained from the J-V measurements very low current output was obtained leading to the overall efficiencies of the devices being very low. Therefore, in order to remediate to this issue, very careful attention needs to be put first of all on the layer deposition techniques used. We know form literature that the devices with the good and even layer homogeneity obtain in most cases the best efficiencies. Secondly careful attention needs to be put on the monitoring of the layer thickness as it is also a very critical parameter that needs to be taken into account if higher efficiencies are going to be achieved.